

Functional genetics of rare neurological disorders

Andreea Aura Manole

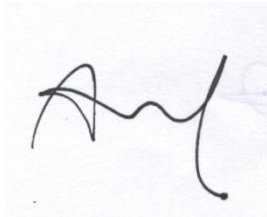
Department of Molecular Neuroscience, UCL Institute of Neurology
& MRC Centre for Neuromuscular Diseases

PhD Supervisors: Professor Henry Houlden, Professor Dimitri M.
Kullmann and Professor Mike G. Hanna

A Thesis submitted for the degree of
Doctor of Philosophy
University College London
June 2017

Declaration

I, Andreea Aura Manole, confirm that the work presented in this Thesis is my own. Where information has been derived from other sources, I confirm that this has been indicated in the Thesis.

A handwritten signature in black ink, appearing to be 'Am', on a light blue background.

Date: 08.06.2017

Abstract

The study of rare Mendelian disorders is able to provide unique insights into neurological disorders that may seem unrelated. This thesis reports mechanistic investigations of five neurological disorders presenting with progressive or episodic neurological symptoms. First, riboflavin transporter neuronopathy represents a phenotypic spectrum of motor, sensory and cranial nerve neuropathy, often with respiratory problems. Our main findings implicate mitochondrial dysfunction as a downstream consequence of riboflavin transporter gene defects and validate riboflavin esters as a potential therapeutic strategy. Second, novel sequence variants in the *SBF1* gene are described as potential mutations in patients with severe axonal neuropathy and bulbar features. Our findings suggest that *SBF1* mutations may cause a syndromic form of autosomal recessive axonal neuropathy in addition to demyelinating Charcot-Marie-Tooth disease. Third, novel frameshift mutations in *SPG11*, investigated using mRNA, are described in patients with complex hereditary spastic paraplegia (HSP) consistent with *SPG11*. The findings that mutations in *SPG11* are the cause of a spectrum of clinical features including the late manifestation of severe axonal neuropathy are extended. Fourth, a family with HSP carrying a *de novo* mutation in *KCNA2* is described. Our results using two-electrode voltage clamp recordings confirm that the mutation is pathogenic, exerting a loss-of-function effect. The discovery of *KCNA2* mutations in epilepsy, ataxia, and HSP extends the phenotypes that can be associated with this gene. Finally, a novel *KCNA1* mutation associated with episodic ataxia and a possible link with malignant hyperthermia is reported. Our work broadens the phenotypes associated with *KCNA1* mutations to include possible susceptibility to malignant hyperthermia, and shows the potential of using induced pluripotent stem cell derived neurons to determine the neuronal consequences of the Kv1.1 mutation. The diverse methods used in this thesis advance the understanding, and potential treatment, of a group of neurological disorders caused by single gene defects.

Acknowledgments

I would like to express my sincere gratitude to my supervisors, Professor Henry Houlden, Professor Dimitri Kullmann, and Professor Mike Hanna, for their invaluable support, insight and guidance throughout my PhD. I am particularly grateful to Dr Roope Mannikko, Dr Monika Madej, Dr Charlie Arber, Dr James Jepson, Dr Iain Hargreaves, Prof Andrey Abramov, Dr Gabriele Lignani, Dr Marife Cano-Jaimez, and Dr Alice Gardiner, for providing training in the different techniques used in this thesis. I would also like to thank the current and past members of my lab group and the faculty members: Dr Alejandro Horga, Dr Enrico Bugiardini, Dr Zane Jaunmuktane, Dr Alan Pittman, Debbie Hughes, Dr Vincenzo Salpietro, Dr Renata Scalo, Dr Marthe Ludtmann, Stephanie Efthymiou, Ben O'Callaghan, Elisavet Preza, Chris Lovejoy, Eloise Tribollet, Dr Selina Wray, Albert Snowball, Dr Andres Vicente, Dr Erica Tagliatti, Dr Philippe Mendonça, Dr Andrianos Liavas, Dr Simon Pope, Dr Oscar Bello, Dr Natalia Zanetti, Dr Conceicao Bettencourt, Dr Elizabeth Nicholson, Louise King, Dr David Lynch, Dr Stjepana Kovacs, Dr Ellen Cottenie, Dr Amelie Pandraud, Dr Qiang Gang, Dr Mercier Marion, Dr Elodie Chabrol-Pipard, Jonathan Cornford, Dr Christine Dixon, Eleonora Lugara, Dr Marc Soutar, Patrick Kratschmer, Dr Andreas Lieb, Dr Claudia Manzoni, Dr Noemi Esteras Gallego, Dr Lucie Bard, Prof Gipi Schiavo, Dr Helene Plun-Favreau, Dr Emma Deas, Dr Plamena Angelova, Dr Sophie Williams, Dr Rahima Begum, Dr Gareth Morris, Dr Emer Oconnor, Dr Piotr Michaluk, Dr Eleanna Kara, Dr Stephanie Schorge, Jenna Carpenter, Dr Rob Wykes, Dr Yamina Bakiri, Alex Brown, Dr Raffaele Ferrari, Dr Mike Parkinson, Dr Paula Giunti, Dr Serena Wu, Dr Zhi Yao, Dr Sarah Wiethoff, Dr Viorica Chelban, Prof Mary Reilly for the advice, support and collaboration and Dr Lee Stanyer for ordering reagents and printing the thesis. Special thanks to Dr Paul Dobbin and Dr Sinan Battah for reagents and helpful discussions. I would like to thank the Neurogenetics Unit, as well as the Neurometabolic Unit at the NHNN for their help, advice, and valuable suggestions during my PhD. I also thank all our collaborators and patients for their essential contribution to my research. This thesis is dedicated to my family and friends for their continued encouragement and support.

The experiments in this thesis were funded mainly by the MRC Centre for Neuromuscular diseases and the Synapthopathies Strategic Award from the Wellcome Trust.

Table of Contents

Declaration.....	2
Abstract.....	3
Acknowledgments	4
Table of Contents.....	5
List of Tables	9
List of Figures.....	10
List of Abbreviations	12
List of Publications	18
Chapter 1 General introduction	20
Functional genetics and aims of this thesis	22
The peripheral nervous system.....	25
Peripheral neuropathies	25
The cerebellum	28
Cerebellar ataxias	28
Thesis outline.....	31
Chapter 2 General methods	32
Patient cohorts	32
DNA extraction from blood samples	32
Primer design.....	32
Polymerase chain reaction.....	33
Agarose gel electrophoresis.....	33
PCR purification.....	34
Sanger sequencing	34
Whole-exome sequencing	35
Mutation nomenclature.....	36

Cell culture	37
<i>Drosophila</i> husbandry	39
Quantification of flavins in <i>Drosophila</i>	39
Assessment of activities of mitochondrial electron transport chain complexes .	40
Adult behaviour	41
Molecular biology	42
<i>Xenopus</i> oocyte collection, preparation and injection.....	43
Electrophysiology.....	43
Immunocytochemistry	44
Statistics.....	45
Specific methods	45
Chapter 3 Riboflavin Transporter Deficiency Neuronopathy	46
Introduction	46
Molecular Genetic Pathogenesis	47
Riboflavin transporters	49
Riboflavin and its derivatives.....	50
Mitochondrial electron transport chain	51
Mitochondria in neurodegeneration	54
Animal models of riboflavin transporter deficiency	54
Aims of this chapter	56
Methods	57
Results	62
Discussion.....	75
Chapter 4 <i>SBF1</i> mutations associated with axonal neuropathy with cranial nerve involvement.	78
Introduction	78
Methods	80
Results	82

Discussion.....	85
Chapter 5 Severe axonal neuropathy is a late manifestation in hereditary spastic paraplegia.....	87
Introduction	87
Methods	88
Results	92
Discussion.....	98
Chapter 6 <i>KCNA2</i> in hereditary spastic paraplegias	100
Introduction	100
Methods	101
Results	102
Discussion.....	105
Chapter 7 <i>KCNA1</i> in episodic ataxia and malignant hyperthermia.....	106
Introduction	106
Methods	108
Results	109
Discussion.....	114
Chapter 8 Modelling of episodic ataxia 1 with iPSC-derived neurons.....	116
Introduction	116
Methods	117
Results	124
Discussion.....	133
Conclusions and future work.....	138
References.....	140
Appendix I	160
Appendix II.....	161
Appendix III	162

Appendix IV	163
Appendix V.....	164
Appendix VI	165

List of Tables

Table 1-1 Molecular genetics and clinical features of episodic ataxias.....	30
Table 3-1 OMIM Entries for the Brown-Vialetto-Van Laere Syndrome	48
Table 3-2 Clinical and genetic features of BVVLS patients (AP1-10).	63
Table 3-3 Clinical and genetic features of BVVLS patients (AM1-10).	64
Table 4-1 Single-gene causes of CMT.....	79
Table 4-2 Primer sequences used for PCR and Sanger sequencing of <i>SBF1</i>	81
Table 5-1 Broad classification of hereditary spastic paraplegias.....	87
Table 5-2 <i>SPG11</i> PCR primer sequences used for PCR and sequencing.	91
Table 5-3 <i>SPG11</i> PCR program for sequencing of genomic and cDNA.....	92
Table 5-4 Nerve conduction studies and electromyography in <i>SPG11</i> patients.....	94
Table 7-1 Characterization of currents from oocytes coexpressing subunits.	112
Table 8-1 qPCR primer sequences for pluripotency and neural markers	121
Table 8-2 Primary antibodies used in this study and their details.	122
Table 8-3 Characterization of iPSC generated in this study	124
Table 8-4 Parameters of 152E iN neurons	132
Table 8-5 Parameters of SP2i iN neurons.....	133

List of Figures

Figure 1-1 Overview of the history of genomics.	21
Figure 1-2 General workflow scheme for the study of functional genetics underlying neurological disorders.	24
Figure 2-1 Filtering strategy for whole exome sequencing data.	36
Figure 3-1 Prevalence of symptoms in the Brown-Vialetto-Van Laere syndrome.	47
Figure 3-2 Timeline with important hallmarks over more than a century.	48
Figure 3-3 Distribution of human riboflavin transporters.	49
Figure 3-4 Riboflavin transport and metabolic trapping of FMN and FAD.	51
Figure 3-5 Diagram of mitochondrial electron transport chain complexes.	53
Figure 3-6 Conservation of residues amongst DRIFT, RFVT1, RFVT2 and RFVT3.	55
Figure 3-7 Reduced mitochondrial activity in BVVLS patient fibroblasts.	68
Figure 3-8 Semi-quantitative RT-PCR illustrating <i>drift</i> (<i>cg11576 RNAi</i>) knockdown.	69
Figure 3-9 Knockdown of <i>drift</i> results in reduced mitochondrial activity.	70
Figure 3-10 <i>drift</i> knockdown reduces locomotor activity larvae.	71
Figure 3-11 <i>drift</i> knockdown reduces locomotor activity and lifespan in <i>Drosophila</i>	72
Figure 3-12 A riboflavin ester partially rescues the drift knockdown phenotypes.	74
Figure 4-1 Characteristics of <i>SBF1</i> family from this study.	84
Figure 4-2 Domain models of the DENN domain-bearing protein SBF1.	86
Figure 5-1 Sagittal MRI sequence.	95
Figure 5-2 Pedigree of the F1 <i>SPG11</i> family.	97
Figure 5-3 cDNA sequencing chromatograms.	97
Figure 5-4 Schematic representation of the SPG11 protein.	99
Figure 6-1 <i>KCNA2</i> family found in this study.	103
Figure 6-2 Electrophysiology for the Kv1.2 wild-type and mutant channels.	104

Figure 7-1 <i>KCNAI</i> family pedigree.	109
Figure 7-2 Electrophysiological characterization of Phe249Cys mutant	111
Figure 7-3 Mean TEA dose–response data.	113
Figure 7-4 Mean current–voltage data	113
Figure 8-1 Validation characteristics of iPSC used in this study.....	125
Figure 8-2 Stain for pluripotency markers of the iPSCs.....	126
Figure 8-3 q-PCR testing for expression of endogenous pluripotency factors.	127
Figure 8-4 Staining for neuronal precursor markers of 73O41.....	128
Figure 8-5 qPCR for neural markers.....	129
Figure 8-6 Staining for panNav	131
Figure 8-7 Electrophysiological data for the human iN neurons	132
Figure 8-8 Mechanism for cell cycle and neuronal differentiation coordination.	135

List of Abbreviations

AAAS	Achalasia-Addisonianism-Alacrima Syndrome
Acetyl-CoA	Acetyl-Coenzyme A
Acyl-CoA	Acyl-Coenzyme A
AD	Autosomal dominant
ALS	Amyotrophic Lateral Sclerosis
ANOVA	Analysis of variance
AR	Autosomal recessive
AMP	Adenosine 5'-monophosphate
ATP	Adenosine 5'-triphosphate
ATP5 β	ATP-synthase β (subunit)
Bp	Base pair
BLAST	Basic Local Alignment Search Tool
BSA	Bovine serum albumin
BVVLS	Brown-Vialetto-Van Laere syndrome
C20orf54	Chromosome 20 open reading frame 54
cAMP	Cyclic adenosine monophosphate
cDNA	Complementary deoxyribonucleic acid
CaCl ₂	Calcium chloride
CG69	Complete Genomics 69
CGH	Comparative Genomic Hybridization
CI	Confidence interval
CIDP	Chronic inflammatory demyelinating polyneuropathy
CMAP	Compound muscle action potential
CMT	Charcot-Marie-Tooth disease
CNS	Central nervous system
CoQ	Coenzyme Q
CoQ ₁	Coenzyme Q ₁
CoQ ₁₀	Coenzyme Q ₁₀
COX10	Cytochrome c oxidase assembly homolog 10
CS	Citrate synthase
C _t	Threshold cycle
DA	Daughterless (driver: da-GAL4)

DIC	differential interference contrast
DAPI	4',6-Diamidino-2-phenylindole
dbSNP	Single nucleotide polymorphism database
DCPIP	2,6-Dichlorophenol-indophenol
ddH ₂ O	double distilled water
ddNTP	Dideoxynucleotides
dH ₂ O	Deionised water
dHMN	Distal hereditary motor neuropathy
DENN	differentially expressed in normal and neoplastic cells domain region
DIV	Days <i>in vitro</i>
DMEM	Dulbecco's modified eagle medium
DMSO	Dimethyl sulfoxide
DNA	Deoxyribonucleic acid
DNMT1	DNA (cytosine-5-)-methyltransferase 3
DNP	2,4-Dinitrophenol
dNTP	Deoxyribonucleotide triphosphate
DPBS	Dulbecco's phosphate buffered saline
DRIFT	Drosophila riboflavin transporter
DSD	Dejerine-Sottas disease
DTT	Dithiothreitol
EA1	Episodic ataxia 1
EDTA	Ethylenediaminetetraacetic acid
EEG	Electroencephalogram
EMG	Electromyogram
EVS	Exome Variant Server
FAD	Flavin adenine dinucleotide
FADH ₂	Flavin adenine dinucleotide (reduced)
FBS	Foetal bovine serum
FCCP	Carbonyl cyanide-4-(trifluoromethoxy)phenylhydrazone
FL	Fazio-Londe
FMN	Flavin mononucleotide
FOXG2	Forkhead-Box-Protein P2
GAPDH	Glyceraldehyde-3-phosphate dehydrogenase

GARS	Glycyl-tRNA synthetase
GATK	Genome Analysis Tool Kit
GFAP	Glial fibrillary acidic protein
GFP	Green fluorescent protein
GJB1	Gap junction protein, beta 1
GPR172A	G protein-coupled receptor 172A
GPR172B	G protein-coupled receptor 172B
HBSS	Hank's balanced salt solution
HCl	Hydrochloric acid
HEK293	Human embryonic kidney 293
HEPES	4-(2-Hydroxyethyl)-1-piperazineethanesulfonic acid
HLA	Human leukocyte antigen
HMSN	Hereditary motor and sensory neuropathy
HNPP	Hereditary neuropathy with liability to pressure palsies
HPLC	High-performance liquid chromatography
hRFVT1	Human riboflavin transporter 1
hRFVT2	Human riboflavin transporter 2
hRFVT3	Human riboflavin transporter 3
HSAN	Hereditary sensory and autonomic neuropathy
HSP	Hereditary spastic paraplegia
HSPB1	Heat shock 27 kDa protein 1
HSPB8	Heat shock 22 kDa protein 8
ION	Institute of Neurology
IPSc	Induced pluripotent stem cells
IVIG	Intravenous immunoglobulin
Kb	Kilobase
KCN	Potassium cyanide
KCNA1	Potassium Voltage-Gated Channel Subfamily A Member 1
KCNA2	Potassium Voltage-Gated Channel Subfamily A Member 2
KD	Knockdown
KDa	Kilodalton
KLF-4	Kruppel-like factor 4
LB	Luria-Bertani (broth)

MADD	Multiple acyl-CoA dehydrogenase deficiency
MAF	Minor allele frequency
Mb	Megabase
MBS	Modified Barth's Saline
MEF	Mouse embryonic fibroblast
MgCl ₂	Magnesium chloride
MgSO ₄	Magnesium sulphate
MH	Malignant hyperthermia
MLPA	Multiplex ligation-dependent probe amplification
MND	Motor neurone disease
MRC (Centre)	Medical Research Council (Centre)
MRI	Magnetic resonance imaging
mRNA	Messenger ribonucleic acid
MTMR2	Myotubularin related protein 2
MTMR13	Myotubularin related protein 13
NaCN	Sodium cyanide
NAD ⁺	Nicotinamide adenine dinucleotide (oxidised)
NADH	Nicotinamide adenine dinucleotide (reduced)
NaOH	Sodium hydroxide
NCBI	National Centre for Biotechnology Information
NCS	Nerve conduction study
NCV	Nerve conduction velocity
NEB	New England Biolabs
NESTIN	neuroectodermal stem cell marker
Ngn2	Neurogenin 2
NGS	Next-generation sequencing
NHNN	National Hospital for Neurology and Neurosurgery
NMD	Nonsense-mediated decay
OCT-4	octamer-binding transcription factor 4
OTX2	orthodenticle homeobox 2
P/S	Penicillin/streptomycin
PAX6	Paired box protein 6
PBS	Phosphate buffered saline

PCR	Polymerase chain reaction
PFA	Paraformaldehyde
PNS	Peripheral nervous system
PVDF	Polyvinylidene fluoride
qPCR	Quantitative polymerase chain reaction
RFVT1	Riboflavin transporter 1 (human) (new nomenclature)
RFVT2	Riboflavin transporter 2 (human) (new nomenclature)
RFVT3	Riboflavin transporter 3 (human) (new nomenclature)
RLAM	riboflavin-5'-lauric acid monoester
RNA	Ribonucleic acid
ROCK	Rho-associated, coiled-coil containing protein kinase
ROS	Reactive oxygen species
Rpm	Revolutions per minute
RT	Reverse transcription
RT-qPCR	Real-time reverse transcription polymerase chain reaction
SBF1	SET binding factor 1
SDH	Succinate dehydrogenase
SEM	Standard error of the mean
SIFT	Sorting Intolerant From Tolerant
<i>SLC52A1</i>	Solute carrier family 52, riboflavin transporter member 1
<i>SLC52A2</i>	Solute carrier family 52, riboflavin transporter member 2
<i>SLC52A3</i>	Solute carrier family 52, riboflavin transporter member 3
SNAP	Sensory nerve action potential
SNP	Single nucleotide polymorphism
SOD1	Superoxide dismutase 1
SOX2	SRY (sex determining region Y)-box 2
SPG11	spastic paraplegia type 11
TBE	Tris/borate/EDTA
Tbr1	T-box, brain, 1
TEVC	two-electrode voltage-clamp
TMRM	Tetramethylrhodamine methyl ester
TTFA	2-Thenoyltrifluoroacetone
UAS	Upstream activating sequence

UCL	University College London
UCLH	University College London Hospital
UMN	Upper motor neurone
UTR	Untranslated region
UV	Ultraviolet
VSVG	Vesicular stomatitis virus
WT	Wild-type
$\Delta\Psi_m$	Mitochondrial membrane potential

List of Publications

Manole A, Jaunmuktane Z, Hargreaves I, Pandraud, A, Salpietro V, Pope S, Ludtmann MHR, Horga A, Scalco RS, Li A, Ashokkumar B, Lourenço CM, Heales S, Horvath R, Chinnery PF, Toro C, Singleton AB, Jacques TS, Abramov AY, Muntoni F, Hanna MG, Reilly MM, Revesz T, Kullmann DM, Jepson JEC, Houlden H. Mitochondrial impairment and rescue in riboflavin responsive neuropathy. *Brain*. *In press*

Salpietro V, Zollo M, Vandrovцова J, Ryten M, Botia JA, Ferrucci V, **Manole A**, Efthymiou S, Mutairi FA, Bertini E, Tartaglia M and Houlden H. The phenotypic and molecular spectrum of PEHO syndrome and PEHO-like disorders. *Brain*, 2017, 140: e49

Salpietro V, Castañeda MS, **Manole A**, Efthymiou S, Bourinaris T, O'Connor E, Veneziano L, Mantuano E, Frontali M, Giunti P, Boles R, Garrido ED, Bettencourt C, Zuccotti GV, Marseglia GL, Botia JA, Ryten M, Vandrovцова J, McCall S, Labrum RW, Zuberi S, Tomlinson SE, Graves TD, Macaya A, Kullmann DM, Männikkö R, Houlden H, Hanna MG, SYNAPS Study Group. Genes that affect synaptic transmission identified by rare variant analyses in episodic ataxias. *Brain*. In review

Udhayabanu T, **Manole A**, Rajeshwari M, Varalakshmi P, Houlden H, Ashokkumar B. Riboflavin Responsive Mitochondrial Dysfunction in Neurodegenerative Diseases. *J Clin Med*. 2017 May 5;6(5).

Bugiardini E, Poole O, **Manole A**, Pittman AM, Horga A, Hargreaves I, Woodward C E, Sweeney MG, Holton JL, Taanman J-H, Plant GT, Poulton J, Zeviani M, Ghezzi D, Taylor J, Smith C, Fratter C, Meena AK, Paramasivam A, Thangaraj K, Spinazzola A, Holt IJ, Houlden H, Hanna MG, Pitceathly RDS. The clinicopathological and molecular spectrum of RNASEH1-related adult mitochondrial disease. *Neurology Genetics*. *Neurol Genet*. 2017 May 2;3(3):e149.

Salpietro V, Lin W, Liu Y, Efthymiou E, Wiethoff S, **Manole A**, Ye Q, Krishnakumar, S, Rothman JE, Bello O, Manzur A, Houlden H. Homozygous truncating mutations in VAMP1 cause a presynaptic congenital myasthenic syndrome. *Ann Neurol*. 2017 Apr;81(4):597-603.

Manole A, Horga A, Gamez J, Raguer N, Salvado M, San Millán B, Navarro C, Pittmann A, Reilly MM, Houlden H. *SBF1* mutations associated with autosomal recessive axonal neuropathy with cranial nerve involvement. *Neurogenetics*. 2017 Jan;18(1):63-67

Manole A, Männikkö R, Hanna MG, SYNAPS study group, Kullmann DM, Houlden H. De novo *KCNA2* mutations cause hereditary spastic paraplegia. *Ann Neurol*. 2017 Feb;81(2):326-328.

Chelban V, **Manole A**, Pihlstrøm L, Schottlaender L, Efthymiou S, O'Connor E, Meissner WG, Holton JL, Houlden H. Analysis of the prion protein gene in multiple system atrophy. *Neurobiol Aging*. 2017 Jan;49:216.e15-216.e18.

Efthymiou S, **Manole A**, Houlden H. Next-generation sequencing in neuromuscular diseases. *Curr Opin Neurol*. 2016 Oct;29(5):527-36.

Manole A, Chelban V, Haridy NA, Hamed SA, Berardo A, Reilly MM, Houlden H. Severe axonal neuropathy is a late manifestation of *SPG11*. *J Neurol*. 2016 Nov;263(11):2278-2286

Mestre TA, **Manole A**, MacDonald H, Riazi S, Kraeva N, Hanna MG, Lang AE, Männikkö R, Yoon G. A novel *KCNA1* mutation in a family with episodic ataxia and malignant hyperthermia. *Neurogenetics*. 2016 Oct;17(4):245-249

Kara E, Tucci A, Manzoni C, Lynch DS, Elpidorou M, Bettencourt C, Chelban V, **Manole A**, Hamed SA, Haridy NA, Federoff M, Preza E, Hughes D, Pittman A, Jaunmuktane Z, Brandner S, Xiromerisiou G, Wiethoff S, Schottlaender L, Proukakis C, Morris H, Warner T, Bhatia KP, Korlipara LV, Singleton AB, Hardy J, Wood NW, Lewis PA, Houlden H. Genetic and phenotypic characterization of complex hereditary spastic paraplegia. *Brain*. 2016 Jul;139(Pt 7):1904-18.

Manole A, Houlden H. (2015) Riboflavin transporter deficiency neuronopathy. In: Pagon RA, Adam MP, Ardinger HH, Wallace SE, Amemiya A, Bean LJH, Bird TD, Fong CT, Mefford HC, Smith RJH, Stephens K, editors. *GeneReviews®* [Internet]. Seattle (WA): University of Washington, Seattle; 1993-2016. Jun 11.

Koutsis G, Lynch D, **Manole A**, Karadima G, Reilly MM, Houlden H, Panas M. Charcot-Marie-Tooth disease type 2C and scapulooperoneal muscular atrophy overlap syndrome in a patient with the R232C TRPV4 mutation. *J Neurol*. 2015 Aug;262(8):1972-5.

Manole A, Fratta P, Houlden H. Recent advances in bulbar syndromes: genetic causes and disease mechanisms. *Curr Opin Neurol*. 2014 Oct;27(5):506-14

Chapter 1 General introduction

The human nervous system is a complex network of pathways that allows us to successfully interact with our environment. It can be divided into two parts: the central nervous system (CNS), which includes the brain, brainstem, and spinal cord, and the peripheral nervous system (PNS) that consists of the individual cranial, motor, and sensory nerves. The main function of the PNS is to transfer information to and from the CNS. The correct development and maintenance of this intricate structure relies on the coordinated action of a large number of genes, often with precise spatial and temporal patterns of expression.

Neurological disorders are diseases of the PNS or CNS that may present with heterogeneous symptoms according to the parts of the system involved in these pathologic processes. There are more than 600 diseases of the nervous system, such as epilepsy, Parkinson's disease and stroke as well as less common ones such as frontotemporal dementia.

Many neurological diseases share pathological processes that require an understanding of genetics and advances in this area have had an enormous impact on the field of the inherited neurological disorders. This can mainly be attributed to progress in technology development and affordability of next-generation sequencing (NGS), moving from polymerase chain reaction (PCR) in the 1980s to exome (protein-coding sequences) and gene panels in 2010 to the emerging use of genome sequencing in 2015 (Efthymiou et al., 2016) (Figure 1-1). In particular, the study of rare Mendelian disorders is able to provide unique insights into neurological disorders that may seem unrelated. Mendelian phenotypes can reveal the metabolic pathways involved in these disorders and networks of functionally related proteins that may be implicated in the development of multifactorial traits. These are also well suited for NGS, given the extreme heterogeneity and the large number of disease genes.

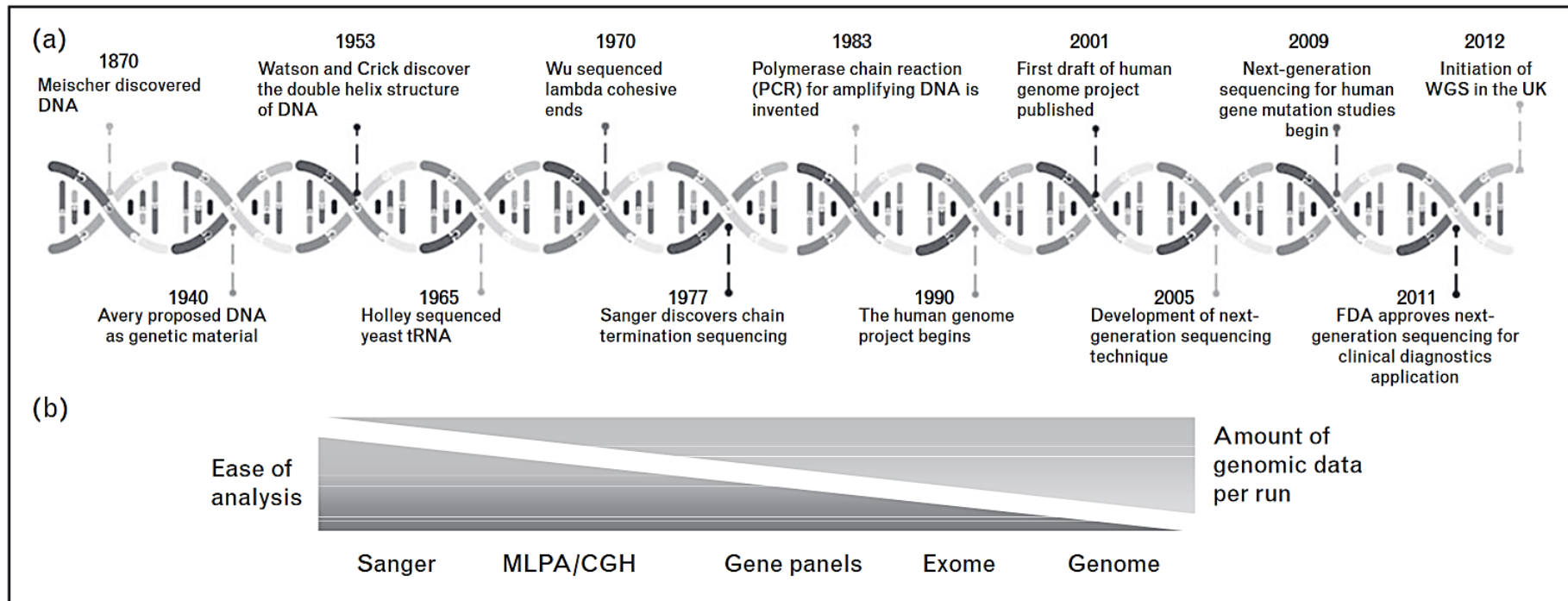


Figure 1-1 Overview of the history of genomics.

(a) A timeline depicting the key events in the history of genomics. Genetic research and the involvement of new technologies have played a major role in the increase of the amount of DNA sequence generated per person per year at greater cost efficiency. WGS: whole genome sequencing; FDA: Food and Drug Administration. (b) Schematic representation comparing the ease of analysis compared with the amount of genomic data generated per run. MLPA: Multiplex ligation-dependent probe amplification; CGH: Comparative Genomic Hybridization. Modified from (Efthymiou et al., 2016).

Functional genetics and aims of this thesis

Within the last decade, molecular and genetic techniques have improved significantly, enabling us to generate high-throughput genetic data within significantly shortened timeframes. Large parts of the obtained data, however, remain difficult to interpret due to genotypic heterogeneity, phenotypic variability, and phenomena such as reduced penetrance and missing heritability. For another significant proportion of neurodegenerative diseases for which the genetic defect is known the underlying molecular and cellular pathogenic events and disease initiating cascades are not well understood. It is also challenging in some cases to create an appropriate disease model and the generated models might have inherent limitations (e.g. biological differences between animal and human organism).

An assortment of gene sequencing, silencing, deletion and heterologous expression techniques have enabled more elaborate studies on the genetic bases of biological processes. These techniques have helped assess the functional consequences of genetic variants and determine their pathogenicity. Figure 1-2 details the different methods that can be used in order to study the functional genetics underlying neurological disorders. The study of the insect model *Drosophila melanogaster* is particularly helpful for this purpose. In the last decades it has been adopted as a main model for the study of the genetic and molecular bases of behaviour and so it is central to current neuroscience (Riemensperger et al., 2016). In Chapter 3 of this thesis work is presented that utilizes *Drosophila* to model a riboflavin responsive neuropathy.

Other methods such as RT-PCR and Western blot can be used to check for the levels of RNA and protein respectively when a transcript change is suspected (Figure 1-2; Chapter 5). These methods are however semi-quantitative and only give minimal information when there is a loss-of-function effect.

Another approach is to utilize cell types that lack endogenous proteins which would confound results and are amenable to genetic transfection or are large enough to be directly injected with genetic material. The *Xenopus* oocyte was one of the first heterologous expression systems proven to be useful for the study of the functional properties of ion channels and transporters (Miledi et al., 1982). It is still widely used

today, due to its large size, its faithful expression of channel proteins in the cell membrane, and the relative absence of endogenous channels which might complicate analysis of electrophysiology measurements (Mazzo et al., 2016). Although this assay is rapid and valuable tool to determine the pathogenicity of a potential mutation, it is not very helpful in determining the exact molecular consequences. In Chapters 6 and 7 of this thesis work is presented that utilizes *Xenopus* for functional studies of potassium channels.

For the field of neurology, the differentiation of human induced pluripotent stem cells (iPSCs) from healthy and diseased individuals into disease relevant neuronal cells permits for the first time *in vitro* study and modelling of human neurodevelopmental and neurodegenerative processes. It thereby holds the potential to significantly advance our understanding of pathological processes governing different developmental and degenerative diseases and thus to inform strategies aimed at stopping disease progression (Russo et al., 2015). Specific advantages of iPSCs include directed differentiation to any human cell type to model disease in a highly reductionist fashion (Jang and Ye, 2016). Furthermore, these cells will express mutations at pathophysiological level and contain the genetic background information of the diseased individual. For the fields of disease modelling this technique already has and might further reduce the amount of animal research in specific areas (Jang and Ye, 2016). Another long term promise of iPSCs will be patient-targeted individual therapy through transplantation. However, accurate restoration of circuit integrity and function after established damage, as well as surgical procedures and informative readouts to deliver and monitor these approaches, will be difficult challenges (Hawkins and Kotton, 2015). In Chapter 8 of this thesis work is presented that utilizes iPSC derived neurons to model episodic ataxia 1.

The overall aim of the thesis was to determine the functional consequences of gene mutations in rare neurological disease presenting with progressive or episodic neurological symptoms.

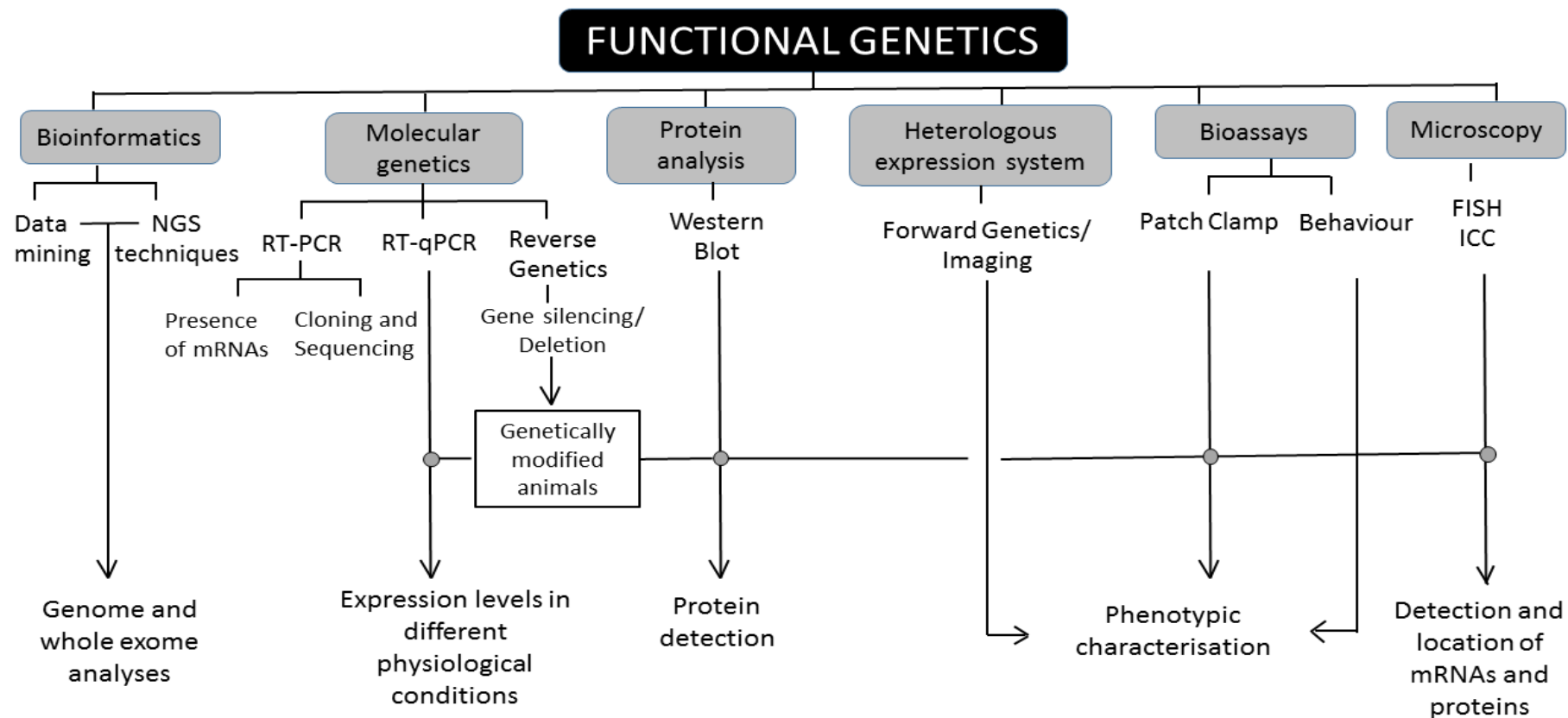


Figure 1-2 General workflow scheme for the study of functional genetics underlying neurological disorders.

FISH: fluorescence *in situ* hybridisation; ICC: immunocytochemistry; NGS: next-generation sequencing; qPCR: quantitative polymerase chain reaction; RT: reverse transcription.

The peripheral nervous system

The PNS consists of 10 of the 12 cranial nerves and the spinal roots, becoming the peripheral nerves and exiting from the spinal cord. The peripheral nerves can be classified as belonging to either the afferent (taking information to the CNS) or efferent (away from the CNS) pathways. Spinal nerves contain both afferent and efferent information. Sensory nerve cells carry information to the CNS and motor nerve cells carry information from the CNS to organs in the whole body. The PNS can be broadly divided into the somatic and the autonomic nervous systems. The somatic nervous system terminates on the skeletal muscle whereas the autonomic nervous system supplies all structures other than the skeletal muscle (e.g. glands and smooth muscle). Characteristic of the peripheral nerves are the long axons, extending to the extremities of the body. The axons can be both unmyelinated and myelinated and are organised in multiple bundles or fascicles (Lunn et al., 2016). The myelinated axons are surrounded by concentric layers of the Schwann cell plasma membrane which form the myelin sheath. The unmyelinated axons are surrounded by a single layer of the Schwann cell plasma membrane and cytoplasm. In the context of pathophysiological mechanisms that result in peripheral neuropathies, abnormalities can be found in both the axon and the myelin sheath, causing a diverse number of peripheral nerve diagnoses (Lunn et al., 2016).

Peripheral neuropathies

The causes of peripheral neuropathies can be multiple, such as hereditary, infectious, inflammatory, exposure to toxins, metabolic or traumatic and involve damage to sensory, motor or autonomic nerves. This can primarily target the axon (axonopathy), cell body (neuronopathy), or myelin sheath/Schwann cells (myelinopathy). Demyelinating neuropathies result from defects in the development and functioning of Schwann cells and the myelin sheath they produce, leading to secondary axonal degeneration (Hughes, 2008). The term mononeuropathy is used for single nerve defects and it is usually due to localised trauma or infection. The myelin sheath or part of the axon can be damaged due to long-term pressure on a nerve due to swelling or injury. Carpal tunnel syndrome, an acquired source of neuropathy usually caused by nerve

compression, is an example of a mononeuropathy as a single peripheral nerve is damaged (Hughes, 2008).

Multiple mononeuropathy or mononeuritis multiplex is characterised by two or more nerves being affected simultaneously or sequentially where the pattern is asymmetric. These can be caused by multiple medical conditions, such as diabetes mellitus or lupus erythematosus and are sometimes difficult to distinguish from the polyneuropathies when their progress becomes more symmetrical (Shakher and Stevens, 2011).

The term polyneuropathy is used to refer to conditions where multiple nerves in all limbs are involved, for example in Charcot-Marie-Tooth (CMT) disease and chronic inflammatory demyelinating polyneuropathy (CIDP) (Hughes, 2008).

Peripheral neuropathy is often length-dependent and therefore affects the longest nerves first. This translates to symptoms starting in the feet and progressing to the hands and more proximal areas later on in the disease course. However, hereditary motor neuropathy due to mutations in glycyl-tRNA synthetase (*GARS*) is characterised by upper limb predominance of symptoms, while heat shock 27 kDa protein 1 (*HSPB1*) and heat shock 22 kDa protein 8 (*HSPB8*) mutations cause length-dependent neuropathy, where the legs are more affected than the arms (Reilly et al., 2011).

Symptoms vary depending on the type of nerve which is damaged. In sensory loss there is neuropathic pain and tingling, burning, or numbness sensations (Hughes, 2008). Fasciculations and muscle weakness are caused by impairment to motor nerves and autonomic nerve damage involves changes in blood pressure, bladder function and sexual function (Shakher and Stevens, 2011).

Severity of disease varies greatly; some patients with peripheral neuropathy may be asymptomatic and disease may be evident only from electrophysiological tests. At the other end of the spectrum, some patients may require wheelchairs for mobility and ventilatory support, ultimately leading to susceptibility to infections such as chest infections that can be fatal (Reilly et al., 2011). In neuropathies such as CIDP, hereditary neuropathy with liability to pressure palsies (HNPP), porphyria and Refsum's disease, patients may experience periods of disease exacerbation characterised by intermittent relapses. Disease may be acute, sub-acute or chronic. Most polyneuropathies show a slowly progressive course (Delemotte et al., 2010).

There is currently no effective treatment to reverse the damage in most peripheral neuropathies. Corticosteroids, plasmapheresis or intravenous immunoglobulins (IVIg)

may be helpful in CIDP patients and in some CMT cases presenting with an overlapping inflammatory neuropathy (Ginsberg et al., 2004). Patients may benefit from physical therapy, use of orthotics, orthopaedic interventions, pain management and genetic counselling (Reilly et al., 2011).

Peripheral neuropathy may be the principal manifestation of disease, such as in CMT or part of a more generalized disorder as in Brown-Vialetto-Van Laere syndrome (BVVLS), hereditary spastic paraplegia (HSP), hereditary ataxia, neuroaxonal dystrophy (NAD), the genetic forms of porphyrias, metachromatic leukodystrophy, Krabbe disease, Tangier disease, Fabry disease, Refsum's disease and others (Reilly and Shy, 2009). Neuropathy may be acquired or inherited.

Acquired peripheral neuropathies

Chronic alcoholism is also frequently associated with acquired neuropathies. Other diseases also cause peripheral neuropathy, for example viral or bacterial infections such as Lyme disease, Hepatitis B and C, HIV/AIDS and varicella-zoster, and some autoimmune diseases including vasculitis due to rheumatoid arthritis, celiac disease, CIDP and multifocal motor neuropathy (Martyn and Hughes, 1997). Diabetes and leprosy are the most common cause of acquired neuropathy in the developed and developing world respectively. Other causes include tumours, which may apply excessive pressure on a nerve, or traumatic injury to a nerve due to an accident or compression (Martyn and Hughes, 1997). Finally, nutritional deficiencies in vitamin B₁, B₂, B₆, B₁₂ and E, as well as disease of the kidney or liver can cause neuropathy (Hughes, 2008).

Inherited peripheral neuropathies

Diseases where peripheral neuropathy is part of the phenotype include CMT, BVVL, neuroaxonal dystrophy, HSP, hereditary ataxia, Fabry disease, Refsum's disease and others (Reilly & Shy, 2009). Chapter 3 of this thesis provides a detailed investigation into the genetic and functional aspects of BVVLS, a neuronopathy which often presents with a CMT-like sensory-motor neuropathy as part of a more widespread disorder. Chapters 4 and 5 look at particular examples of CMT genetics.

The cerebellum

The cerebellum receives information from the sensory systems, the spinal cord, and other parts of the brain and then regulates motor movements. It coordinates voluntary movements such as posture, balance, coordination and speech, resulting in smooth and balanced muscular activity (Buckner, 2013). Although the cerebellum accounts for approximately 10% of the brain's volume, it contains over 50% of the total number of neurons in the brain (O'Halloran et al., 2012).

It is situated in the posterior fossa of the skull beneath the occipital pole of the cerebral hemispheres, dorsal to the brainstem. It is composed of a 1 mm layer of cortex that forms a continuous layer over the entire outer surface, with a longitudinal band of less dense cortex, the vermis, forming a medial divide (O'Halloran et al., 2012). The anterior and posterolateral fissures divide the cerebellum into three anatomically distinct lobes: the anterior, posterior, and flocculonodular lobes (Buckner, 2013). Blood is supplied to the cerebellum by three arteries, arising from the vertebrobasilar system: the superior cerebellar artery, the anterior inferior cerebellar artery, and the posterior inferior cerebellar artery (Buckner, 2013).

The cerebellum is subject to a range of pathological conditions, including hereditary ataxias, degenerative conditions, tumours, and stroke (Buckner, 2013).

Cerebellar ataxias

The cerebellar ataxias comprise a wide spectrum of neurological disorders with ataxia as the main symptom. Ataxia results from the involvement of cerebellar structures or from a combination of cerebellar and extra-cerebellar lesions, especially due to brainstem involvement (Manto and Marmolino, 2009).

Multiple system atrophy (MSA) is the most common nonhereditary degenerative ataxia (Dayal et al., 2017). The disease usually starts around 55 years. The latest criteria retain the diagnostic categories of MSA with parkinsonism and MSA with predominant cerebellar ataxia to designate the presentations of the disease (Laurens et al., 2017). Other examples of sporadic and acquired nonhereditary ataxias include: idiopathic late-onset cerebellar ataxia, stroke, toxic induced, immune-mediated, traumatic and neoplastic disorder (Manto and Marmolino, 2009).

The hereditary ataxias are a highly heterogeneous group of disorders phenotypically characterized by gait ataxia, incoordination of eye movements, speech, and hand

movements, and are frequently associated with atrophy of the cerebellum (Sun et al., 2016).

The hereditary ataxias can be subdivided first by mode of inheritance (autosomal dominant, autosomal recessive, X-linked, and mitochondrial) and secondarily by the gene in which pathogenic variants occur or chromosome locus to which the phenotype has been mapped (Jayadev and Bird, 2013). Spinocerebellar ataxia (SCA) is a historical term first used in the 1950s based on Friedreich ataxia as a model. SCA now refers to autosomal dominant hereditary ataxia where the numbers are assigned in the order in which the disease was identified (Sun et al., 2016). There are more than 35 autosomal dominant types frequently termed spinocerebellar ataxia and typically having adult onset (see review (Jayadev and Bird, 2013)). SCAR refers to autosomal recessive spinocerebellar ataxias. Autosomal recessive ataxias usually have onset in childhood; the most common subtypes are Friedreich, ataxia-telangiectasia, ataxia with oculomotor apraxia type 1, and ataxia with oculomotor apraxia type 2 (Manto and Marmolino, 2009). Four autosomal recessive types have dietary or biochemical treatment modalities (ataxia with vitamin E deficiency, cerebrotendinous xanthomatosis, Refsum, and coenzyme Q10 deficiency), but there are no specific treatments for other ataxias. EA refers to episodic ataxias.

Episodic ataxias

Hereditary episodic ataxia represents a group of monogenic disorders characterized by recurrent episodes of vertigo and ataxia, variably associated with progressive ataxia (Jen et al., 2007). The number of phenotypes and genotypes is expanding (Table 1-1). Nearly all episodic ataxia mutations identified so far occur in individuals with onset early in life (Jen et al., 2007). This thesis focusses on EA1 for which a more detailed introduction is provided in Chapter 7.

Table 1-1 Molecular genetics and clinical features of episodic ataxias

Modified from Jayadev and Bird, (2013).

Disease	Gene / Locus	Distinguishing Clinical Features	OMIM Links
EA1	<i>KCNA1</i>	<ul style="list-style-type: none"> ➤ Gait ataxia ➤ Myokymia ➤ Attacks lasting seconds to minutes; startle or exercise induced ➤ No vertigo 	160120
EA2	<i>CACNA1A</i>	<ul style="list-style-type: none"> ➤ Gait ataxia ➤ Nystagmus ➤ Attacks lasting minutes to hours; posture change induced ➤ Vertigo ➤ Later, permanent ataxia 	108500
EA3	1q42	<ul style="list-style-type: none"> ➤ Adult onset ➤ Vertigo ➤ Tinnitus 	606554
EA4	--	<ul style="list-style-type: none"> ➤ Adult onset ➤ Cerebellar pathology documented 	606552
EA5	<i>CACNB4</i>	<ul style="list-style-type: none"> ➤ Childhood to adolescent onset 	613855
EA6	<i>SLC1A3</i>	<ul style="list-style-type: none"> ➤ Seizures ➤ Migraine ➤ Childhood onset 	612656
EA7	19q13	<ul style="list-style-type: none"> ➤ Vertigo ➤ Weakness ➤ Seizures ➤ Childhood to adolescent onset 	611907
Episodic ataxia with neonatal epilepsy	<i>SCN2A</i>	<ul style="list-style-type: none"> ➤ Neonatal epilepsy ➤ Later-onset episodic ataxia ➤ Autism ➤ Hypotonia ➤ Dystonia 	613721
CAPOS syndrome	<i>ATP1A3</i>	<ul style="list-style-type: none"> ➤ Cerebellar ataxia ➤ Areflexia ➤ Pes cavus ➤ Optic atrophy ➤ Sensorineural hearing loss ➤ Also alternating hemiplegia 	601338

Specific diseases are described in further detail in the introductory sections of Chapters 3 to 8.

Thesis outline

The work described in this thesis used a combination of genetic techniques together with functional studies to study several rare neurological disorders. The results from the present work advance the understanding, and potential treatment, of a group of neurological disorders caused by single gene defects

Chapter 2 gives a detailed account of general methods used extensively through the thesis. Initial work in Chapter 3 expands the clinic-genetic spectrum of riboflavin responsive neuropathy, and this leads to a series of experiments to identify the consequences on mitochondrial function of the loss of function effect. Next clinical case histories and undertake pathological evaluation of brain and spinal cord of two patients are reviewed. Finally, using a *Drosophila* model of the disease, the *in vivo* consequences of this disease are investigated, and whether these can be mitigated by supplementation with a riboflavin derivative is tested.

In Chapter 4, novel variants in *SBFI* as the potential causative mutations in two siblings with severe axonal neuropathy, hearing loss, facial weakness and bulbar features are identified. Chapter 5 describes novel frameshift mutations in *SPG11*, identified by whole exome sequencing, segregating with the disease and investigated using mRNA. The causative mutations were associated with the late manifestation of severe axonal neuropathy. In Chapter 6, a *de novo* missense mutation within the Kv1.2 voltage sensor associated with HSP and ataxia is reported. Chapter 7 describes the electrophysiological consequences of F249C mutation in Kv1.1 associated with EA1 and malignant hyperthermia and finally in Chapter 8, induced pluripotent stem cell derived neurons are used to determine the neuronal consequences of the Kv1.1 mutation.

Chapter 2 General methods

Patient cohorts

Patients were enrolled with informed consent from the patient and/or parental guardian. DNA was collected from cases presenting with diverse rare inherited neurological disorders at medical centres in England (including from patients originating from Pakistan, India, Saudi Arabia, Kuwait, Iran and Turkey) as well as from medical centres in Wales, Scotland, Northern Ireland, Ireland, France, Belgium, the Netherlands, Greece, Malta, Russia, Lebanon, Iceland, Australia and the United States. Clinical assessment of the patients was performed by consultants.

DNA extraction from blood samples

DNA extraction from blood was performed with the QIAamp DNA Blood Midi/Maxi kit according to the manufacturer's instructions (Qiagen) by the diagnostic department. The concentration of the DNA samples was then measured by nanodrop spectroscopy (Nanodrop ND-1000, ThermoFisher) and adjusted to 50 ng/ μ L for subsequent use. The 260/280 nm absorbance ratio was used as a quality indicator.

Primer design

Primers were designed using the default parameters in Primer3 (<http://primer3.ut.ee/>) as follows. Each exon's nucleotide sequence was inputted separately in the program, along with approximately 100 bp flanking sequence from each of the upstream and downstream intron. The DNA sequence was extracted from the suitable transcript downloaded from ensembl (<http://www.ensembl.org/index.html>) (usually the longest coding transcript with a consensus coding sequence identifier (ID)). The target region that should definitely be included in the polymerase chain reaction (PCR) product (which is the exon and approximately 50 bp flanking intronic regions) was selected. All generated primer pairs were checked for the presence of SNPs through ensembl. Primer pairs overlapping SNPs were discarded. Where an exon was too long (over 600 bp), primers were either designed for two separate amplicons or for the single amplicon with additional mid-amplicon primers for use in sequencing reaction. When two neighbouring exons were separated by a short intron (<200 bp), primers were designed

amplifying them as a single amplicon. The primers were ordered from Sigma in lyophilised form and were subsequently dissolved in autoclaved, double distilled water (ddH₂O) as per manufacturer instructions after centrifuging the tubes to ensure minimal loss of lyophilised material upon opening of the tubes. The stock solutions were diluted to a final working concentration of 10 μ M.

Polymerase chain reaction

All coding exons and flanking intronic regions of the studied genes were amplified by PCR and sequenced by Sanger sequencing (dideoxyterminator nucleotide reaction). First, primers were optimised using control DNA to ensure efficiency of the reaction, which was confirmed through agarose gel electrophoresis. For the PCR reaction, 12.5 μ l of Roche fast start PCR master mix (Roche, UK), 0.75 μ l of forward primers (10 μ M), 0.75 μ l of reverse primers (10 μ M) and 10 μ l of double distilled water were added to 1 μ l of genomic DNA of a concentration of 50 ng/ μ l. Most PCR reactions with the Primer3 designed primers worked with the following program: 95^oC for 5 min, followed by eight cycles of denaturing at 95^oC for 20 s, annealing at 70^oC for 20 s, and extending at 72^oC for 30 s. 20 further cycles of the same conditions were run except the annealing temperature was decreased by 0.5^oC per cycle until the final annealing temperature reached 65^oC. Finally, 12 cycles were run with denaturing at 95^oC for 20 s, annealing at 50^oC for 20 s and extending at 72^oC for 30 s. The reaction underwent a final extension at 72^oC for 5 min. If the PCR was unsuccessful, we added various amounts of DMSO and/or used lower annealing temperatures for the PCR. If none of these combinations worked different cyler programs and/or new primers were used.

Agarose gel electrophoresis

Agarose gel electrophoresis was used to determine whether a PCR was successful. To prepare a 1% agarose gel, 100 ml of 1x Tris/Borate/ Ethylenediaminetetraacetic acid (EDTA) (TBE) were mixed with 1 g of agarose and heated in the microwave oven for 2 min. When the solution was transparent and was hand hot 10 μ l of gel red dye was added and mixed by shaking until the solution was homogeneous. This solution was then poured in a gel casting mould after adding the combs and was left to set.

We mixed 7 μ l from each PCR product with 3 μ l of Orange G dye and loaded this mix for each sample in one well of the gel. We also added 7 μ l of DNA ladder (Quick-Load® 2-Log DNA Ladder (0.1-10.0 kb)) in the first well and ran the gel in TBE at 100 V for 30 min. The DNA bands were visualised under UV light.

PCR purification

PCR purification was performed using the Exosap method. For this we prepared a stock solution including 50 μ l Exo I enzyme, 200 μ l FastAP Thermosensitive Alkaline Phosphatase (1 U/ μ L; Thermo Scientific) and 750 μ l ddH₂O. We added 2.8 μ l of this solution to 7 μ l of PCR product and placed the plate in the thermocycler following using this programme: 37°C for 30 min then 80°C for 15 min. We then used 3.5 μ l of this reaction for bidirectional sequencing.

Sanger sequencing

For the sequencing reaction, 2 μ l of sequencing buffer (BigDye terminator v1.3 Cycle sequencing kit, Applied Biosystems, USA), 2 μ l of primers forward or reverse (5 pM), 1.5 μ l of ddH₂O, and 0.5 μ l of BigDye (BigDye terminator v3.1 Cycle sequencing kit, Applied Biosystems, USA) were added to 3.5 μ l of purified PCR product. Both forward and reverse strands were sequenced and conditions were as follows: 25 cycles of denaturation at 95°C for 10 s, annealing at 50°C for 5 s and extension at 60°C for 4 min. For purifying we used the Sephadex method: 40 ml distilled autoclaved H₂O was mixed 2.9 g Sephadex in 50 ml tube. The resin was allowed to hydrate at room temperature for 30 min prior to usage. 350 μ l of Sephadex suspension was added per well of a Cornig glass plate placed on an empty collection plate. This was centrifuged at 700 g for 3min. The sequencing reaction product was added to the Cornig plate that was placed over a non-skirted plate. The plate was then centrifuged at 910 g for 5 min, resulting in purified sequencing reaction product in the non-skirted collection plate. We added ddH₂O to any empty wells of the non-skirted plate prior to placing in the sequencing machine. Each Cornig plate can be used up to five times, after cleaning as follows: Sephadex columns are disposed of then the plate is rinsed 4 times with ddH₂O and centrifuge at 910 g for 3 min to remove the residual water. Sequencing reaction products were read by the ABI 3730xl DNA Analyser (Applied Biosystems, USA), which uses a capillary

electrophoresis system, and the sequencing results were analysed using the SeqScape software version 3 (Applied Biosystems). Where a possible pathogenic mutation was found, the PCR and sequencing of the appropriate exon were repeated in both the forward and reverse directions for the sample in question. Samples that had poor quality sequencing were repeated.

Whole-exome sequencing

Exome sequencing was performed in-house with the HiSeq 2500 by Dr Deborah Hughes at the Institute of Neurology, UCL. Enrichment of coding exons and flanking intronic regions was carried out with the use of the Illumina's TruSeq Exome Enrichment Kit in combination with HiSeq2500 sequencing. Preliminary data analysis including image analysis, base calling, alignment and variant calling, copy number variations and structural variations was performed in-house by Dr Alan Pittman. After removal of PCR duplicates using Picard (<http://picard.sourceforge.net>) as well as reads without a unique mapping location, variants were extracted using the Maq model in SAMtools and filtered by the following criteria: consensus quality >30, SNP quality >30 and root mean square mapping quality >30. These variants were further filtered against the dbSNP 135 and 1000 Genomes databases by use of Annovar (<http://www.openbioinformatics.org/annovar/>). The data filtering from this step onwards was carried out by the researchers as described in Figure 2-1. For most exomes analysed where data from another affected sibling was available it was filtered such that only common variants were displayed. Synonymous SNPs were excluded and the appropriate disease model was applied to the remaining list of variants. Further prioritising of variants was done by combining linkage analysis results or based on individual gene function and expression. *In silico* predictions of pathogenicity and conservation between species were assessed and details of gene expression in various tissues and location of the mutated amino acid within the protein were examined to prioritise candidate gene lists.

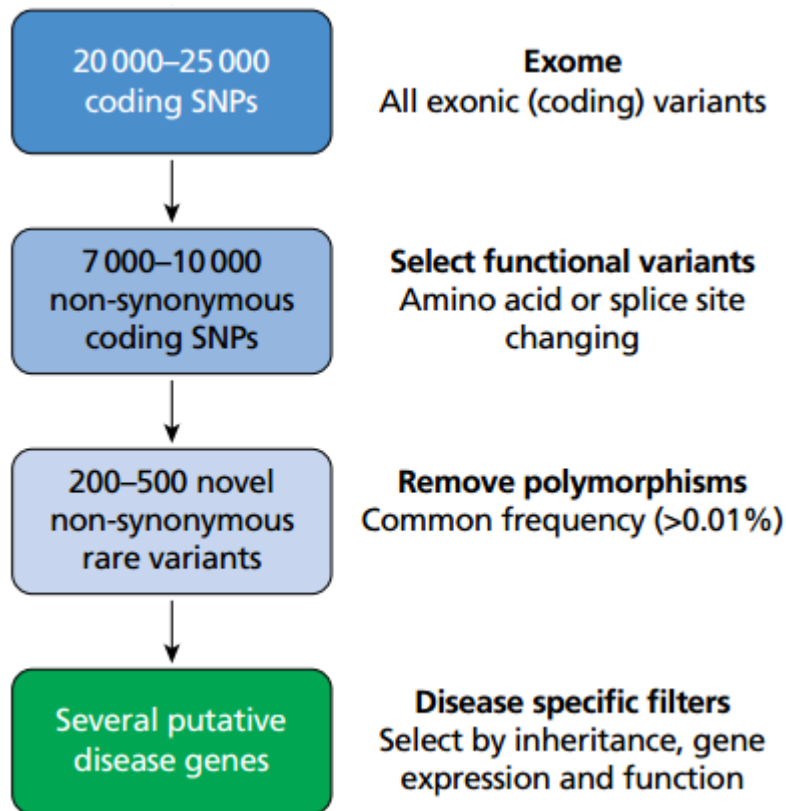


Figure 2-1 Filtering strategy for whole exome sequencing data.

SNP, single nucleotide polymorphism. Modified from (Kullmann et al., 2016).

Some areas may not be covered fully by the hybridisation probe design, leading to a variable number of independent reads at a particular base pair known as the read depth. Therefore, gene coverage and read depths of known disease-associated genes and candidates genes were determined by checking the binary format for the sequence data. A base was considered poorly covered if it had less than 15-20 times coverage. These were still included in the analysis but were regarded as potentially false positives until confirmed by Sanger sequencing. All possible candidates were checked by Sanger sequencing.

Mutation nomenclature

The variations discussed in this thesis are named based on published cDNA sequences, using standard nomenclature from the Human Genome Variation Society (<http://varnomen.hgvs.org/>). Variations mentioned in the text are written with respect to both the nucleotide change and amino acid change (denoted by ‘c.’ and ‘p.’

respectively), and subsequently one or three letter amino acid change is used. Variations in tables and figures are written in the protein form unless otherwise specified.

Cell culture

Fibroblasts cell culture

Fibroblasts were grown at 37°C in 95% air and 5% CO₂. Unless otherwise specified, cells were maintained in Dulbecco's modified eagle medium (DMEM)-GlutaMAX (high glucose and pyruvate; Life Technologies) with 10% v/v foetal bovine serum (FBS; heat-inactivated, non-USA origin; Life Technologies) and in 75 cm² tissue culture flasks. The medium was changed every four days. Cultures were passaged when cells reached 80% confluence. To split or freeze cells, the medium was removed from the flask. Cells were washed with 5 ml of 1x Dulbecco's phosphate buffered saline (dPBS; Life Technologies). 1 ml of 0.05% 1x trypsin-EDTA (Life Technologies) was added and cells were placed back in the incubator at 37°C for 5 min. 7 ml of medium was added to the flask to quench the trypsin, and cells were collected and centrifuged at 300 g for 5 min. The supernatant was discarded. To split cells, the cell pellet was resuspended in medium and split into new flasks as appropriate. To freeze cells, the cell pellet was resuspended in cold freezing medium containing 10% DMSO and 90% FBS and placed in labelled cryovials (two cryovials per 80% confluent 75 cm² flask). Cells were first frozen at -80°C in an isopropanol freezing container for 24 h and then were transferred to liquid nitrogen for long-term storage. Cells were defrosted quickly in a 37°C water bath and seeded at a density of 5 x 10³ cells/cm² into 75 cm² tissue culture flasks. To obtain reproducible results, only fibroblasts of passage number 2 to 10 were used in experiments.

Induced pluripotent stem cell culture

iPSCs were maintained as feeder-free cells on Geltrex (Life Technologies, A1413302) in 6 well plates. Essential 8 media (Life Technologies, A1517001) was exchanged daily and cells were split using UltraPure™ 0.5mM EDTA (Life Technologies, 15575-020) in dPBS upon reaching 70% confluency. Briefly cells were washed with 2 ml of dPBS and 1 mL of 0.5 mM EDTA was added and the cells were visualized under phase-contrast microscope to closely monitor the progress of the incubation at room temperature. When the cells began to separate uniformly throughout the entire colony

the EDTA was removed and the media was added to dissociate the cells and then these were plated at a 1:5 split ratio. For freezing cells were dissociated as before but 1 ml of freezing media was added (10% (vol/vol) DMSO in full E8 medium). For one well from a six-well plate with 70–80% confluence, we froze two vials. Cells were first frozen at -80°C in an isopropanol freezing container for 24 h and then were transferred to liquid nitrogen for long-term storage. To thaw cells, the cryotube was taken out of the liquid nitrogen tank and place it directly in a 37°C water bath. When only a small ice particle was floating, the cells were transferred into a 15-ml conical tube. 10 ml of E8 medium was added dropwise while continuously mixing the solution in the tube. Cells were centrifuged at 200 g for 5 min. The supernatant was aspirated and E8 medium was used to resuspend the cells. ROCK inhibitor (10 µM; Bio Vision) was added into E8 medium and the cells were plated. All procedures were carried out in accordance with recommendations of iPSC culture (Life Technologies, Publication Number MAN0007035). Two passages before usage for differentiation the media was switched to mTeSR™1 medium (Stem Cell Technologies) and Matrigel (BD Biosciences) for coating.

Neuronal cultures

All animal procedures were carried out according to the Animals (Scientific Procedures) Act 1986. Most times neurons were available from primary cortical cultures prepared by other workers (Dr Andres Vicente, Dr Erica Tagliatti or Dr Philippe Mendonça). If not available, P0 mice were decapitated and heads were washed in 3x25 ml of Wash buffer (Hank's Balanced Salt Solution (HBSS, Sigma, H9394) + 5 mM HEPES (pH 7.3, Invitrogen, 15630056)). The brain was removed and cortices were isolated with the use of fine tweezers. Isolated cortices were rinsed 5 times with 5 ml Wash buffer and were then digested with trypsin type XI (1 mg/ml; Sigma, T1005) and 1% (w/v) DNase I (Sigma, D5025-150 KU) for 10 min at 37°C. Trypsinisation was stopped by adding 5 ml of Dissection solution (Wash buffer + 20% Fetal Bovine Serum (FBS, Invitrogen, 10082147)). Cells were mechanically dissociated using a series of fine Pasteur pipettes. Dissociated neurons were plated in 24-well plates at a density of 50,000 cells/well on iPSC derived neurons in Neurobasal culture medium (Invitrogen, 10888022) with B27 supplement (1x; Invitrogen, 17504044) and glutamine (25 µM; Invitrogen, 35050038) and cultured at 37°C and in 5% CO₂.

Cell counting

To establish the number of cells in 1 ml of cell suspension prior to cell seeding, a 10 μ l sample of suspension was added to 10 μ l of 0.4% Trypan Blue (Sigma). The solution was pipetted onto a haemocytometer and the number of live cells (colourless and bright) in 4 sets of 16 corner squares of the grid was counted under a light microscope. The total count was averaged and multiplied by two to adjust for the 1:2 dilution in Trypan Blue. The resulting value $\times 10^4$ is equivalent to the number of cells per ml of suspension.

***Drosophila* husbandry**

The life cycle of the fly is 10 days at 25°C and 21 days at 18°C. Flies were reared on standard fly food consisting of corn meal, yeast, sucrose, glucose, wheat germ, soya flour, nipagin and propionic acid. Fly stocks were turned over every 14 days if they were reared at room temperature, and every 30 days if they were being reared at 18°C. Crosses were reared at 25°C. Females for crosses were virgins and these remain virgins for ~6 h at 25°C, and for ~18 h at 18°C. Virgins were collected by use of a twice a day procedure in which vials were cleared in the morning, placed at 25°C for 6 h, then the females (who should all be virgins) were collected and the vials were placed at 18°C. Virgins are light coloured and could be identified by the presence of a dark spot in their abdomens. For setting up crosses, ~3 females, and 3 males were used per vial.

Quantification of flavins in *Drosophila*

Approximately 10 virgin females flies per strain were homogenized in isolation buffer (320 mM sucrose, 1 mM EDTA and 10 mM Trizma-base, pH to 7.4) then stored at -80°C. Riboflavin, FMN and FAD content were measured in neutralized perchloric extracts by means of HPLC as follows: separation was achieved by means of a reverse-phase HPLC (Chromsystems) including Jasco PU-980 intelligent pump (SpectraLab Scientific), FP-2020 Plus Jasco fluorescence detector and Azur data capture system (Kromatek, UK). Quantitative determination of riboflavin, FMN, and FAD was carried out using the Whole Blood Chromsystems vitamins B1/B2 kit (Chromsystems, Germany) as per the manufacturer's protocol. The Bio-Rad DC protein assay (Bio-Rad Laboratories, USA) or a Lowry assay was used to normalise for protein concentration.

Assessment of activities of mitochondrial electron transport chain complexes

Approximately 10 virgin female flies per strain were homogenized in isolation buffer then stored at -80°C for subsequent measurements.

Complex I activity

The measurements were taken in an Uvikon 941 spectrophotometer (Northstar Scientific, UK). The method used to measure complex I activity (30°C) was based on a modification of the method of Ragan (1987), which involved monitoring the oxidation of NADH at 340 nm. Samples were added to polystyrene cuvettes containing the assay buffer (10 mM MgCl₂ and 25 mM potassium phosphate, pH 7.2), 0.15 mM NADH, 2.5 mg of bovine serum albumin, and 1 mM KCN (to inhibit complex IV), giving a final volume of 1 ml. Ubiquinone (50 μM) was added to start the reaction, and rates were monitored for 6–7 min. Rotenone (20 μM) was then added to inhibit complex I activity and to allow determination of the rotenone-insensitive rate for a further 5–6 min. The extinction coefficient used was $6.81 \times 10^3 \text{ M}^{-1} \text{ cm}^{-1}$.

Complex II activity

Complex II assay was modified from the method of Birch-Machin et al. (1994) and was measured by the succinate-dependent 2-thenoyltrifluoroacetone (TTFA) sensitive reduction of 2,6-dichlorophenolindophenol (DCPIP) at 600 nm. Briefly, the assay medium contained 50 mM potassium phosphate pH 7.4, 0.1 mM EDTA, 1 mM KCN, 10 μM rotenone, 20 mM succinate, 0.12 mM DCPIP and the sample. Coenzyme Q₁ (50 μM) was added to start the reaction, and the rates were monitored for 6–7 min. TTFA (1 mM) was added and the reaction measured for a further 7 min. The extinction coefficient used was $19.1 \text{ mM}^{-1} \cdot \text{cm}^{-1}$.

Complex II-III activity

Homogenized flies were stored at -80°C, then exposed to 3 cycle of freeze-thawing in liquid nitrogen. Complex II/III activity was determined using a modification of the method of King (1997) which followed the succinate dependent antimycin A sensitive reduction of cytochrome *c* at 550 nm. Samples were added to plastic cuvettes containing buffer (100 mM potassium phosphate, 0.3 mM potassium-EDTA, pH 7.4), 1 mM KCN,

and 100 μM cytochrome *c* with a final volume of 1 ml. The reaction was initiated by the addition of succinate (20 mM). After 7–8 min, antimycin A (10 μM) was added to inhibit complex III activity and to allow the determination of the antimycin A -insensitive rate.

Citrate synthase assay

Citrate synthase activity provides an estimate of mitochondrial content and was therefore used to normalise complex I and II activities for mitochondrial enrichment (Hargreaves et al., 1999). The activity of citrate synthase is measured by the formation of the anion of thionitrobenzoate from 5,5'-dithiobis(2-nitrobenzoate) (DTNB) and CoA at 412 nm (Shephard, 1969). The assay mixture contained 100 mM Tris-HCl/0.1% v/v Triton (pH 8.0), 0.25 mM DTNB, 0.1 mM acetyl-CoA and the sample. The reaction was started by addition of 0.2 mM oxaloacetate and monitored spectrophotometrically for 7 min. The extinction coefficient used was $13.6 \times 10^3 \text{ M}^{-1} \text{ cm}^{-1}$.

Adult behaviour

Adult flies were kept as groups of males and females in a LD cycle at 25°C for 1 day prior to testing. Single females were loaded into glass tubes (with 2% agar and 4% sucrose food) and monitored through the *Drosophila* Activity Monitoring System (Trikinetics) in LD at 25°C with an approximate intensity of 700-1000 Lux during the L condition. They remained on normal or supplemented food during the data acquisition. The *Drosophila* Activity Monitor measures the locomotor activity of 32 individual flies, each in a separate tube. As a fly walks back and forth within its tube, it interrupts an infrared beam that crosses the tube at its midpoint, and this interruption, detected by the onboard electronics, is added to the tube's activity count as a measure of fly activity. In a typical experiment, an agar/sucrose food mixture was placed into one end of each tube, followed by the fly, and the tube is sealed by a cotton plug. The 32 tubes are inserted into holes in the monitor case and centered. Over the course of the experiment, which may last for days or weeks, the counting circuits continuously monitor the activity in all 32 tubes, and at periodic intervals, upload their count totals to the host computer for storage and later analysis. This daily record provides a good measure of both the intensity of locomotor activity, and the relative periods of rest. A beam of infrared light passes through the middle of the tube and fly activities were deduced from beam-

breaking events. Locomotor activity was recorded in 30 min bins and an analysis was performed on the second day after loading. Data were pooled from at least two independent experiments. The average locomotor activity profile for each genotype was analyzed using Microsoft Excel. The relative locomotor activities per 30 min bin for individual flies were averaged for each genotype and also the average locomotor activity per day was calculated. In some cases the locomotor activity per 30 min bin was normalized by the average locomotor activity per day. Locomotion graphs were generated using GraphPad Prism 6 and Microsoft excel.

Molecular biology

Mutations were introduced into the corresponding cDNA using a site-directed mutagenesis procedure based on PCR with the proofreading *Pfu* DNA polymerase (Qiagen) [25 cycles of denaturation at 95°C (10 s), annealing at 50°C (5 s) and extension at 60°C (10 min)] followed by the digestion of the PCR reaction with 1 µl (10 U/µl) of DpnI at 37°C for 1 h. Primers were overlapping to the sequence of interest. A standard heat-shock transformation was carried out by adding 5 µL of the PCR product to 50 µL of competent *Escherichia coli* XL10 blue cells. Briefly, bacteria were transferred from ice heat-shocked for 45 s at 42°C and then immediately put back on ice for 2 min. 250 µl of pre-warmed S.O.C. medium (20 g/L tryptone 5 g/L yeast extract, 4.8 g/L MgSO₄, 3.603 g/L dextrose, 0.5g/L NaCl, 0.186 g/L KCl, Sigma) was added to each transformation reaction and cells were then shaken (225 rpm, IKA incubating 91 shaker) for 60 min at 37°C. The cells were streaked on Luria broth (LB) agar (1.8% agar) plates containing 100 µg/mL ampicillin and incubated overnight at 37 °C. Single colonies were picked and inoculated into 5 mL LB medium with 50 µg/mL ampicillin left shaking overnight at 200 rpm and 37 °C.

The plasmid DNA was purified using a QIAprep Spin Miniprep kit supplied by Qiagen. Plasmid DNA concentration was measured using a spectrophotometer (Nanodrop ND-1000, Thermoscientific). The 260/280nm absorbance ratio was used as a quality indicator. The DNA sample (100 ng/µl) was then sent for sequencing in the UCL facility and the mutation presence confirmed.

Plasmid DNA was linearised using a restriction enzyme specific to the plasmid (linearisation conditions are dependent on the enzyme used, see results Chapters 6 and 7 for details). The plasmid was subsequently linearized overnight at 37 °C and cleaned

using the QIAquick PCR Purification Kit according to the manufacturer's instructions. 2 µg of linearised DNA was used for transcription of RNA using Ambion T7 mMessage mMachine kit (Life Technologies) in a reaction mixture containing: 10 µl 2x NTP, 2 µl 10x reaction buffer, 2 µl enzyme mix and 2 µg of linear template DNA, made up to 20 µl with water. This reaction was incubated for 2 h at 37°C. Lithium chloride precipitation was then used for RNA extraction using the following method; 30 µl of H₂O and 30 µl of LiCl precipitation solution were added to the reaction, the mixture was placed at -20°C overnight, and centrifuged for 15 min at 13,000 rpm and 4°C. The supernatant was discarded and the pellet was washed by the addition of 500 µl of 70% ethanol, further centrifugation and removal of the supernatant. The resultant pellet was resuspended in 20 µl of RNase free H₂O. RNA concentration was measured using the nanodrop spectrometer.

***Xenopus* oocyte collection, preparation and injection**

Xenopus care and handling was in accordance with the highest standards of institutional guidelines. Frogs underwent no more than two surgeries separated by at least 3 weeks. Before surgery, frogs were anaesthetized with an aerated solution of 3-aminobenzoic acid ethyl ester.

Stage V-VI *Xenopus laevis* oocytes were harvested from female *Xenopus laevis* frogs within UCL and stored in Modified Barth's Saline (MBS) ((in mM): 96 NaCl, 2 KCl, 1 MgCl₂, 5 HEPES (pH 7.4 with NaOH)). All chemicals were from Sigma (St. Louis, MO). The follicular layer was removed by incubation with 1 mg/ml collagenase A (Roche diagnostics) in MBS for 90 min, removal of unhealthy oocytes, and further incubation with new collagenase. Healthy oocytes were selected and deposited into OR-2 media ((in mM): 82.5 NaCl, 2 KCl, 1 MgCl₂, 5 HEPES (pH 7.4 with NaOH)) with 100 U/ml penicillin- streptomycin and stored at 18°C.

Electrophysiology

Within 24 h of harvest oocytes were injected with RNA (RNA volume is experiment-dependent) using a Drummond Nanoject microinjector pipette (Drummond Scientific Company). 3.5'' glass capillaries (Nanolitre replacement tubes, Drummond Scientific) were formed using a multistage puller (Zeitz DMZ Universal Puller,

AutoMate Scientific). The tip was broken manually to create a sharp edge and the electrode backfilled with mineral oil (Sigma-Aldrich). RNA was microinjected into the oocyte cytoplasm and the oocytes incubated at 18°C in MBS containing (in mM): 96 NaCl, 1 KCl, 0.75 CaCl₂, 0.8 MgCl₂ and 10 HEPES (pH 7.4), with 50 U/ml penicillin G and 50 mg/ml streptomycin.

Experiments were carried out at room temperature (22–24°C), with continuous superfusion of oocytes with a solution containing (in mM): 96 NaCl, 2 KCl, 1.8 CaCl₂, 1 MgCl₂, 5 HEPES (pH 7.4).

Electrophysiological experiments were performed using the well-established two-electrode voltage-clamp (TEVC) technique (Stühmer, 1998). The TEVC was controlled by a GeneClamp 500B amplifier (Axon Instrument Foster City, CA, USA) and was used to record the currents produced by the *Xenopus* oocytes. The amplifier was controlled and signals recorded using pClamp 7 software together with a DigiData1200A A/D converter (Axon Instruments). Microelectrodes were fabricated from borosilicate glass (Harvard Apparatus) using a multistage puller (AutoMate Scientific) to an O.D of 3-5 µm for the voltage electrode and 7 -9 µm for the current electrode. The tip resistance of the electrodes were <2M Ω and <1M Ω respectively with both electrodes filled with 3M KCl. Data analysis was completed using Clampfit (from pCLAMP 9.2 TM, Axon instruments) and OriginPro 9.0 (OriginLab).

Immunocytochemistry

To confirm expression of target markers at the protein level, culture medium was aspirated and cells were washed with PBS briefly before being fixed in 4% paraformaldehyde for 20 min at room temperature. Cells were washed with PBS containing 0.3% Triton-100 (PBST, Sigma, T8787) three times for 5-10 min and blocked with 4% bovine serum albumin (BSA) in PBS for 30 min. Slides were incubated for 1 h at room temperature or overnight at 4°C with the primary antibody in 4% BSA in PBST (Chapter 8). Cells were washed with PBST three times for 5 to 10 min again and incubated with the appropriate secondary antibodies (Alexa Fluor® dyes secondary antibodies, Life Technologies, see Chapter 8) for 1 h at room temperature in the dark. Cells were washed again with PBST three times for 5 to 10 min and the first wash was combined with a counterstain with 4,6-Diamidino-2-phenylindole dihydrochloride (DAPI, Sigma, D9542, concentration 1:1000). Cells were mounted using mounting

media (Sigma-Aldrich, F4680) or preserved using Anti-fade reagents (ProLong® Gold 213 antifade reagent, Life Technologies, P36934) and visualised on a Zeiss fluorescence microscope.

Statistics

Statistics were performed using GraphPad Prism 6 or SPSS 24. The significance between the variables was shown based on the p-value obtained (ns indicates $p > 0.05$, * indicates $p < 0.05$, ** indicates $p < 0.005$, *** indicates $p < 0.0005$). Data are presented as bar charts (Chapter 8 only) and box/dot plots illustrating 80% of the data distribution, together with the median and 10th, 25th, 75th and 90th percentiles.

Specific methods

Chapters 3 to 8 contain further specific methods and details for modifications of methods listed above.

Chapter 3 Riboflavin Transporter Deficiency Neuronopathy

Introduction

Riboflavin transporter deficiency neuronopathy encompasses two conditions that were once considered distinct disorders: Brown-Vialetto-Van Laere syndrome (BVVLS) and Fazio-Londe disease. The Brown-Vialetto-Van Laere Syndrome (BVVLS) was first reported in 1894 by Charles Brown as an ‘infantile’ form of amyotrophic lateral sclerosis (ALS) with associated hearing loss (Brown, 1894). The male index case manifested an acute onset of bulbar weakness, hearing loss and respiratory insufficiency at age 12 years, with rapid progression of symptoms and later involvement of the upper limbs as well as ‘general arrest of development and emaciation’. The subsequent report of three siblings with pontobulbar paralysis and associated hearing loss by Vialetto in 1936 followed by the report of three sisters with similar clinical features by Van Laere in 1966, resulted in the term BVVLS being used to describe this pontobulbar palsy (Brown, 1894, Vialetto, 1936, Van Laere, 1966). Since the initial reports there have been many individual cases and small families described with BVVLS (Manole et al., 2014). Fazio-Londe disease clinical presentation is similar to BVVLS, without the hearing loss (Johnson et al., 2012).

Affected patients mostly present with neuropathy, bilateral sensorineural deafness, bulbar palsy and respiratory compromise (Figure 3-1). Other cranial nerve palsies, optic atrophy, upper and lower motor neuron involvement and ataxia can occur particularly as disease progresses, mimicking conditions such as amyotrophic lateral sclerosis (ALS), Madras motor neuron disease (MMND) and Nathalie syndrome (Anand et al., 2012, Manole et al., 2014). Deafness is the most common sign of this condition, with most affected individuals exhibiting hearing loss during the disease course. The time between the onset of deafness and the development of other manifestations varies (Manole and Houlden, 2015). Very few autopsy findings have been described but mainly show degeneration and atrophy of the cranial nerve nuclei and variable loss of anterior horn cells in the spinal cord with replacement gliosis (Johnson et al., 2012).

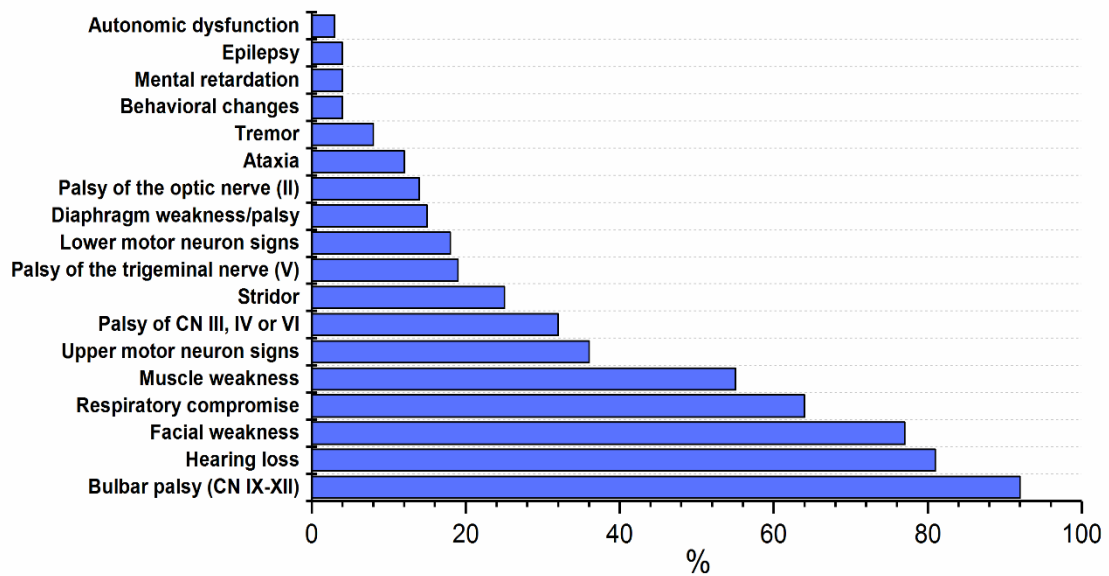


Figure 3-1 Prevalence of symptoms in the Brown-Vialetto-Van Laere syndrome.

The most prevalent symptoms are bulbar palsy, hearing loss, facial weakness, ataxia, neuropathy and respiratory compromise. Statistics have been generated from case reports dating from 1981 to 2016. CN = cranial nerve. Modified from Manole et al., 2014.

Molecular Genetic Pathogenesis

Solute carrier family 52, riboflavin transporter member 1 (*SLC52A1*) (previously G protein-coupled receptor 172B (*GPR172B*)) encodes the human riboflavin transporter 1 (RFVT1) (previously human riboflavin transporter 1 (hRFT1)) (Yao et al., 2010).

SLC52A2 (previously G protein-coupled receptor 172A (*GPR172A*)) encodes the human riboflavin transporter 2 (RFVT2) (previously human riboflavin transporter 3 (hRFT3)) (Yao et al., 2010).

SLC52A3 (previously chromosome 20 open reading frame 54 (*C20orf54*)) encodes the human riboflavin transporter 3 (RFVT3) (previously human riboflavin transporter 2 (hRFT2)) (Yamamoto et al., 2009).

Previous work has revealed strong links between mutations in *SLC52A2* and *SLC52A3*, and BVVLS (Green et al., 2010, Johnson et al., 2012, Foley et al., 2014) (Figure 3-2). The role of *SLC52A1* in BVVLS pathogenicity is still uncertain, as it was found to be defective in only one case (Ho et al., 2011). OMIM entries for BVVLS are listed in Table 3-1.

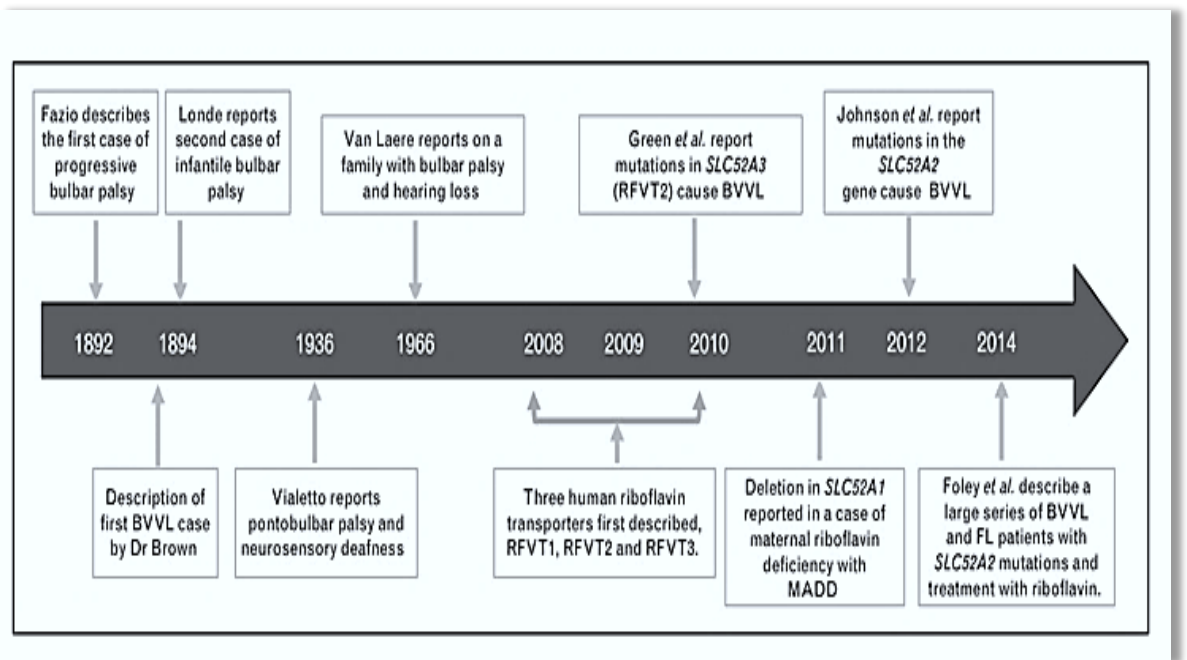


Figure 3-2 Timeline with important hallmarks over more than a century.
 The Brown–Violetto–Van Leare and Fazio–Londe progressive bulbar palsy discoveries.
 Modified from Manole et al., 2014.

Table 3-1 OMIM Entries for the Brown-Violetto-Van Laere Syndrome

211500	FAZIO-LONDE DISEASE
211530	BROWN-VIALETTO-VAN LAERE SYNDROME 1; BVVLS1
607882	SOLUTE CARRIER FAMILY 52 (RIBOFLAVIN TRANSPORTER), MEMBER 2; <i>SLC52A2</i>
613350	SOLUTE CARRIER FAMILY 52 (RIBOFLAVIN TRANSPORTER), MEMBER 3; <i>SLC52A3</i>
614707	BROWN-VIALETTO-VAN LAERE SYNDROME 2; BVVLS2

SLC52A2 and *SLC52A3* mutations include missense, nonsense, frame-shift, and splice-site alterations, but uniformly result in loss-of-function through reduced RFVT expression and/or riboflavin uptake (Foley et al., 2014, Intoh et al., 2016).

Riboflavin transporters

Three mammalian riboflavin transporters (RFVTs) have been previously characterized (Yonezawa and Inui, 2013). These are homologous proteins and primary structural analysis show that they exhibit high similarity and identity. RFVT2 shows 86.7% and 44.1% amino acid identity with RFVT1 and RFVT3, respectively. They are predicted to have 10 (RFVT1 and RFVT2) and 11 (RFVT3) membrane-spanning domains (Yonezawa and Inui, 2013).

Studies have revealed that mammalian RFVTs exhibit wide domains of expression (Yonezawa and Inui, 2013). However, RFVT2 was more strongly expressed in the brain and salivary gland while RFVT1 was strongly expressed in the placenta and small intestine and RFVT3 was most abundantly expressed in the testis and strongly in the small intestine and prostate (Yonezawa and Inui, 2013) (Figure 3-3). The apparent Michaelis–Menten constants of riboflavin calculated for RFVT1, RFVT2 and RFVT3 were 1.38, 0.33 and 0.98 μM respectively (Bosch et al., 2011). Since riboflavin cannot be synthesised by mammals *de novo*, RFVTs are thought to be indispensable for normal cellular metabolism, signifying that reduced intracellular riboflavin is a critical pathological mediator of BVVLS.

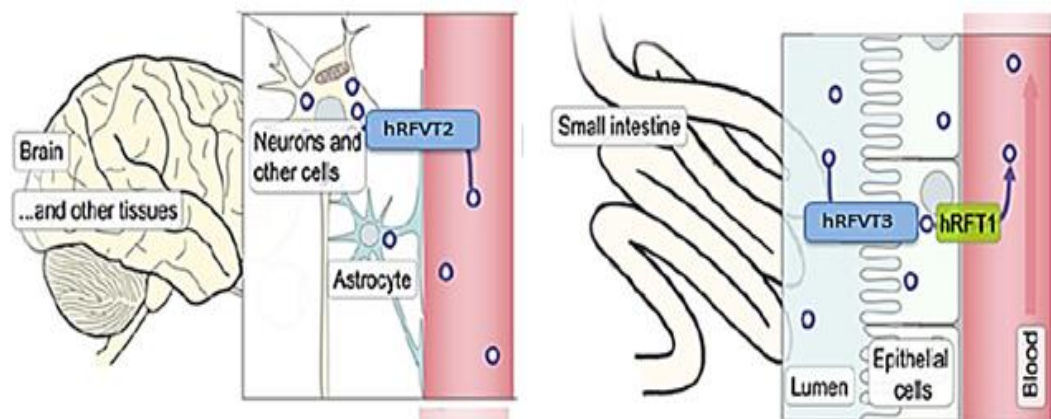


Figure 3-3 Distribution of human riboflavin transporters.

Riboflavin is taken up and passed through into the blood by intestinal epithelial cells. Uptake into the target cells may be facilitated to a small extent by passive diffusion but essentially relies on specific transport systems. RFVT2 is highly expressed in the brain, concordant with an important role in brain riboflavin homeostasis, while RFVT1 and RFVT3 are expressed mainly in the gut. Modified from (Haack et al., 2012)

Riboflavin and its derivatives

Riboflavin (7,8-dimethyl-10-ribityl-isoalloxazine), also known as vitamin B₂ (Figure 3-4), is a water-soluble compound that is essential for normal cellular functions and its main role in the body is to serve as a precursor for flavin mononucleotide (FMN) and flavin adenine dinucleotide (FAD). These coenzymes underpin many biological redox reactions. In the human genome there are over 90 genes encoding for flavin-dependent proteins, utilizing either FMN or FAD, while very few have a requirement for both (Lienhart et al., 2013). Other roles of riboflavin include drug and endobiotic metabolism via cytochrome P450 enzyme systems (Massey, 2000). Furthermore, they are required for Acyl-CoA dehydrogenases and disulphide reductases (Massey, 2000) (Figure 3-4). Abnormalities in plasma flavin levels and in acylcarnitine profile have been observed in some but not all BVVLS patients (Foley et al., 2014).

Milk and dairy products contain particularly high concentrations of riboflavin and these represent a large fraction of Western diets (Powers, 2003). Cereals, meats and fatty fish are also good sources of riboflavin. A small amount of riboflavin is present in food as the monophosphorylated form, FMN but most occurs as FAD so both have to be hydrolysed by nonspecific phosphatases in the brush border membranes of enterocytes for dietary riboflavin to be absorbed (Zanette et al., 1984). Absorption takes place primarily in the proximal small intestine (Haack et al., 2012) with an absorption half-life of 1.1 h, and urinary excretion increases linearly with intake (Zempleni et al., 1996). The first step in human flavo-cofactor biosynthesis is the phosphorylation of riboflavin to form FMN, a reaction catalysed by riboflavin kinase which introduces a phosphate group onto the terminal hydroxyl of riboflavin. A substantial portion of FMN is further transformed by FAD synthetase via the attachment of AMP to FAD (Figure 3-4).

FMN and FAD are also important components of cellular respiration as they function in the electron transport chain, thus making riboflavin critical for energy metabolism.

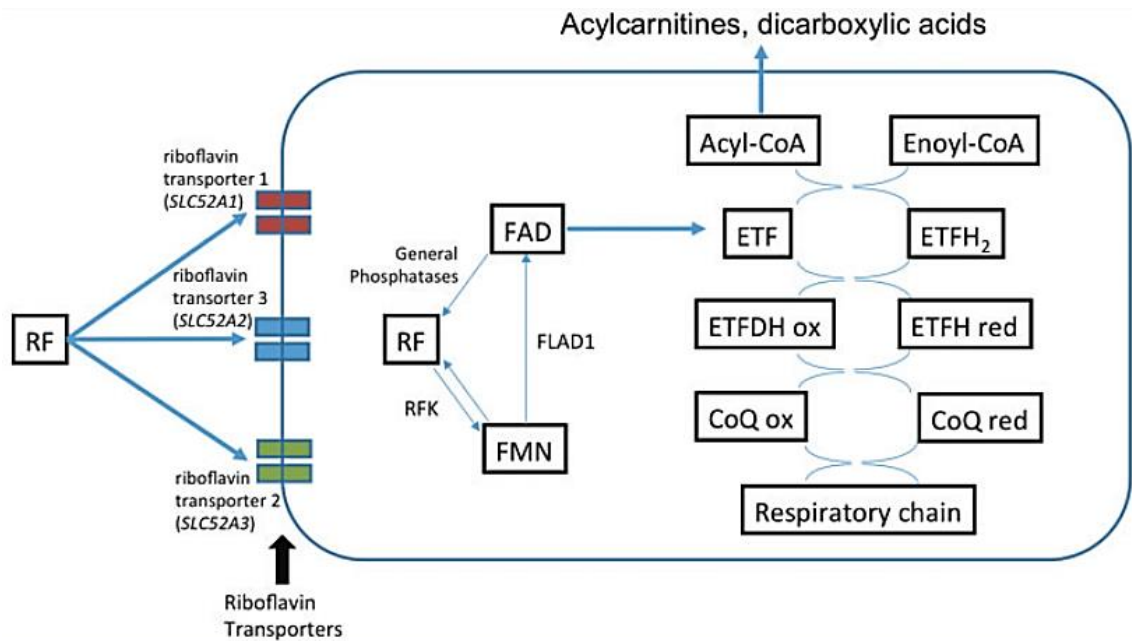


Figure 3-4 Riboflavin transport and metabolic trapping of FMN and FAD

The conversion of riboflavin into FMN and FAD forms takes place in the cytoplasm of most cells, especially in the small intestine, liver, kidney and heart. The RFK product, riboflavin kinase, catalyzes the phosphorylation of riboflavin (RF) to form FMN. The FLAD1 product is thought to catalyze the adenylation of FMN to form FAD. ETF = electron transport flavoprotein; CoQ = coenzyme Q (ubiquinone); ETFDH = electron transport flavoprotein dehydrogenase; FMN = flavin mononucleotide; FAD = flavin adenine dinucleotide; RF = riboflavin. Note the three riboflavin transporters are variably expressed in disparate tissues. Modified from (Johnson et al., 2012).

Mitochondrial electron transport chain

Mitochondrial multi-protein complexes of the electron transport chain (ETC) generate the majority of cellular energy in the form of ATP via oxidative phosphorylation. These are found in the inner mitochondrial membrane and consist of: complex I (reduced nicotinamide adenine dinucleotide (NADH): ubiquinone oxidoreductase), complex II (succinate: ubiquinone oxidoreductase), complex III (ubiquinol: ferrocyanochrome *c* oxidoreductase), complex IV (cytochrome *c* oxidase), and complex V (ATP synthase). NADH initially binds to complex I and transfers two electrons to the FMN prosthetic group of the enzyme to give FMNH₂. The electrons are then transferred to the FMN via a series of iron-sulfur (Fe-S) clusters, and finally to coenzyme Q10 (ubiquinone) to be reduced to ubiquinol (Figure 3-5). This electron flow changes the redox state of the protein, inducing conformational changes of the complex resulting in protons being pumped out of the mitochondrial matrix (Voet, 2008). In complex II electrons are delivered to ubiquinone originating from succinate and transferred via FAD (Figure 3-

5). Other electron donors (e.g., fatty acids and glycerol 3-phosphate) to the complex also direct electrons to ubiquinone via FAD. Complex II is a parallel electron transport pathway to complex I, but no protons are transported to the intermembrane space (Voet, 2008). Complex III transfers electrons to cytochrome *c*, a water-soluble electron carrier located within the intermembrane space. A proton gradient is formed and in total four protons are translocated (Voet, 2008). Complex IV transfers electrons from cytochrome *c* and to O₂, producing H₂O. At the same time protons are translocated across the membrane, contributing to the proton gradient (Voet, 2008). In complex V, the proton gradient formed before is used to make ATP via oxidative phosphorylation (Voet, 2008). We hypothesize that lower levels of riboflavin in the cell as a result of mutated transporters would lead to reduced levels of FMN and FAD, which in turn would lead to impairments at the level of the ETC. It is important to note that high dose riboflavin supplementation in BVVLS patients, and especially in young patients, has been shown to improve their biochemical and clinical condition (Bosch et al., 2011, Foley et al., 2014).

Defects in ETC produce free radicals which induce membrane lipid peroxidation and DNA damage (Turrens, 2003). Such impairments could lead to bioenergetic dysfunctions that may ultimately cause neuronal cell death thus implicating mitochondria in the pathology of neurodegenerative disorders (Lezi and Swerdlow, 2012, Udhayabanu et al., 2017).

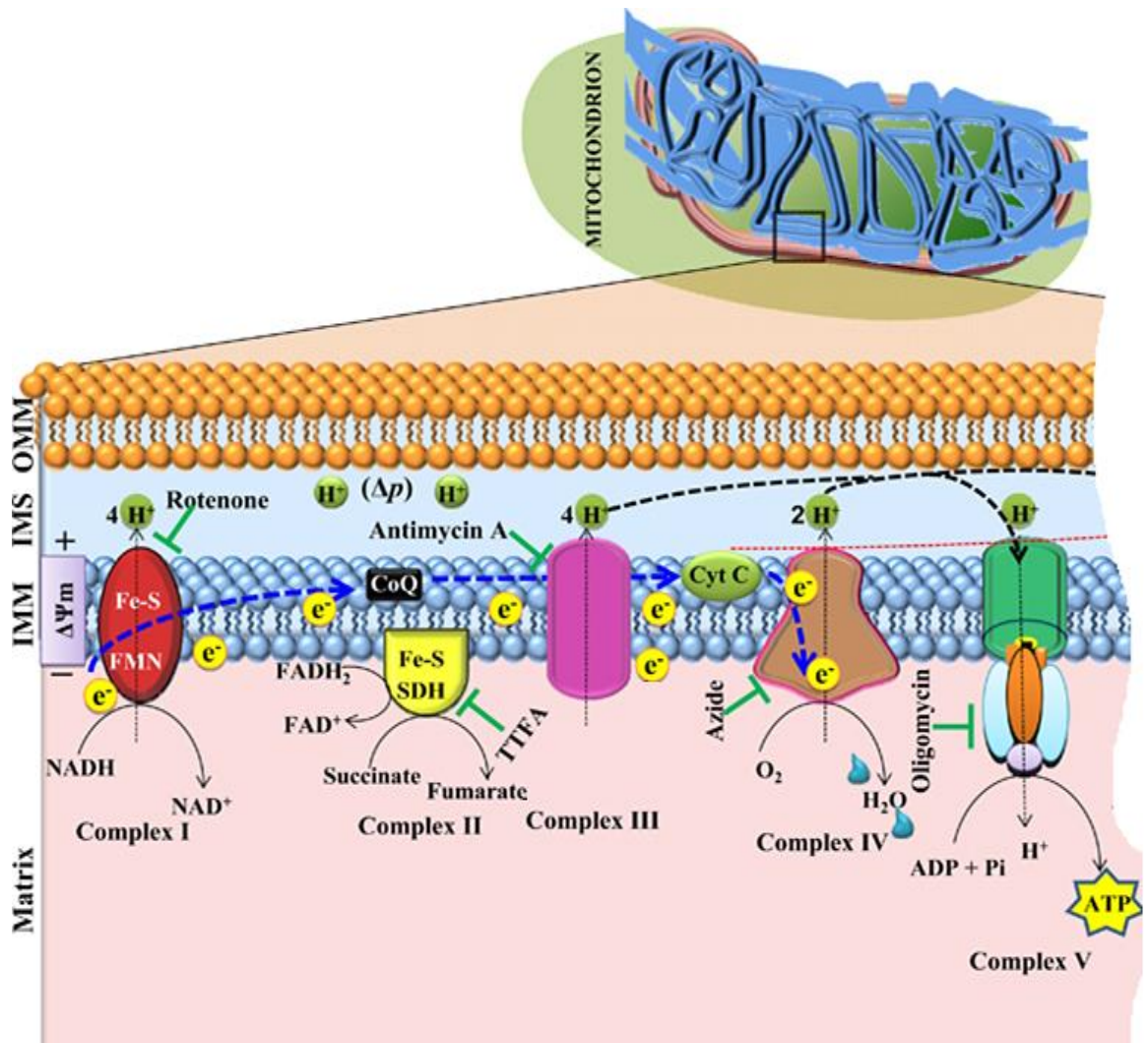


Figure 3-5 Diagram of mitochondrial electron transport chain complexes

During respiration, the free energy generated by oxidation of substrates is conserved in reduced molecules of nicotinamide adenine dinucleotide (NADH) and FADH₂. These donate the electrons to protein complexes and the energy in these molecules is used to transport protons to the intermembrane space. The electrons from the complexes I and II are accepted by mobile electron carrier coenzyme Q (CoQ), which then acts as an electron donor to the complex III. Cytochrome *c* shuttle these electron between complexes III and IV. Complex IV then reduces molecular oxygen to water. Complex V drives synthesis of adenosine triphosphate (ATP) from adenosine diphosphate (ADP) and inorganic phosphate (Pi), and as a result, the protons are transported back to the matrix through complex V. Rotenone, TTFA, antimycin A, azide and oligomycin are inhibitors of complex I, II, III, IV and V respectively. Cyt *C*: cytochrome *c*; IMM: inner mitochondrial membrane; IMS: intermembrane space; OMM: outer mitochondrial membrane; TTFA: thenoyl trifluoroacetone. Modified from (Mehta and Li, 2009).

Mitochondria in neurodegeneration

Mitochondria are known to play a key role in many cellular functions including ATP generation, intracellular Ca^{2+} homeostasis, reactive oxygen species (ROS) formation, and apoptosis (Lezi and Swerdlow, 2012). Mitochondrial dysfunction is a common signature in development of neurodegenerative diseases such as Alzheimer's, Parkinson's, Huntington's and ALS, where decreases in one or more mitochondrial complexes and corresponding oxidative stress have been reported in cell or animal models (McInnes, 2013, Golpich et al., 2016, Menzies et al., 2002, Fukui and Moraes, 2007, Hoglinger et al., 2003, Yamada et al., 2014). Neurons are dependent on mitochondria because of their high energy demands. In particular motor neurons are thought to be uniquely especially to impaired energy metabolism because of their high metabolic rate and axonal length (Cozzolino and Carri, 2012). It is also important to note that primary mitochondrial disorders that affect mitochondrial DNA (mtDNA) such as MELAS (mitochondrial encephalomyopathy, lactic acidosis, and stroke-like episodes) and MERRF (myoclonic epilepsy with ragged red fibers) tend to affect the central nervous system and muscle, the body's two most aerobic tissues (Scaglia and Northrop, 2006).

Animal models of riboflavin transporter deficiency

Previous work has utilised knock-out of the mouse *SLC52A3* orthologue to model BVVLS (Yoshimatsu et al., 2016, Intoh et al., 2016), but the *SLC52A3* homozygous knock-out mice die within 48 h of birth (Yoshimatsu et al., 2016), precluding phenotypic analysis at later developmental stages. In order to generate a new *in vivo* model of BVVLS, we turned to the fruit fly, *Drosophila melanogaster*. Comparative BLAST analysis revealed a single *Drosophila* homologue of *SLC52A3*, the previously uncharacterised gene *cg11576* (E-value: $2.74e^{-74}$; next closest homologue, E-value: 2.95). As described below, we named the *cg11576* gene *drift* (*Drosophila* riboflavin transporter). The DRIFT amino-acid sequence exhibits 36.9% identity and 53.1% similarity with hRFVT3, and the L1 loop and GXXXG motifs characteristic of RFVTs are also conserved (Figure 3-6). The L1 loop is a region of the protein shown to recognize riboflavin through both hydrogen bonds and van der Waals interactions (Zhang et al., 2010), while the GXXXG motif is required for dimerization (Russ and Engelman, 2000). DRIFT is also highly homologous to the hRFVT3 paralogues

hRFVT1 and hRFVT2 (Figure 3-6). DRIFT exhibits a broad expression pattern according to RNAseq data from the *Drosophila* ModEncode Project (Graveley et al., 2011).

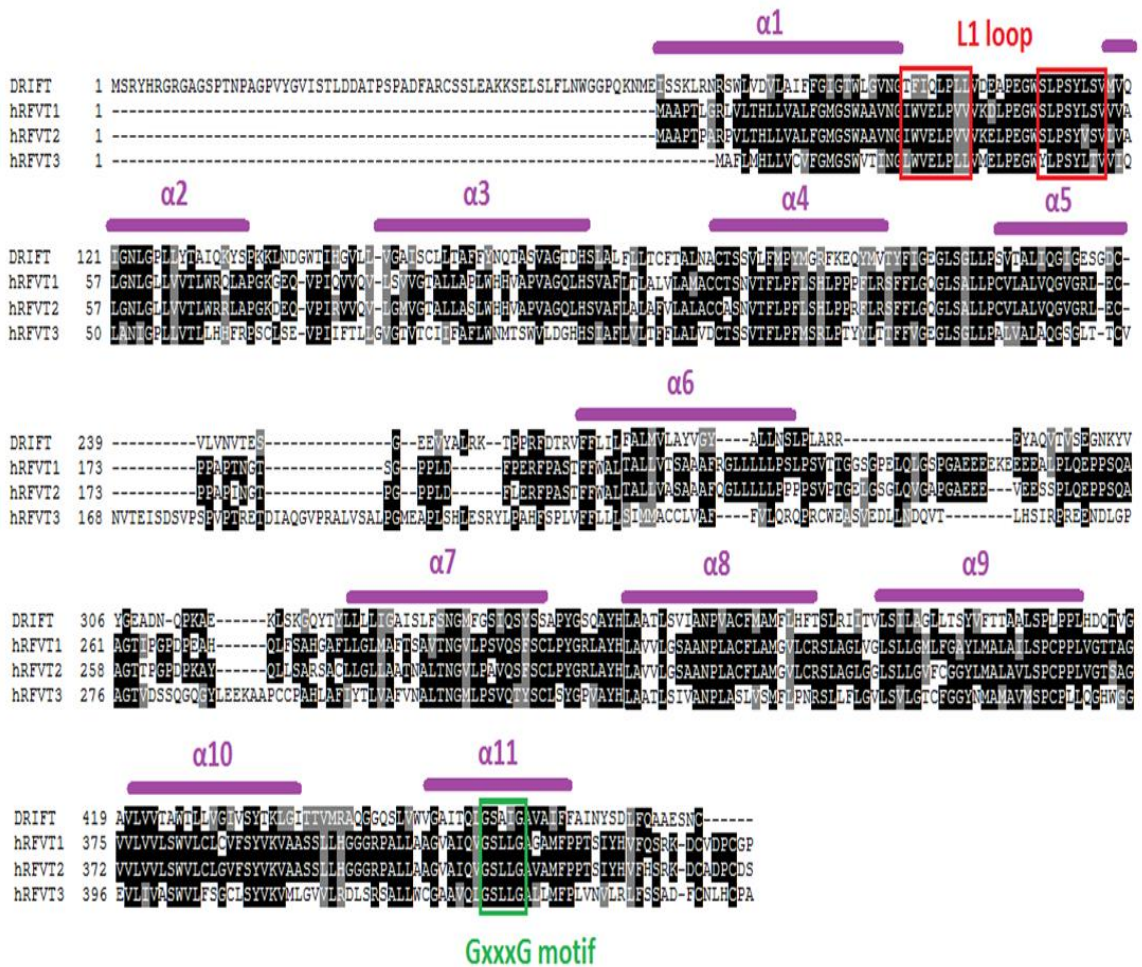


Figure 3-6 Conservation of residues amongst DRIFT, RFVT1, RFVT2 and RFVT3. Single letters: amino acids. Black: identical amino acid, Grey: semi-conserved substitution (similar shapes). Purple bars indicate the transmembrane α -helices predicted with TMHMM (<http://www.cbs.dtu.dk/services/TMHMM-2.0/>). The L1 loop, highlighted in red, is a conserved region that has been shown to interact with riboflavin in a crystalized soluble portion of a riboflavin transporter in *Streptococcus aureus* (3P5N). The GxxxG motif highlighted in green is a well conserved motif for dimerization. Conservation among species of the amino acid residues was determined using ClustalW2 software for multiple sequence alignment and plotted with BOXSHADE.

A disruption of DRIFT in *Drosophila* would therefore provide a model for BVVLS. Transgenic RNA interference (RNAi), transposon-mediated mutagenesis, and homologous recombination-based gene knockout can be used for this purpose (Greene et al., 2003). In this study we have used the GAL4-UAS system which consists of two parts: GAL4, a yeast

transcription activator protein under control of a *Drosophila* promoter, and the GAL4-binding sequence UAS (upstream activating sequence) 5' of DNA encoding, for example, an effector transgene or an inverted RNA repeat to generate dsRNA (Brand and Perrimon, 1993).

Aims of this chapter

In this study, we expand the clinic-genetic spectrum of riboflavin transporter genes and then perform a series of experiments to identify the underlying effects of loss of RFVT function on neuronal integrity and mitochondrial function. We review clinical case histories and undertake pathological evaluation of brain and spinal cord of two patients with confirmed *SLC52A3* mutations who presented either in infancy or in later childhood. Finally, we investigate the *in vitro* cellular effects of *SLC52A2* mutations on metabolism and ETC function and also the *in vivo* consequences of loss of the *SLC52A3* homologue in *Drosophila*, and test whether these can be mitigated by supplementation with a riboflavin derivative.

Methods

Study Subjects

Patients were enrolled with informed consent from the patient and/or their parental guardian. DNA was collected from a total of 132 suspected cases (probands and their relatives) presenting with cranial neuropathies and sensorimotor neuropathy with or without respiratory insufficiency. Patients' DNA samples were collected at medical centres in England (including from patients originating from Pakistan, India, Saudi Arabia, Kuwait, Iran and Turkey) as well as from medical centres in Wales, Scotland, Northern Ireland, Ireland, France, Belgium, the Netherlands, Greece, Malta, Russia, Lebanon, Iceland, Australia and the United States, following the announcement of an on-going molecular study at the UCL Institute of Neurology, University College London (National Hospital for Neurology & Neurosurgery, Queen Square, London) of patients presenting with this phenotype. This study was ethically approved by the UCL/University College London Hospital Joint Research Office (99/N103), and written informed consent to perform a skin biopsy and fibroblasts was obtained as appropriate. Clinical assessment of the patients was performed by consultants.

PCR and Sanger sequencing

Primer sequences, PCR and Sanger sequencing conditions for *SLC52A1*, *SLC52A2* and *SLC52A3* were described by (Foley et al., 2014) (Chapter 2). Segregation of pathogenic variants was also assessed. Where one heterozygous mutation was identified, deletions in the other allele were investigated by array CGH but no deletions or insertions were identified. Mutation positions are based on NCBI reference sequences for complementary DNA. *SLC52A2* mutation positions are based on sequences NM_024531.4 for the nucleotide sequence and NP_078807.1 for the protein sequence. *SLC52A3* mutation positions are based on sequences NM_033409.3 for the nucleotide sequence and NP_212134.3 for the protein sequence.

Neuropathological evaluation

Formalin-fixed, paraffin embedded brain and spinal cord tissue were available from two patients (AM2 and AM4). The paraffin sections were cut at 4 µm, mounted on glass slides and stained with routine H&E and Luxol fast blue/cresyl violet histochemical stains. Sections were examined by immunohistochemistry with the following antibodies: glial fibrillary acid protein (GFAP) (polyclonal, 1:2500, Dako), phosphorylated neurofilaments (clone SMI31, 1:5000, Sternberg), myelin basic protein (clone SMI94,

1:2000, Sternberg), ubiquitin (polyclonal, 1:1200, Dako), p62 (3/P62LCK Ligand, 1:100, BD Transduction), α -synuclein (clone KM51, 1:50, Leica/Novocastra), amyloid- β (clone 6F3D, 1:100, Dako), hyperphosphorylated tau (clone AT8, 1:1200, INNOGENETICS), TDP43 (clone 2E2-D3, 1:3000, Abova), CD68 (clone PG-M1, 1:100, Dako), CD3 (LN10, 1:100, Leica/Novocastra), CD20 (clone 7D1, 1:200, Dako). Immunohistochemistry was carried out either manually or on a BondMax autostainer (Leica Microsystems) using 3,3-diaminobenzidine as chromogen. Negative controls were treated identically except that the primary antibody was omitted. Appropriate positive controls were used for all immunohistochemical studies. Staining and analysis was performed by Zane Jaunmuktane.

Generation of human fibroblast cultures and cell culture

Skin fibroblasts of BVVLS patients with *SLC52A2* mutations were generated at the Medical Research Council (MRC) Centre for Neuromuscular Diseases Biobank, Dubowitz Centre, UCL Institute of Child Health (ICH) by Dr Diana Johnson, or sent in culture by collaborators. Three age-matched controls were obtained from the ICH Biobank: Control 1 (C1) (age at biopsy: 14 years; female); Control 2 (C2) (age at biopsy: nine years; male); Control 3 (C3) (age at biopsy: five years; male). Five BVVLS patients' fibroblast lines were available for this study. Patients carried the following mutations:

p.[Gly306Arg];[Gly306Arg];p.[Trp31Ser];[Leu312Pro];p.[Gln234Stop];[Ala420Thr]; p.[Gly306Arg];[Leu339Pro]; p.[Tyr305Cys]; [Gly306Arg]. All cells were maintained at 37°C and 5% CO₂ under humidified conditions and cultured in high glucose Dulbecco's modified Eagle medium (Invitrogen) supplemented with 10% foetal bovine serum (Biowest). All fibroblast lines were grown for four days in modified DMEM containing physiological concentrations (12.6 nM) of riboflavin, followed by four days in modified DMEM, which was either riboflavin-supplemented (300.6 nM) or contained a low riboflavin concentration (3.1 nM). Cell culture was performed by Amelie Pandraud.

Determination of flavin status in fibroblasts

Riboflavin, FMN and FAD content were measured in neutralized perchloric extracts by means of High Performance Liquid Chromatography (HPLC), as previously described (Giancaspero et al., 2009). Quantitative determination of riboflavin, FMN, and FAD was carried out using the Whole Blood Chromsystems vitamins B₁/B₂ kit (Chromsystems, Germany) as per the manufacturer's protocol. The Bio-Rad DC protein assay (Bio-Rad

Laboratories, USA) was used to normalise for protein concentration. Amelie Pandraud performed these experiments.

Assessment of ETC complex I, II, and citrate synthase activities in fibroblasts

All enzyme activities were determined at 30°C. Prior to analysis all samples were subjected to three cycles of freeze/thawing to lyse membranes. Enzymatic activities were determined using an Uvikon 940 spectrophotometer (Kontron Instruments Ltd, Watford, UK).

Complex I activity was measured according to the method of (Ragan, 1987), which involved monitoring the oxidation of NADH at 340 nm. Complex II assay was measured according to the method of (Birch-Machin et al., 1994), which monitored the succinate-dependent 2-thienyltrifluoroacetone sensitive reduction of 2,6-dichlorophenolindophenol at 600 nm. The activity of citrate synthase was measured by the formation of the anion of thionitrobenzoate from 5,5'-dithiobis(2-nitrobenzoate) and CoA at 412 nm (Shephard, 1969). This provided an estimate of mitochondrial content and was therefore used to normalise complex I and II activities for mitochondrial enrichment (Hargreaves et al., 1999). Amelie Pandraud performed these experiments.

***Drosophila* stocks and culture conditions**

Fly strains were obtained from the Bloomington *Drosophila* Stock Center (Indiana, USA) and Vienna *Drosophila* Resource Center (Austria). All transgenic insertions used in this study were outcrossed at least 5 times into an isogenic (iso31) background. These were: *cg11576* UAS-RNAi ((VDRC 7578) (Dietzl et al., 2007) and HMC04813 (Perkins et al., 2015)), and *daughterless*-GAL4 (Bloomington stock 55850). Flies were reared at 25°C on standard fly food consisting of corn meal, yeast, sucrose, glucose, wheat germ, soya flour, nipagin and propionic acid. For experiments with compound supplementation, 0.1 mg/ml riboflavin (Sigma) or 0.1 mg/ml riboflavin-5'-lauric acid monoester (RLAM) was added to the food. Flies were kept under 12 h light: 12 h dark cycles, defined as LD conditions.

Semi-quantitative RT-PCR for whole flies

Total RNA was extracted from flies using TRIzol, as per manufacturer's instructions. The concentration and purity of RNA was determined spectrophotometrically. 1 µg of RNA was reverse transcribed to first strand cDNA by using random primers and Moloney murine leukemia virus reverse transcriptase (Promega, Madison, WI, USA). Primers used for *cg11576* (*drift*) were designed so that they span exon-exon boundaries, Forward– 5' CCAGATGCTCCTCTCTCGA 3' Reverse– 5' AGTACACAGTCGCCACTCTC 3'.

Primers used for *Drosophila rp49* were: Forward– 5' CCCAACCTGCTTCAAGATGAC 3', Reverse – 5' CCGTTGGGGTTGGTGAGG 3'. GoTaq® Green Master Mix was used and PCR reactions were performed with the following protocol: 95°C-2 min, (95°C-30 s, 60°C-30 s, 73°C-1 min) for 35 cycles, 73°C-5 min, and 4°C-hold. Two exponential curves representing the product formation was made for both primer pairs and cycles 26 and 29 were chosen for *rp49* gene and *drift* respectively so that amplification rates were in the linear range for semi-quantitative comparisons.

Quantification of flavins, ETC complexes I, II, II/III redox activities and citrate synthase assay in *Drosophila*

Riboflavin, FMN and FAD content, and the redox activities of ETC complexes I and II redox activity and citrate synthase activities were measured in flies (approximately 10/genotype) as described above for patient fibroblasts and in more detail in Chapter 2. Prior to analysis all samples were subjected to three cycles of freeze/thawing to lyse membranes. A Lowry assay was used to normalize for protein concentration (Frolund et al., 1995). Complex II/III activity was determined at 30°C using the method of (King, 1967) which followed the succinate-dependent antimycin A sensitive reduction of cytochrome *c* at 550 nm (see Chapter 2).

Larval behaviour

Larval locomotion was tested by placing individual third instar larvae in the center of petri dishes (8.5 cm diameter, 1.4 cm height) coated with 10 ml of 4% agar. On average, 30 larvae were tested per strain. The number of grid squares (1 cm) entered per min by the larva was analysed using Kruskal-Wallis tests and subsequently Dunn's post-hoc tests.

Adult behaviour

Adult flies were kept as groups of males and females in a 12h:12h light-dark (LD) cycle at 25°C for 1 day prior to testing. Single virgin females (approx. 1 day old) were loaded into glass tubes (with 2% agar and 4% sucrose food) and monitored using the *Drosophila* Activity Monitoring System (Trikinetics) in LD at 25°C with an approximate intensity of 700-1000 Lux during the L condition. For experiments involving RLAM-supplementation, RLAM was added to the above food. Fly activities were deduced from the number of times flies broke beams of infrared light passing through the middle of the tube (Chapter 2). Locomotor activity was recorded in 30 min bins and an analysis was performed on the second day after loading. Data were pooled from at least two independent experiments. The relative locomotor activities per 30 min bin for individual flies were averaged for each

genotype and also the average locomotor activity per day was calculated. Locomotion graphs were generated using GraphPad Prism 6 and Microsoft Excel.

Life span

Adult female flies were collected from eclosion and transferred to fresh food tubes (10 flies/tube) with or without riboflavin or RLAM supplementation. Each day, death events were scored and viable flies were transferred to fresh tubes. Survival proportions were plotted as percentage of live flies against days. Approximately 100 flies were tested for each genotype.

Other statistics

Statistics were performed using GraphPad Prism 6. The significance between the variables was shown based on the p-value obtained (ns indicates $p > 0.05$, * indicates $p < 0.05$, ** indicates $p < 0.005$, *** indicates $p < 0.0005$). Data are presented as box plots illustrating 80% of the data distribution, together with the median and 10th, 25th, 75th and 90th percentiles.

Results

Clinical and genetic analysis of BVVLS patients

We screened 132 patients with phenotypes suggestive of BVVLS and identified twenty patients (15%) with RFVT mutations. Genetic and clinical details of the twenty individuals carrying mutations in *SLC52A2* or *SLC52A3* are summarised in Table 3-2 and 3-3. Thirteen of the probands were males. Age of symptom onset was available for 15 patients (mean: 8.2 years; range: 7 months – 21 years). First symptoms usually occurred during childhood (11 patients) and less frequently during teenage years (four patients) or adulthood (one patient), and were mostly secondary to cranial nerve involvement (Table 1). Only one patient presented with symptoms not related to cranial nerve involvement (limb weakness). Sensorineural hearing loss was both a common presenting symptom (eight patients) and a common clinical feature during follow-up (17 patients). Other frequent clinical features include optic atrophy (14 patients), weakness of facial and bulbar muscles (13 patients) and sensorimotor peripheral axonal neuropathy (16 patients). Limb weakness was more severe in the upper than in the lower limbs in nine patients. Ten patients developed some degree of respiratory involvement with three requiring assisted ventilation, and ten patients had dysphagia and/or chewing difficulty, six of them requiring nasogastric tube or gastrostomy feeding.

Of the twenty-two mutations identified, eight were found in the *SLC52A2* locus and 14 in *SLC52A3*, of which five *SLC52A2* and nine *SLC52A3* variants were novel (Table 3-2 and 3-3). In contrast, no *SLC52A1* mutations were observed. None of the variants were found in the homozygous state in the ExAC database of over 100,000 controls, suggesting pathogenicity (Table 3-2). Consistent with this hypothesis, all except one mutation (p.Arg212Cys in *SLC52A3*) were predicted to be at least probably damaging by SIFT and Polyphen-2 algorithms (scores ranging between 0.55 and 1). The mutations reside in transmembrane helices and in the intracellular and extracellular loops. Although three homozygous and seven compound heterozygous mutations were identified, five mutations (all in *SLC52A3*) were identified on only one allele. These heterozygous individuals did not differ substantially in phenotype including age of presentation from the rest of the cohort of mutation-positive cases. There was no correlation between the nature of pathogenic variant and phenotype severity, although in the case of patient AM2 nonsense mutations on both alleles resulted in a truncated protein, and this genotype correlated with rapid progression of symptoms and death at 2 years of age.

Table 3-2 Clinical and genetic features of BVVLS patients (AP1-10).

The features were reported at the time of diagnosis. Novel mutations are in bold.

Patient	Mutation	Sex	First Symptom	Age at first symptom	OA/HL	Sensorimotor neuropathy**	Distribution of weakness	Overall maximal motor function	Maximal motor function at the time of diagnosis	Respiratory function	Feeding	Age at genetic diagnosis
AP1	<i>SLC52A2</i> homozygous c.935T>C p.Leu312Pro	F	horizontal nystagmus	7 months	OA	yes	UL>LL	crawling, could hold objects with pincer grip	hypotonic, deteriorated arm function	ventilator dependent	gastrostomy only	deceased (2.1 yrs)
AP2	<i>SLC52A2</i> compound heterozygous c.[383C>T];[1088C>T] p.[Ser128Leu][Pro363Leu]	F	sensorineural hearing loss	childhood	OA, HL	yes	UL>LL	can walk with walking devices and orthosis	able to walk	respiratory insufficiency	not affected	27 yrs
AP3	<i>SLC52A3</i> heterozygous c.1371C>G p.Phe457Leu	M	upper limb weakness	19 yrs	HL	yes	UL and LL	wheelchair bound	wheelchair bound	ventilator dependent	dysphagia	20 yrs
AP4	<i>SLC52A3</i> heterozygous c.37G>A p.Gly13Arg	M	sensorineural hearing loss	n/a	HL	yes	UL>LL	n/a	n/a	not affected	n/a	35 yrs
AP5		M	sensorineural hearing loss	n/a	HL	yes	UL>LL	n/a	n/a	not affected	n/a	35 yrs
AP6	<i>SLC52A2</i> compound heterozygous c.[1016T>C];[c.935T>C] p.[Leu339Pro][Leu312Pro]	M	visual loss, optic atrophy	15 months	OA, HL	yes	UL>LL	wheelchair bound	holds pen in mouth to draw in tablet	sleep apnea	oral diet	17 yrs
AP7	<i>SLC52A3</i> heterozygous c.374C>A p. Thr125Asn	F	sensorineural hearing loss	10 yrs	HL	yes	UL>LL	n/a	n/a	respiratory problems	n/a	12 yrs
AP8	<i>SLC52A3</i> heterozygous c.403A>G p. Thr135Ala	F	partial right third nerve palsy	15 yrs	no	yes	UL>LL	wheelchair bound	wheelchair bound	not affected	nasogastric tube	15 yrs
AP9	<i>SLC52A3</i> heterozygous c.58A>C p. Ile20Leu	M	optic nerve atrophy	2 yrs	OA, HL	yes	UL>LL	unsteadiness, fatigue and falls	n/a	respiratory problems	difficulty chewing and swallowing	25 yrs
AP10	<i>SLC52A3</i> compound heterozygous c.[106G>A];[c.1237T>C] p.[Glu36Lys];[p.Val413Ala]*	M	n/a	n/a	OA, HL	yes	n/a	could walk a short distance with a stick	n/a	not affected	n/a	n/a

* in *cis* configuration;** based on NCS; F= female; M=male; UL = upper limb; LL = lower limb; OA= Optic atrophy; HL= Hearing loss

Table 3-3 Clinical and genetic features of BVVLS patients (AM1-10).

The features were reported at the time of diagnosis. Novel mutations are in bold.

Patient	Mutation	Sex	First Symptom	Age at first symptom	OA/HL	Sensorimotor neuropathy **	Distribution of weakness	Overall maximal motor function	Maximal motor function at the time of diagnosis	Respiratory function	Feeding	Age at genetic diagnosis
AM1	<i>SLC52A3</i> compound heterozygous c.[354G>A][1074G>A] p.[Val118Met][splice defect]	M	sensorineural hearing loss	2 yrs	OA, HL	yes	UL and LL	n/a	n/a	breathing difficulty	gastronomy only	22 yrs
AM2	<i>SLC52A3</i> compound heterozygous c.[1128-1129_insT][1294G>A] p.[Tyr376fs][Trp431X]	M	horizontal nystagmus, ptosis, neck weakness	8 months	OA, n/a	yes	UL>LL	completely paralysed	completely paralysed	ventilator dependent	gastronomy only	2 yrs (deceased)
AM3	<i>SLC52A2</i> compound heterozygous c.[231G>A];[c.865C>T] p.[Glu77Lys];[Ala288V]	F	sensorineural hearing loss	3 yrs	OA, HL	yes	UL and LL	unsteadiness, fatigue and falls	unsteadiness, fatigue and falls	breathing difficulty	difficulty chewing and swallowing	54 yrs
AM4	<i>SLC52A3</i> compound heterozygous c.[39G>A];[1255G>A] p.[Gly13Arg][Gly418Asp]	M	sensorineural hearing loss	8 yrs	OA, HL	yes	LL	mild postural tremor	mild postural tremor	compromised	chewing difficult	19 yrs (deceased)
AM5	<i>SLC52A2</i> homozygous c.1327T>C p.Cys443Arg	M	nystagmus	2.5 yrs	OA, HL	yes	LL>UL	wheel chair bound	crawls in bed using elbows	not affected	nasogastric tube	8 yrs
AM6		F	visual loss, optic atrophy	18 months	OA, HL	yes	UL and LL	generalized hypotonia	n/a	not checked	nasogastric tube	4 yrs
AM7	<i>SLC52A3</i> homozygous c.634C>T p.Arg212Cys	M	facial palsy and mild hearing lost	14 yrs	OA, HL	no	no	some leg pain but can walk	some leg pain but can walk	not affected	normal	17 yrs
AM8		M	facial palsy and paralysed vocal cord	11 yrs	OA, HL	no	no	some leg pain but can walk	some leg pain but can walk	not affected	normal	15 yrs
AM9		M	no symptom	not developed	no	no	no	not checked	not checked	not affected	normal	12 yrs
AM10		F	facial palsy and mild hearing loss	14 yrs	OA, HL	no	no	some leg pain but can walk	some leg pain but can walk	not affected	normal	5 yrs

* in cis configuration;** based on NCS; F= female; M=male; UL = upper limb; LL = lower limb; OA= Optic atrophy; HL= Hearing loss

Neuropathological analysis of BVVLS patients

To characterise in detail the neuropathological symptoms of BVVLS, we undertook a comprehensive pathological examination of two patients carrying compound heterozygous *SLC52A3* mutations (AM2 and AM4; Table 3-3). These patients represent two ends of the spectrum of severity of BVVLS.

Patient AM2 had a normal birth at term. His motor skills were mildly delayed and he never acquired the ability to roll over completely front to back. He achieved the ability to sit with minimal support at age 7 months. From about 8 months of age he began to exhibit more clear signs of the condition such as ptosis and neck weakness. He was admitted at the age of 9 months for investigations but no diagnosis was made at that time. His condition quickly progressed to include respiratory muscle weakness and ventilator dependence at the age of 1 year. He also developed severe weakness in his shoulder girdle areas and proximal upper limbs. Weakness subsequently developed in forearm muscles, distal lower limb muscles and thighs, trunk and face, and progressed to the point that he could only weakly move his eyelids and had very limited sideways movements of his eyes. Nerve conduction studies (NCV) and electromyography showed a severe neuropathy. He died at two years of age of respiratory failure. The pathology was performed by Zane Jaunmuktane. Briefly, the neuronal density in the substantia nigra was normal for the patient's age, but the 3rd and 4th cranial nerve nuclei showed severe neuronal loss, gliosis and microglial activation (Appendix I). In the pons there were two symmetrical sharply demarcated lesions surrounding both 5th cranial nerves with prominent neovascularisation, dense infiltration of macrophages and widespread myelin loss, with relative preservation of axons (Appendix II). The medial lemniscus, spinocerebellar tract and medullary reticular formation were all gliotic. Inferior olivary nuclei, in particular the dorsal and ventral parts, showed severe neuronal loss and gliosis. In the cerebellum, there was no significant cortical atrophy (Appendix III), but the cerebellar white matter showed widespread vacuolation. In the spinal cord, there was moderate neuronal loss in the anterior horns and moderately severe atrophy of spinothalamic tracts, spinocerebellar tracts, gracile fasciculus and nucleus in the medulla, and to a lesser extent cuneate fasciculus and nucleus in the medulla (Appendix I). There was severe fibre loss and macrophage activation in the anterior spinal nerve roots, whilst the poster spinal nerve roots were densely populated by myelinated fibres with little macrophage activation (Appendix II).

Patient AM4 also had a normal birth at term. He had hearing problems from the age of 8 years and was diagnosed with sensorineural hearing loss at the age of 11. He developed optic atrophy and difficulty walking at the age of 16 years. At age 17 years he presented with dysarthria and subsequently developed swallowing difficulties. Electromyography showed widespread denervation and NCS studies were consistent with an axonal motor-neuropathy. He died at 19 years of respiratory insufficiency. The pathology was performed by Zane Jaunmuktane. Briefly, the 4th cranial nerve nuclei showed a mild degree of neuronal loss and accompanying mild gliosis (Appendix IV). In the pons there was prominent neuronal loss in the loci coerulei with free pigment deposits in the neuropil and gliosis (Appendix IV). The 5th and 7th cranial nerve nuclei showed severe neuronal loss (Appendices IV and V). The nerve tracts of the available 5th, 10th and 12th cranial nerves (Appendix V) showed reduced density of the myelinated fibres. The gracile nucleus showed severe, while the cuneate nucleus showed mild neuronal loss and gliosis (Appendix IV). In the cerebellar cortex there was widespread Purkinje cell loss and Bergmann gliosis and some degree of neuronal loss in the granular cell layer (Appendices III and V). In the ventral aspect of the upper spinal cord at the junction with the lower medulla there were bilateral symmetric lesions involving the anterior horns, lateral reticular nucleus, supraspinal nucleus, spinothalamic tracts and medial longitudinal fasciculus with neovascularization and dense infiltration of macrophages with a near complete loss of myelin, whilst neurons and axons were relatively preserved (Appendix VI). Severe symmetrical atrophy with prominent pallor, macrophage infiltration and vacuolation of the anterior and posterior spinocerebellar tracts (Appendix V), spinothalamic tracts and gracile and to a lesser extent cuneate fasciculi (Appendix IV) was also observed. Whilst the posterior nerve roots were densely populated by myelinated fibres with only mild macrophage activation, in the anterior nerve roots there was moderately severe loss of myelinated fibres and prominent infiltration of macrophages (Appendix VI).

Fibroblasts biochemical studies

Mitochondrial dysfunction has long been documented in neurodegenerative diseases (Palomo and Manfredi, 2015). For example, SOD1 mutations in familial ALS have been shown to lead to abnormalities in mitochondrial morphology, both in biopsies and post-mortem tissues of human patients (Sasaki and Iwata, 2007, Sasaki, 2010) and in cellular and mouse models of the disease (Magrane et al., 2009, Vinsant et al., 2013, Magrane et al., 2014, Palomo and Manfredi, 2015). However, whether mitochondrial function is perturbed

by BVVLS-linked mutations has yet to be examined. We hypothesized that lower levels of intracellular riboflavin as a result of mutated RFVTs would lead to reduced levels of FMN and FAD, which in turn would lead to impairments at the level of the ETC complex I and complex II. Using fibroblasts derived from BVVLS patients with RFVT mutations and healthy age-matched controls, we found a significant reduction in the intracellular levels of FMN and FAD in patient fibroblasts when grown in low extracellular riboflavin conditions (Figure 3-7). Levels of intracellular riboflavin in patient fibroblasts frequently fell below the threshold of detection under these conditions (but not in control fibroblasts; data not shown), consistent with defective riboflavin transport. Furthermore, we observed a significant reduction in ETC complex I and complex II activity in patient fibroblasts compared to controls (Figure 3-7). These experiments were performed by Amelie Pandraud.

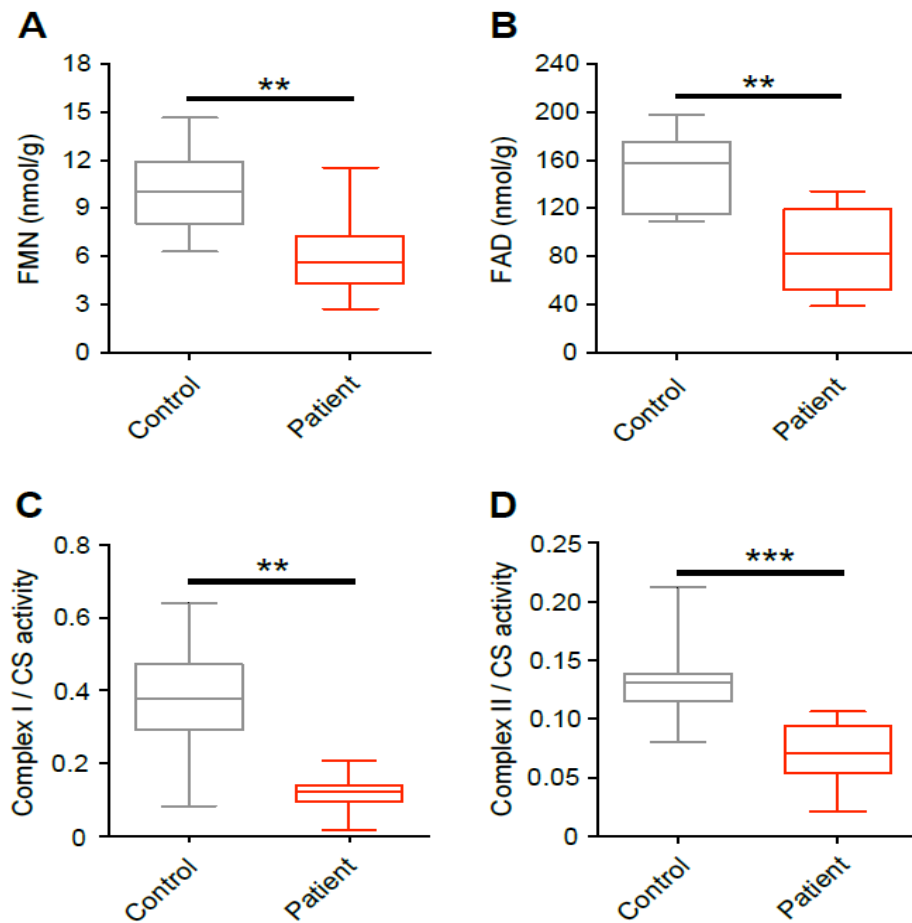


Figure 3-7 Reduced mitochondrial activity in BVVLS patient fibroblasts. (A-B) Intracellular FMN (A) and FAD (B) levels in control and patient fibroblasts. (C-D) Complex I (C) and complex II (D) activity in control and patients' fibroblasts. Complex activities are expressed as a ratio to citrate synthase activity. Data are presented as box plots illustrating 80% of the data distribution. 10th, 25th, Median, 75th and 90th percentiles are shown in these and all subsequent box plots. **p < 0.005, ***p < 0.0005, Mann–Whitney U-test. Data were generated from a minimum of three independent experiments. n = 3 and n = 5 for control and patient fibroblasts respectively.

Generation of a novel *Drosophila* model of BVVLS

Using a distinct global driver (*daughterless*-Gal4; *da*-Gal4) in concert with the 7578 RNAi line, we achieved robust *drift* knockdown as determined by semi-quantitative RT-PCR (Figure 3-8). However, this knockdown did not result in early lethality (suggesting stronger RNAi expression by *actin*- relative to *da*-Gal4), facilitating analysis of *drift* knockdown flies at later developmental stages. Using whole-body tissue from *drift* knockdown adults and associated control lines (heterozygotes for *da*-Gal4 and the *drift* RNAi transgene), we

found that *drift* knockdown resulted in a substantial reduction of *in vivo* riboflavin levels as well as the riboflavin metabolites FMN and FAD (Figure 3-9). These results, combined with the high homology of DRIFT to hRFVT1-3, strongly suggest that DRIFT is a *bona fide* riboflavin transporter. We next asked whether *drift* knockdown resulted in reduced mitochondrial activity. Similarly to BVVLS patient fibroblasts, ETC complex I activity was profoundly reduced by *drift* knockdown (Figure 3-9), while ETC complex II and II-III activity exhibit a trend towards lower levels, albeit non-significant (Figure 3-9). Thus, in *Drosophila*, complex I activity appears particularly sensitive to DRIFT expression.

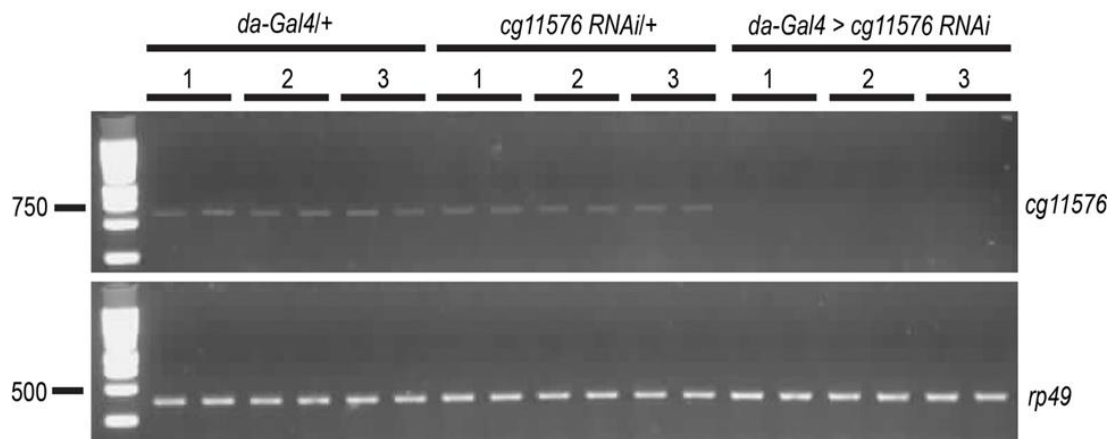


Figure 3-8 Semi-quantitative RT-PCR illustrating *drift* (*cg11576 RNAi*) knockdown
 1% agarose DNA gel for cycle no. 26 and 29 of the PCR for the cDNA of *rp49* and *cg11576* respectively. *da-Gal4/+* and *cg11576 RNAi/+* are the controls for the driver and RNAi line respectively while the knockdown is represented by the *da-Gal4>cg11576 RNAi*. The expected size of the bands are at ~ 620 bp and ~ 370 bp for *cg11576* and *rp49* respectively. DNA ladder (on the left) is in bp. Data were generated from three independent biological samples (1-3), each with two technical replicates.

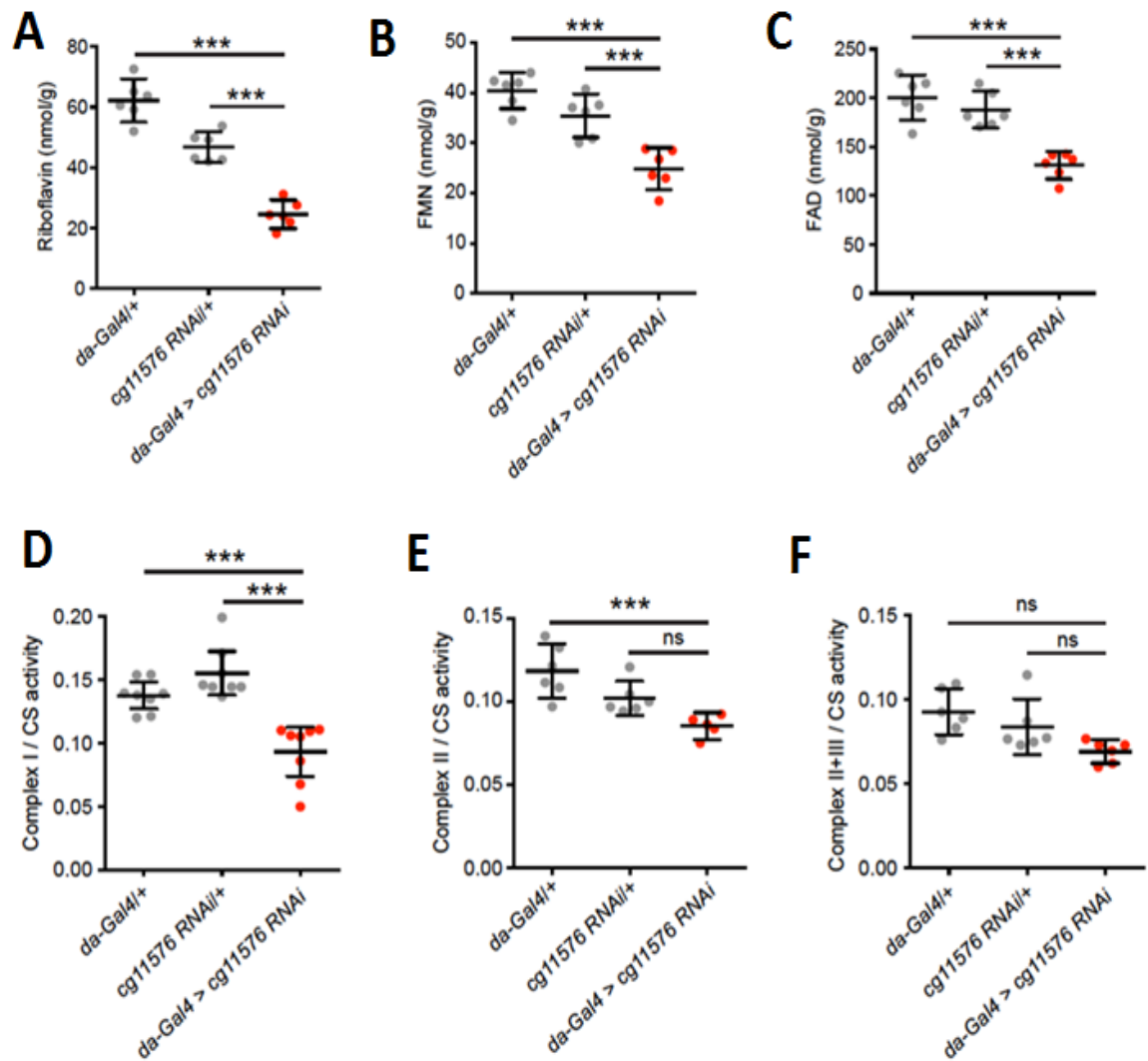


Figure 3-9 Knockdown of *drift* results in reduced mitochondrial activity.

A-C) Riboflavin (A), FMN (b) and FAD (c) levels in *drift* knockdown flies and controls normalised to total protein levels. (D-F) Complex I (D), complex II (E) and complex II-III (F) activity in *drift* knockdown flies and controls. Complex activities are normalised to citrate synthase (CS) activity. *** $p < 0.0005$, ns - $p > 0.05$, one-way ANOVA with Dunnett's post-hoc test. Data were generated from a minimum of three independent experiments. $n = 10$ for each genotype. Individual measurements were performed in duplicates.

drift knockdown results in reduced locomotion and lifespan in *Drosophila*

The viability resulting from *drift* knockdown via *da-Gal4* allowed us to assess whether RFVT knockdown impacts post-embryonic organismal phenotypes in a manner consistent with BVVLS pathology (Foley et al., 2014, Manole et al., 2014). We found that *drift* knockdown resulted in profound locomotor defects in both larval and adult *Drosophila*. *drift*

knockdown 3rd instar larvae exhibit significantly reduced locomotion, as measured by the number of grid crosses per minute on an agar plate (Figure 3-10) We also used the *Drosophila* activity monitor (DAM) system to perform automated recordings of adult locomotion, measured as the number of infra-red beam breaks across a 24 h day/night cycle. Under 12 h light: 12 h dark conditions, control 1-2 day old adult female *Drosophila* exhibit peaks of activity at dawn and dusk, and relative quiescence during the afternoon and night (Figure 3-11). In contrast, peak activity and total beam breaks in *drift* knockdown adults were substantially reduced (Figure3-11). Furthermore, *drift* knockdown resulted in greatly reduced lifespan, with 99% mortality within four days post-eclosion (Figure 3-11). These phenotypes mimic motor problems and early mortality observed in BVVLS patients, suggesting a conserved link between RFVT dysfunction, locomotor strength and lifespan.

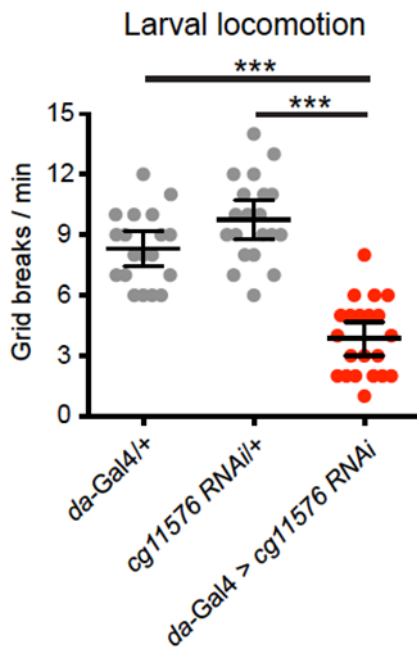


Figure 3-10 *drift* knockdown reduces locomotor activity larvae.

The number of grid breaks per min of wandering larvae. Values are presented as a mean and error bars indicate standard error means (SEM). Statistical analysis was carried out using Kruskal-Wallis test, followed by Dunn's post-hoc test, levels of significance compared to both controls (ns indicates $p > 0.05$, * indicates $p < 0.05$, ** indicates $p < 0.005$, *** indicates $p < 0.0005$). Data were generated from $n=30$ for each genotype.

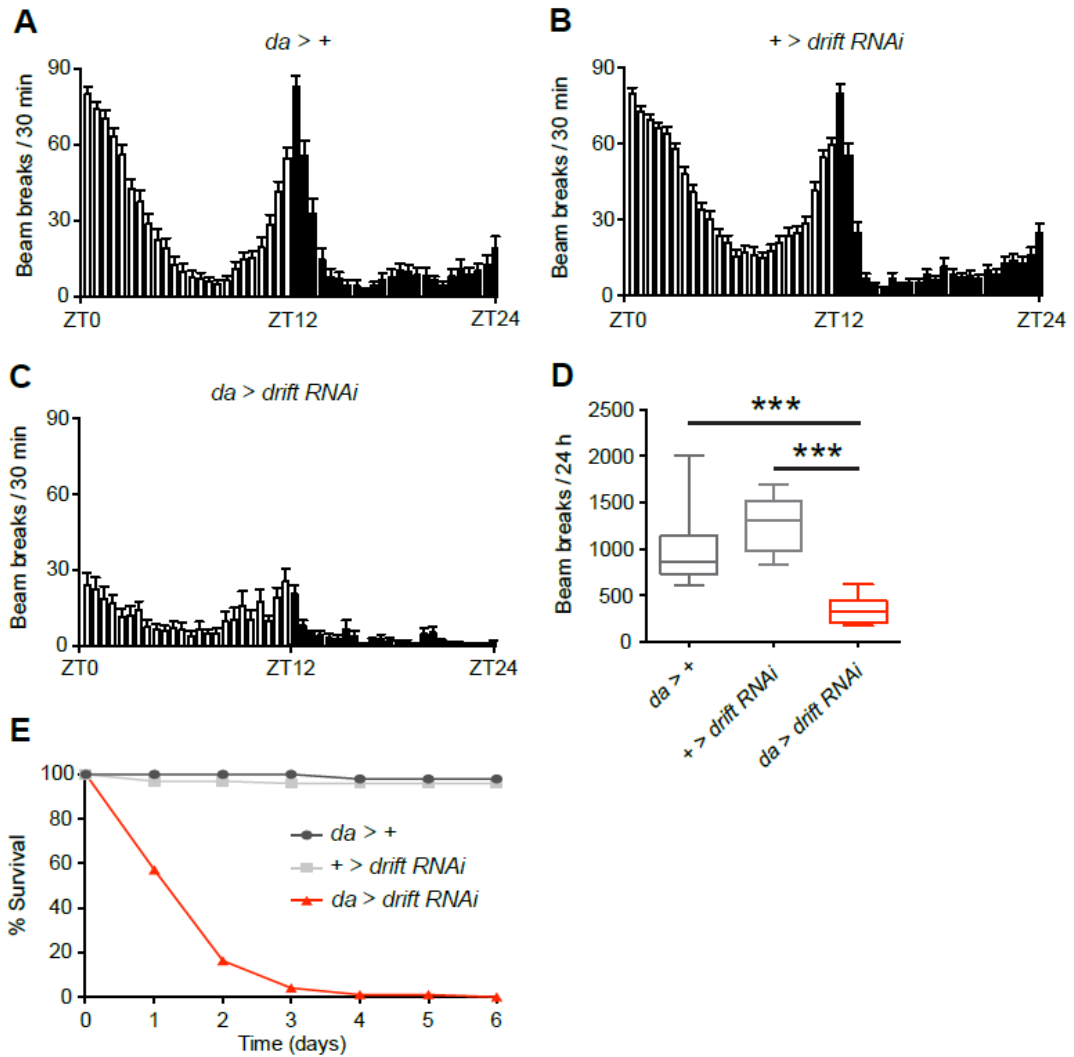


Figure 3-11 *drift* knockdown reduces locomotor activity and lifespan in *Drosophila*.

(A-C) Locomotor activity over 24 h of driver alone (A) and drift RNAi alone (B) controls, and *drift* knockdown flies (C). Data was derived from adult females. Mean values for each time point are presented; error bars indicate standard error of the mean (SEM). Open and filled bars represent the data acquired during the day and night respectively. ZT= Zeitgeber Time. (D) Box plots illustrating total activity over 24 h for each genotype. *** $p < 0.0005$, Kruskal-Wallis test with Dunn's post-hoc test. Data were generated from at least three independent experiments. $n = 30$ for each control and $n = 16$ for the *drift* knockdown flies. (E) Percentage survival of *drift* knockdown flies and controls on normal food. $n = 98$ for each control and $n = 99$ for the *drift* knockdown flies.

An esterified riboflavin derivative partially rescues *drift* knockdown phenotypes

Since BVVLS pathology can be partially ameliorated by riboflavin treatment, we asked whether locomotor defects in *drift* knockdown flies could be rescued by supplementing *Drosophila* culture medium with riboflavin (0.1 mg/ml). However, we found no enhancement of locomotor activity following riboflavin supplementation (data not shown). Riboflavin is a water-soluble vitamin that is easily excreted, leading to low bioavailability and short half-life. Furthermore, since RFVT expression is very low in *drift* knockdown flies (Figure 3-8), riboflavin in the *Drosophila* haemolymph may fail to be transported into relevant cell-types. We sought to circumvent these issues using an esterified derivative of riboflavin (riboflavin-5'-lauric acid monoester; RLAM; 0.1 mg/ml) that could act as a pro-drug, that is likely to diffuse into the intracellular space independently of RFVT function and be cleaved by esterases to release active riboflavin (Figure 3-12). As predicted, food supplementation with RLAM dramatically increased complex I activity (~ 3-fold), and critically, resulted in heightened total locomotion, increased peak levels of daily activity and a partial extension of lifespan (Figure 3-12) in *drift* knockdown flies. We speculate that RLAM may represent a more efficient treatment method for BVVLS patients since cellular uptake of RLAM may still robustly occur in the absence of functional endogenous RFVTs.

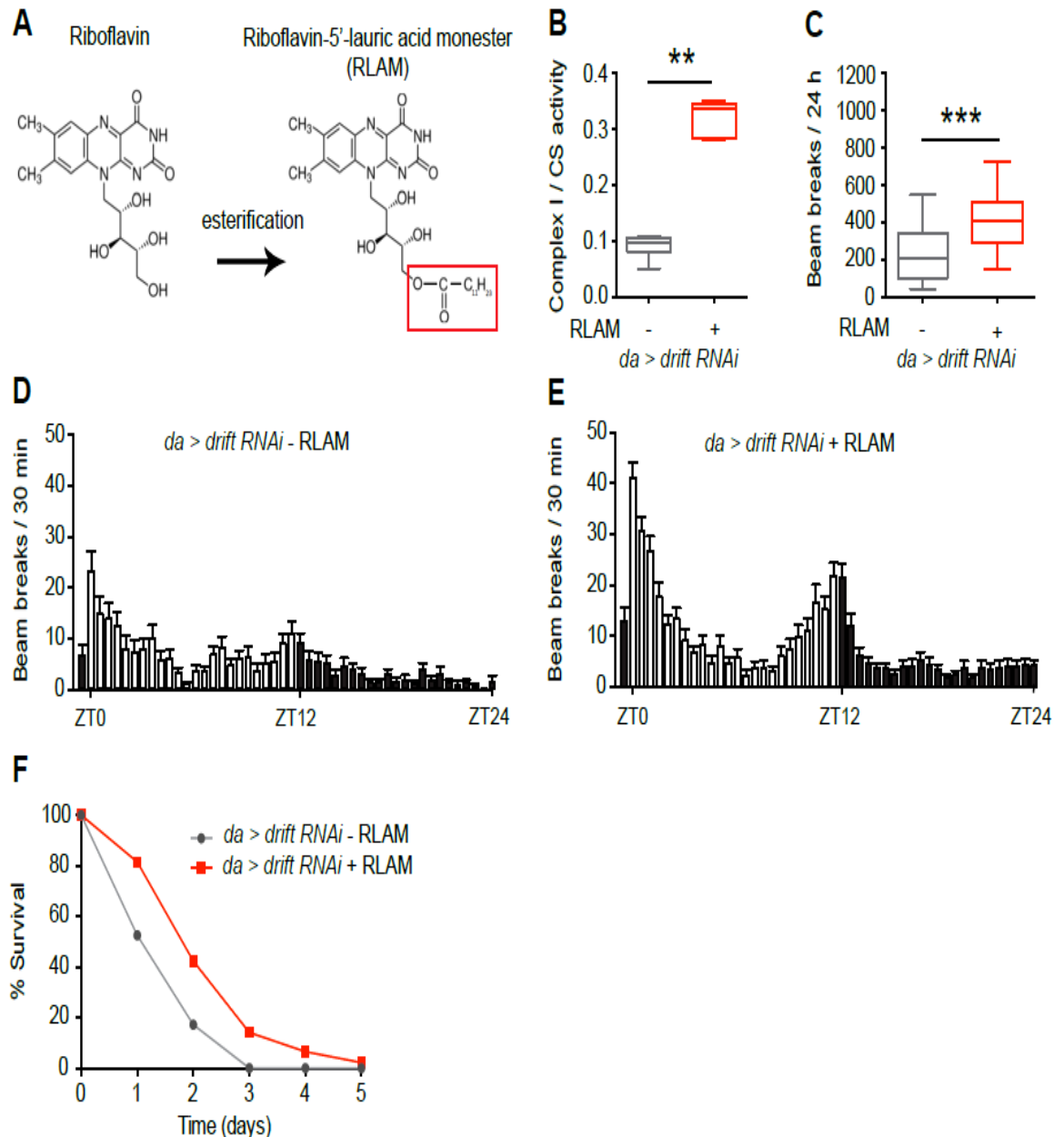


Figure 3-12 A riboflavin ester partially rescues the drift knockdown phenotypes.

(A) Chemical structure of riboflavin and its ester (RLAM). (B) Complex I activity in *drift* knockdown flies grown on normal and RLAM-supplemented food. Complex activity is expressed as a ratio to citrate synthase (CS) activity. Data were generated at least three independent experiments. $n = 10$ for each genotype. Individual measurements were done in duplicates. (C) Total locomotor activity over 24 h in *drift* knockdown grown on normal and RLAM-supplemented food. $**p < 0.005$, $***p < 0.0005$, Mann-Whitney U-test. Data were generated at least three independent experiments. $n = 37$ and $n = 52$ *drift* knockdown fed normal and RLAM-supplemented conditions respectively. (D-E) Mean locomotor activity over 24 hours of the *drift* knockdown flies grown on normal food (D) and RLAM-supplemented food (E). Values are presented as a mean and SEM. Open and filled bars represent the data acquired during the day and night respectively. ZT= Zeitgeber Time. (F) Percentage survival of *drift* knockdown flies grown on normal and RLAM-supplemented food. $n = 99$ and $n = 92$ *drift* knockdown fed normal and RLAM-supplemented conditions respectively, $p < 0.05$ by log-rank test.

Discussion

We expanded the spectrum of genetic defects in RFVTs identifying *SLC52A2* and *SLC52A3* mutations in 15% of cases. It was previously noted that the distinct phenotype of upper limb and axial weakness, hearing loss and optic atrophy could be attributed only to patients harbouring *SLC52A2* mutations (Foley et al., 2014). However, in our cohort of 20 patients, mutations in both *SLC52A2* and *SLC52A3* resulted in similar phenotypes. Recruitment and clinical assessment of the patients was performed by consultants. We recruited patients presenting with cranial neuropathies and sensorimotor neuropathy with or without respiratory insufficiency and we recognize this as a limitations of our study because more atypical presentations would have been missed.

SLC52A3 mutations were more frequent than mutations in *SLC52A2* in our cohort. This is in agreement with previous reports where BVVLS-linked mutations were predominantly found in *SLC52A3* (Bosch et al., 2011, Manole and Houlden, 2015). The high proportion of patients who were found to be negative for mutations in the known RFVTs indicates that novel genetic causes are yet to be found.

The neuropathology of BVVLS has not been fully characterised in the past (Sathasivam, 2008, Malafronte et al., 2013). In keeping with the spectrum of clinical findings, severe depletion of neurons in multiple cranial nerve nuclei, anterior horns of the spinal cord, cerebellar nuclei, Purkinje cells in the cerebellum, and degeneration of optic pathway, solitary tract, and spinocerebellar and pyramidal tracts was seen along with an axonal neuropathy in the sural nerve (Foley et al., 2014). Here we provide detailed neuropathological assessment of the brains and spinal cords in two patients with genetically confirmed mutations in the *SLC52A3* gene, who fell at the two extremes of age of presentation of BVVLS. Briefly, there was variably and severe neuronal loss and gliosis in the brain stem cranial nerve nuclei and anterior horns of the spinal cord with accompanying nerve root atrophy which reflects the spectrum of clinical symptomatology. Whilst no correlation between the mutation type and severity of clinical phenotypes was evident in the case series presented here, it is possible that different mutations directly influence the length of the disease and degree of atrophy of specific brain structures. For example, the rapid deterioration and demise of patient AM2 due to formation of truncated protein originating from nonsense mutations on both alleles may explain less prominent atrophy of cerebellar Purkinje cells when compared with patient AM4, the atrophy of which may require longer

duration of the disease (Manole et al., 2017). In both patients there were symmetrical lesions in the brain stem characterised by prominent neovascularisation, dense infiltration of macrophages, loss of myelin and relative preservation of neurons and axons. Although the anatomical distribution of the symmetrical lesions differed in both cases, the morphology of the lesions was identical and moreover to the pathology seen in mitochondrial encephalopathies (Tanji et al., 2001, Filosto et al., 2007). To the best of our knowledge such lesions have not been documented in any of the previous published cases of BVVL clinical syndrome and link with the mitochondrial abnormalities in flies and patient fibroblasts.

Although fibroblasts are non-neural cells and not particularly vulnerable as a tissue, metabolic and mitochondrial abnormalities are commonly studied in this cell-type (Distelmaier et al., 2009). We identified clear deficiencies in the activities of ETC complex I and complex II in patient-derived fibroblasts relative to fibroblasts from healthy controls. Interestingly, previous results have only shown evidence of marginally decreased ETC complex I activity in muscle cells from some *SLC52A2* patients sensitive to reduced riboflavin uptake (Foley et al., 2014). Mitochondrial activity in different tissues and cell types may thus be differentially sensitive to reduced riboflavin uptake.

Finally, we examined the *in vivo* consequences of knockdown of the single *SLC52A3* homologue *drift* in *Drosophila*. Biochemical analysis of *drift* knockdown tissue is consistent with data derived from patient fibroblasts, showing diminished levels of riboflavin, FMN and FAD, and reduced complex I activity. At the whole-organismal level, there was impairment in locomotion at both the larval and adult stages, reminiscent of the limb weakness and movement impairment of the BVVLS patients. Moreover, *drift* knockdown flies had severely reduced life span, similar to untreated patients (Bosch et al., 2011). It is interesting to note that these lifespan and locomotor defects are rescued by ingestion of an esterified derivative of riboflavin, since this provides further evidence that the phenotypic signatures of *drift* knockdown flies are linked to riboflavin deficiency and consequent downstream metabolic defects. We hypothesize that lack of RLAM during pupation, a critical neurodevelopmental stage during which RLAM-supplemented food will not be consumed, may contribute to the partial nature of the observed RLAM rescue. Nonetheless, RLAM fulfils the criteria for being a treatment targeting the fundamental mitochondrial process of energy metabolism, in addition to circumventing the disease-related protein, features generally believed to be of great promise (Lin and Beal, 2006, Foley et al., 2014, Xuan et al., 2013).

In addition to its role in energy metabolism, riboflavin also acts indirectly as an antioxidant. FAD is needed for the recycling of glutathione as it is a cofactor for glutathione reductase. Glutathione reductase converts oxidised glutathione (GSSG) to reduced glutathione (GSH) which is a scavenger of free radical and reactive oxygen species (ROS) (Henriques et al., 2010). In fact, the erythrocyte glutathione reductase (EGR) test is commonly performed to test for riboflavin nutritional status (Northrop-Clewes and Thurnham, 2012) and could be used to look at the levels of GSH. Furthermore, in addition to its role in the ETC, CoQ₁₀, the predominant form of CoQ, is also an antioxidant and free radical scavenger in its reduced form ubiquinol, protecting against oxidative damage (Mancuso et al., 2010). CoQ₁₀ was able to maintain the $\Delta\Psi_m$ in neuronal cells undergoing oxidative stress (Mancuso et al., 2010). Interestingly, a monooxygenase involved in the biosynthesis of CoQ₁₀ is FAD-dependent (Baker and Tarnopolsky, 2003).

Therefore, oxidative stress which may result from ETC complex inhibition, decreased CoQ₁₀ levels, and/or decreased levels of the antioxidant GSH (the recycling of which is FAD-dependent) could all be investigated by measuring ROS production both in the cytosol and mitochondrial matrix (Gandhi et al., 2009) as possible mechanisms behind the pathology.

It was previously thought that defective mitochondria occur secondary to primary disease mechanism, but current research suggests that mitochondrial dysfunction may play a role in both onset and development of neurodegenerative diseases such as Alzheimer's, Parkinson's, Huntington's and ALS, where decreases in activity of one or more mitochondrial complexes and corresponding oxidative stress have been reported in cell or animal models (McInnes, 2013, Golpich et al., 2016, Menzies et al., 2002, Fukui and Moraes, 2007, Hoglinger et al., 2003, Yamada et al., 2014). Our findings suggests that this may apply to our *in vitro* and *in vivo* models of childhood neuropathy but more investigations should be undertaken to look at for example mitochondrial oxygen consumption and membrane potential as well as mitochondrial structure.

Chapter 4 *SBF1* mutations associated with axonal neuropathy with cranial nerve involvement.

Introduction

Charcot-Marie-Tooth disease (CMT) was first described in 1886 by Jean-Marie Charcot, Pierre Marie and Howard Henry Tooth (Charcot and Marie, 1886, Tooth, 1886). Also known as hereditary motor and sensory neuropathy (HMSN), it is the most common inherited neuromuscular disorder, with a prevalence of about 1 in 3300 depending on the population studied (Barreto et al., 2016, Bansagi et al., 2017).

Symptoms include distal muscle weakness and wasting which is generally symmetrical and becomes proximal with disease progression, sensory loss and foot deformities (Rossor et al., 2015). The onset is usually in the first to third decade and it can be predictive of the severity of the disease (Reilly et al., 2011).

Historically it was divided into demyelinating or axonal subtypes based on neurophysiology data. The demyelinating and axonal forms of CMT may show autosomal dominant (AD), recessive (AR), or X-linked inheritance. CMT3, also known as congenital hypomyelinating neuropathy (CHN) or Dejerine-Sottas disease (DSD), refers to early-onset severe demyelinating CMT. CMT4 refers to AR demyelinating CMT. Since a 1.4-Mb duplication of chromosome 17 containing the peripheral myelin protein 22 gene (PMP22) has been identified as the cause of the most prevalent subtype CMT1A (Lupski et al., 1991), the vast genetic heterogeneity of this disease has been revealed by advances in sequencing technology that have allowed for over 60 genes or loci to be linked to CMT (Rossor et al., 2015). Different pathogenic variants in a single gene may be associated with both autosomal dominant and autosomal recessive inheritance, and both axonal and demyelinating neuropathy, making classification challenging (Rossor et al., 2016). A broad single gene causing CMT description is provided in Table 4-1.

Table 4-1 Single-gene causes of CMT.

Each of the CMT subtypes (CMT1, CMT2, CMT4, and CMTX) is further subdivided primarily on molecular genetic findings. Proportion is based on (Saporta et al., 2011).

Disease Name	Pathology	Mode of Inheritance	Proportion of all CMT
CMT1	Abnormal myelin	AD	40%-50%
CMT2	Axonopathy	AD	10%-15%
Intermediate form	Combination of myelinopathy and axonopathy in individual	AD	Rare
CMT4	Either myelinopathy or axonopathy	AR	Rare
CMTX	Axonopathy with secondary myelin changes	X-linked	10%-15%

CMT4 is a group of progressive motor and sensory axonal and demyelinating neuropathies that are distinguished from other forms of CMT by autosomal recessive inheritance (Reilly et al., 2011). Individuals with CMT4 usually have the clinical characteristics of the CMT phenotype, including distal muscle weakness and atrophy, sensory loss, and, often, pes cavus foot deformity.

Mutations in genes encoding myotubularin-related proteins (*MTMR2* and *SBF2*) are associated with autosomal recessive forms of demyelinating CMT4 (CMT4B1 and CMT4B2, respectively) (Bolino et al., 2000, Azzedine et al., 2003). Mutations in the *SBF1* gene, which encodes another member of the myotubularin family, have been identified in one Korean family with autosomal recessive demyelinating CMT (CMT4B3) but also in one Saudi family with severe axonal neuropathy and additional neurological and skeletal features (Nakhro et al., 2013, Bohlega et al., 2011, Alazami et al., 2014). In contrast to the *Mtmr2*- and *Sbf2*-deficient mice which develop peripheral neuropathy characterized by reduced nerve conduction velocity and myelin out-folding and in-folding, similar to what is observed in CMT4B1 and CMT4B2 patients (Tersar et al., 2007, Robinson et al., 2008), the *Sbf1* knockout mice are phenotypically normal except for a spermatogenesis defect (Firestein et al., 2002). In addition knockdown of *Sbf1* in mouse motor neuron cells did not affect cell proliferation and did not result in transcriptional changes (Nakhro et al., 2013).

In this study, we describe novel variants in *SBF1* as the potential causative mutations in two siblings with severe axonal neuropathy, hearing loss, facial weakness and bulbar features. Our findings support the previous observation that *SBF1* mutations may cause

axonal neuropathy phenotypes in addition to CMT4B3. The findings were reported in (Manole et al., 2017a).

Methods

Two brothers with peripheral neuropathy were investigated. Informed consent was obtained from all individuals and the institutional review boards at the participating medical centres approved the study. Individuals underwent clinical and instrumental assessments during the routine diagnostic process. Neurophysiological studies, MRI scans and skin, muscle and nerve biopsies were performed using standard methods. Genomic DNA from the two affected individuals and four unaffected relatives was used for molecular genetic analyses. Clinical assessment of the patients was performed by consultants.

Whole-exome sequencing

The exomes of individuals II:3 and II:1 were enriched using the Nextera Rapid Capture Exome kit (Illumina) and sequenced on the HiSeq 2500 platform (Illumina). The resulting 100 bp paired-end sequence reads were mapped against the human reference genome assembly 19 (GRCh37) with the Burrows-Wheeler Aligner package (Li and Durbin, 2009) and read duplicates were removed with Picard (<http://broadinstitute.github.io/picard/>). Variant calling and indel realignments were performed with the Genome Analysis Toolkit (GATK) (McKenna et al., 2010) and variants were submitted to ANNOVAR for annotation (Wang et al., 2010). The analysis was performed by Alan Pittmann.

Bioinformatic analysis

cDNA and protein sequence variants are described in accordance with the recommendations of the Human Genome Variation Society (<http://www.hgvs.org>) using Ensembl ENSG00000100241; ENST00000380817 as the reference sequences (<http://www.ensembl.org/>). Evolutionary conservation of nucleotides was assessed using PhyloP (46 vertebrate species) and GERP scores, which were accessed through the UCSC Genome Browser (<https://genome.ucsc.edu/>) using genomic coordinates from GRCh37/hg19. Grantham scores were used to assess the physicochemical nature of the amino acid substitutions. *In silico* analyses of sequence variants were performed using the following pathogenicity prediction tools: SIFT

(<http://sift.jcvi.org/>), PolyPhen-2 (<http://genetics.bwh.harvard.edu/pph2/>) and Mutation Taster version 2 (<http://www.mutationtaster.org/>).

Sanger sequencing

We confirmed causative variant candidates by the Sanger sequencing method using an automatic genetic analyzer. *SBFI* PCR primers were designed using Primer3 so that the PCR products would span whole exons and about 35 bp of flanking introns (<http://primer3.ut.ee/>). Primer sequences are reported in Table 4-2.

Table 4-2 Primer sequences used for PCR and Sanger sequencing of *SBFI*

Exon	Forward / reverse	DNA Sequence
11	Forward	TTGGGGTGTGGAGAAGCTC
11	Reverse	ATGCGCTTATCTCCTACCCC
19	Forward	CTCATGCGTGTGGTGCCG
19	Reverse	GAAGAAACTGTGGGCATGGG
38	Forward	CCAAGTCCCAACCTCCTGT
38	Reverse	ACCAGTTCGACACCCCAA

Touchdown PCR was performed as follows on genomic DNA (50 ng): 95°C for 5 min, followed by eight cycles of denaturing at 95°C for 20 s, annealing at 70°C for 20 s, and extending at 72°C for 30 s. 20 further cycles of the same conditions were run except the annealing temperature was decreased by 0.5°C per cycle until the final annealing temperature reached 65°C. Finally, 12 cycles were run with denaturing at 95°C for 20 s, annealing at 50°C for 20 s and extending at 72°C for 30 s. The reaction underwent a final extension at 72°C for 5 min. PCR amplification products were cleaned with ExoAp. The purified PCR product was split into two and sequenced bidirectionally with the original primers that were used to amplify the region of interest and Big Dye Terminator Kit v.3.1 (Applied Biosystems) at Agencourt Biosciences. Conditions were as follows: 25 cycles of denaturation at 95°C for 10 s, annealing at 50°C for 5 s and extension at 60°C for 4 min. Sequencing reactions were cleaned using CleanSEQ SPRI beads according to the manufacturer's protocol (Agencourt). Sequencing was performed using a 3730 DNA Analyzer (Applied Biosystems). *SBFI* mutation positions are based on NCBI reference sequences: NM_002972, NP_002963 (www.ncbi.nlm.nih.gov).

Results

Clinical features

The proband and his affected brother (II:3 and II:2; Figure 2-1) were the third and second children of healthy, non-consanguineous parents of Spanish descent. Both walked independently at age 14 months. At ages 4 and 9 years, respectively, they were noted to have an unsteady gait and subsequently developed slowly progressive, distal-predominant, muscle weakness and sensory loss in their limbs. They lost ambulation in their mid- to late-30s. In their late 40s, on neurological examination, they had mild ocular movement abnormalities, bilateral hearing loss, upper and lower facial weakness, bulbar features including tongue weakness, dysarthria, dysphagia and reduced or absent gag reflex, lumbar hyperlordosis, mild pes cavus, distal and proximal muscle weakness and atrophy and marked sensory impairment in their limbs. They were unable to stand unaided and their IQ was 90.

Nerve conduction studies were consistent with a severe length-dependent, motor and sensory axonal neuropathy with median and ulnar motor nerve conduction velocities (NCVs) ranging between 49 and 61 m/s (Manole et al., 2017a). CMAPs for the facial nerves were markedly reduced in patient II:3. Needle EMG showed neurogenic motor unit action potentials in the limbs and facial muscles (Manole et al., 2017a).

Brain MRIs in both cases demonstrated mild cerebellar atrophy (Figure 4-1). Skin, tibialis anterior muscle and sural nerve biopsies were performed in patient II:3 at age 34; skin biopsy was unremarkable, muscle biopsy showed features of longstanding neurogenic atrophy and nerve biopsy revealed decreased number of myelinated fibres and axons with relatively thin myelin sheaths (Figure 4-1). Muscle biopsy of patient II:2 at age 32 also showed features of longstanding neurogenic atrophy.

Genetic studies

Genetic analysis of the 17p11.2 chromosome region and direct sequencing of *GJB1*, *AAAS*, *SLC52A2* and *SLC52A3* genes revealed no pathogenic variants. Genetic tests for spinal muscular atrophy, Kennedy's disease, Friedreich ataxia, spinocerebellar ataxia types 1, 2, 3, 6, 7, 8, 12 and 17, dentatorubral-pallidoluysian atrophy, and fragile X-associated tremor/ataxia syndrome were also negative. To identify the underlying genetic cause, we applied whole-exome sequencing (WES) on the proband (II:3) and one unaffected brother (II:1). Analysis focused on nonsynonymous, splice-site and coding indel variants with a minor allele frequency (MAF) of <0.5% in the Exome

Aggregation Consortium (ExAC; exac.broadinstitute.org), Exome Variant Server (EVS; <http://evs.gs.washington.edu>) and 1000 Genomes databases (1000G; <http://www.1000genomes.org>). From a total of 613 variants that met these filtering criteria in the proband, 186 variants in 60 genes co-segregated under an autosomal recessive model and 2 variants in 2 genes under an X-linked model. Of these 188 variants, only 3 involved a gene associated with inherited neuropathy, i.e. the *SBFI* gene. These variants were validated by Sanger sequencing.

Segregation analysis confirmed that both affected siblings and their unaffected father were heterozygotes for the *SBFI* variants c.2209_2210del and c.5197C>T, indicating that these two variants were located in the same allele, and that all affected and unaffected siblings and their mother were heterozygous for the *SBFI* variant c.1168C>G (Figure 4-1).

c.2209_2210del and c.1168C>G are novel variants not previously reported in public databases. c.1168C>G, located in exon 11 of the *SBFI* gene (Ensembl transcript ENST00000380817), leads to the substitution of positively charged arginine for neutral glycine at codon 390 (p.Arg390Gly), affects a highly conserved nucleotide and amino acid and is predicted as being deleterious by pathogenicity prediction tools. c.2209_2210del, located in exon 19, creates a frame shift starting at codon 737 that ends in a premature stop codon 2 positions downstream (p.Leu737Glufs*3).

c.5197C>T is reported in the dbSNP database (rs199972466) and is present in 62 individuals, including one homozygote, in the ExAC database (MAF = 0.053%). This variant is located in exon 38 and leads to the substitution of positively charged arginine for neutral cysteine at codon 1733 (p.Arg1733Cys). c.5197C>T is predicted as being deleterious; however, in the two affected individuals from the present study, this variant was in *cis* with c.2209_2210del, which causes a premature stop codon 994 amino acids upstream. Thus, the contribution of c.5197C>T to the observed phenotype is uncertain.

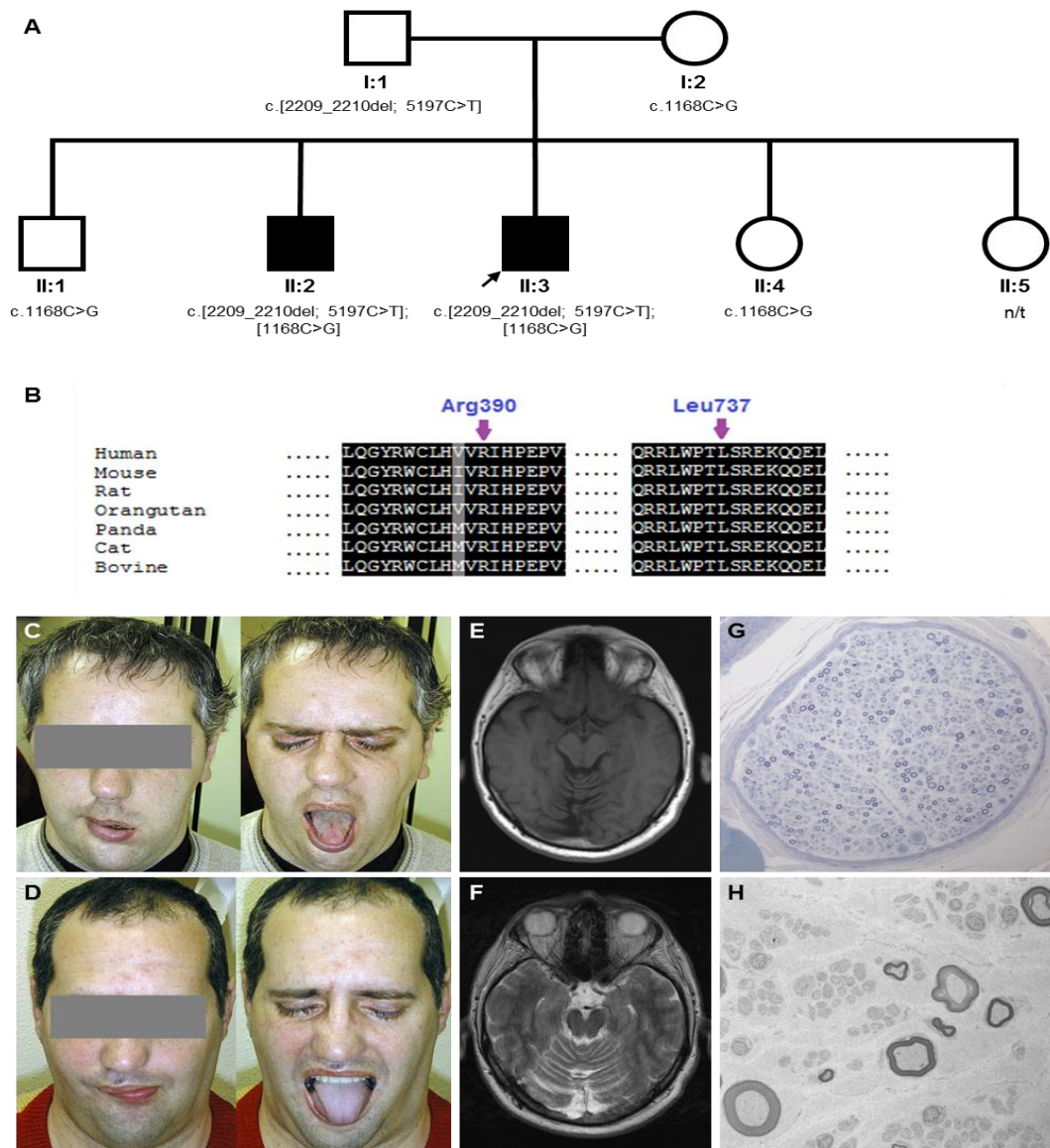


Figure 4-1 Characteristics of *SBF1* family from this study

A) Family pedigree and segregation of *SBF1* variants; genotypes are indicated below tested individuals (*n/t* not tested). B) Structural conservation of the relevant amino acid residues (Arg390 and Leu737) in *SBF1* across 7 species (*single letters* = amino acid residues; *black* = identical; *grey* = conserved substitution); conservation among species of the affected amino acid residues was determined using Ensembl to retrieve the sequences and ClustalW2 software for multiple sequence alignment. C), D) Clinical images of patients II:2 C and II:3 D showing asymmetric facial involvement at rest (left images) and incomplete eye closure (right images); note the preserved tongue muscle bulk in patient II:3 and tongue atrophy in patient II:2 E), F) Axial brain MRI images of patient II:2 (T1-weighted image) and patient II:3 (T2-weighted image) showing atrophy of the cerebellar vermis. G), H) Histopathological findings in sural nerve biopsy of patient II:3; transverse semi-thin section (G; Toluidine blue stain, magnification $\times 400$) and electron micrographs (H; original magnification $\times 6200$) showing decreased number of myelinated axons of all diameters and occasional moderately thin myelin sheaths.

Discussion

In this study we have identified two novel compound heterozygous variants in *SBF1* as the probable causative mutations using WES in two siblings with a severe axonal neuropathy, hearing loss, facial weakness and bulbar features.

Myotubularins comprise a group of catalytically active and inactive proteins involved in membrane trafficking and endocytosis (Laporte et al., 2003, Hnia et al., 2012). Inactive myotubularins such as *SBF1* and *SBF2* interact with and regulate their active homologues by heterodimerization, and coiled-coil domains seem to be crucial for this interaction (Hnia et al., 2012, Kim et al., 2003, Laporte et al., 2003). *SBF1* interacts with the *MTMR2* lipid phosphatase and deletion of the coiled-coil domain of *SBF1* leads to an altered cellular localization of *MTMR2* *in vitro* (Kim et al., 2003). The frameshift mutation p.Leu737Glufs*3 detected in our family may result in a truncated *SBF1* protein lacking the coiled-coil domain, which could affect the activity and distribution of *MTMR2*; alternatively, the mutation may cause lack of expression due to nonsense-mediated decay. Of note, nonsense and frameshift mutations are common in *SBF2*-related *CMT4B2* (Azzedine et al., 2003, Hirano et al., 2004, Baets et al., 2011).

Both *SBF1* and *SBF2* but not *MTMR2* contain DENN domains (differentially expressed in normal and neoplastic cells domain region) involved in regulation of Rab GTPases, which are in turn central regulators of membrane trafficking (Marat et al., 2011). Pathogenic mutations affecting the dDENN (downstream DENN) motif of the DENN domain have been identified in two families with *CMT4B* (p.Met417Val in *SBF1* and p.Leu351_Glu432del in *SBF2*) (Senderek et al., 2003, Nakhro et al., 2013). The novel variant p.Arg390Gly detected in our family is also located within the dDENN motif of *SBF1*, which suggests pathogenic relevance (Figure 4-2).

Our cases have several similarities with the previously reported Saudi family carrying the homozygous *SBF1* variant p.Asp443Asn (Alazami et al., 2014, Bohlega et al., 2011). All except one individual became immobile before their 40s, indicating a severe neuropathy in both families. Like our cases, all Saudi brothers developed facial weakness; in addition, one of them had mild dysarthria and another had dysphagia, features that were observed in our family (Bohlega et al., 2011). Electrophysiology was consistent with an axonal neuropathy in all individuals although sensory/motor NCVs were decreased in one of the Saudi brothers. Nerve biopsy in both probands showed a decreased number of myelinated axons with no onion bulbs. Some of the features

observed in the Saudi family, however, were mild (ophthalmoparesis) or absent (cognitive impairment, microcephaly and syndactyly) in our cases. Given this phenotypic variability and the previous association of *SBF1* with CMT4B3, additional studies are needed to define the clinical spectrum of *SBF1*-related neuropathies.

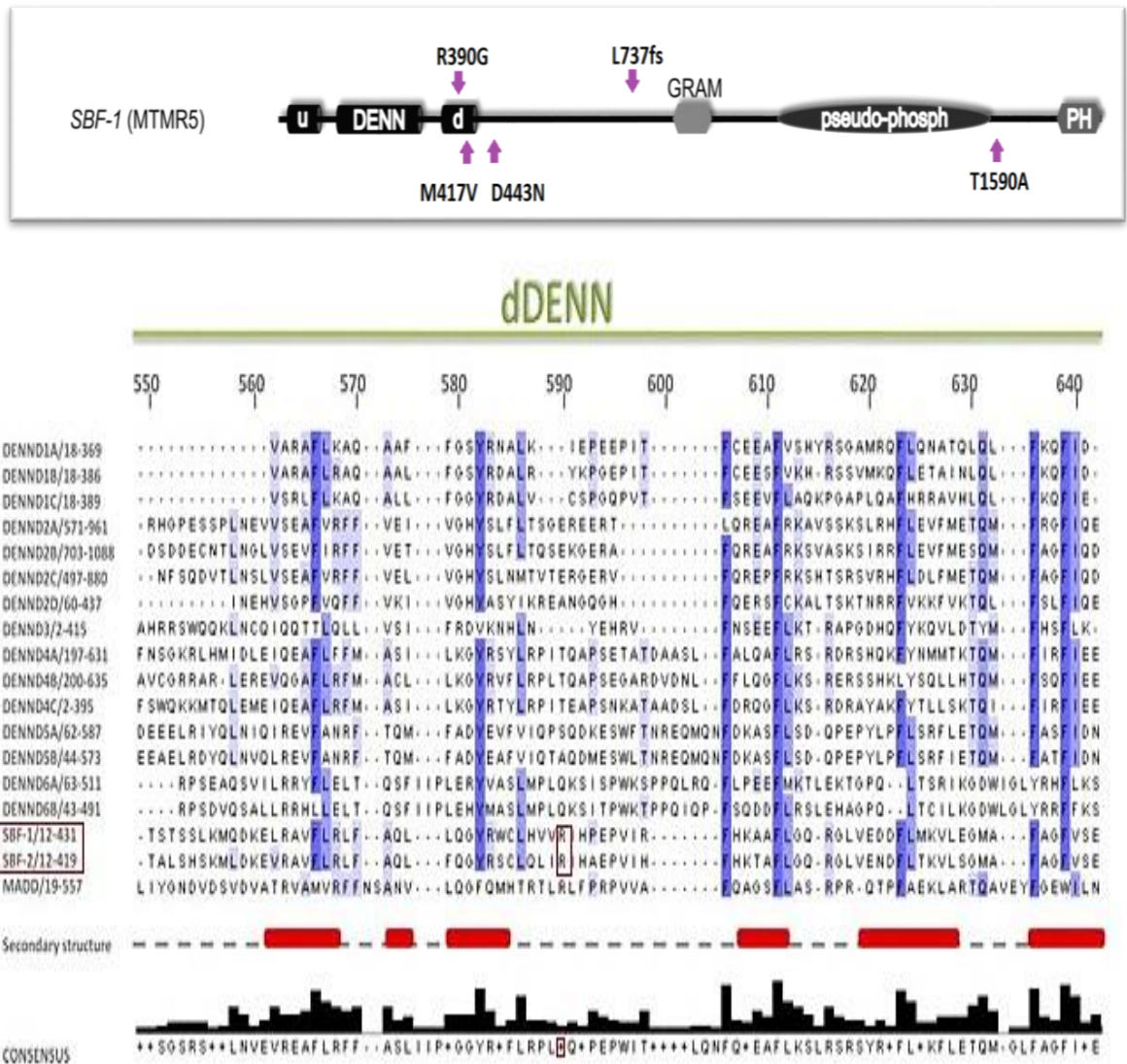


Figure 4-2 Domain models of the DENN domain-bearing protein SBF1

Top: above the scheme are represented the mutations that have been found in this study and below are represented mutations that have been previously reported. u, uDENN module; d, dDENN module; GRAM, glucosyltransferase/Rab-like GTPase activator/myotubularin domain; pseudo-phosph, pseudo-phosphatase domain; PH, pleckstrin homology. Bottom: amino acid sequence alignment of the 18 human DENN domain proteins. Alignment was performed with ClustalW and manually modified using Jalview. Shaded boxes represent conserved residues, with darker shadings based on increasing percent identity. Secondary structure predictions are also indicated along the gray dashed line below the alignment. α -helices are represented as red rectangles. Highlighted in a red rectangle is the R390 residue that is mutated in the proband. The consensus sequence below shows the need for a positively charged residue. Modified from Marat et al., (2011).

Chapter 5 Severe axonal neuropathy is a late manifestation in hereditary spastic paraplegia

Introduction

The hereditary spastic paraplegias (HSPs) are heterogeneous inherited neurological disorders, resulting in progressive spasticity of the limbs, bladder dysfunction and walking difficulties. Other features such as weakness, ataxia, cognitive decline and peripheral neuropathy are present in complex HSP. They are classified genetically as autosomal dominant (AD), autosomal recessive (AR) and X-linked HSP (XL); and clinically as pure or complicated HSP, based upon the absence (pure) or presence (complex) of additional features (Table 5-1). Age of onset is early childhood through 70 years (Finsterer et al., 2012).

The estimated global average prevalence is around 1 in 50000 for both autosomal and recessive forms of HSP (Ruano et al., 2014). Pure forms are more prevalent in Northern Europe, Japan, and North America (Ishiura et al., 2016) while complicated forms are generally more prevalent in Mediterranean countries (Coutinho et al., 1999), due to the increased frequency of consanguinity. To date, more than 70 different disease-loci and more than 50 spastic paraplegia genes (SPGs) have been identified (Lo Giudice et al., 2014, Kara et al., 2016).

Table 5-1 Broad classification of hereditary spastic paraplegias.

<i>Pure</i>
AD (SPG8, 12, 19, 37, 41, 42)
AR (SPG28)
XL (SPG34)
<i>Complex</i>
AD (SPG9, 17, 29, 33, 36, 38)
AR (SPG15, 18, 20, 23, 24, 25, 26, 27, 32, 39, 43, 44, 45, 46, 47)
XL (SPG1)
<i>Pure or complex</i>
AD (SPG3, 4, 6, 10, 13, 31, 40)
AR (SPG5, 7, 11, 14, 21, 30, 35, 48)
XL (SPG2, 16, 22)

In the past, axonal neuropathy has been infrequently associated with complex HSP and *SPG11* mutations, although this is usually mild (Kara et al., 2016). Recently mutations

in *SPG11* have been shown to cause Charcot–Marie–Tooth disease type 2 (CMT2) as a distinct clinical phenotype (Montecchiani et al., 2016).

Spatascin is expressed ubiquitously in the nervous system (Lo Giudice et al., 2014) and the sural nerve biopsy pathology in typical *SPG11* cases showed a loss of unmyelinated nerve fibers and accumulation of intra-axonal pleomorphic membranous material. In CMT2 cases sural nerve biopsies showed similar intra-axonal inclusions but also predominantly loss of large myelinated fibers, mainly in fibers of large caliber, in line with the diagnosis of CMT2 (Montecchiani et al., 2016). Although the role of the protein is unknown, it seems to be important to the survival of neurons (Southgate et al., 2010). In this study we describe novel frameshift mutations in *SPG11*, identified by whole exome sequencing, segregating with the disease and investigated using mRNA. The causative mutations were found in two sisters with complex HSP consistent with *SPG11*, associated with the late manifestation of severe axonal neuropathy. A similar presentation was found in a second, unrelated Cypriot family. The findings were reported in (Manole et al., 2016).

Methods

In family F1, two sisters with complex HSP were investigated who had with clinical features as described below. Informed consent (UCLH: N99/103) was obtained from all individuals and the institutional review boards at the participating medical centers approved the study. Acquired spastic paraplegia was excluded and neurophysiological studies and MRI scans were performed using standard methods. Genomic DNA samples from the two affected individuals and two unaffected relatives were used for molecular genetic analyses. The mutation in the Cypriot family was previously reported (Kara et al., 2016). Clinical assessment of the patients was performed by consultants.

Whole exome sequencing

Exome sequencing was performed as previously described in Chapter 2 using the Agilent SureSelect kit and run on the Illumina HiSeq2500. The resulting 100 bp paired-end sequence reads were mapped against the human reference genome assembly 19 (GRCh37) with the Burrows-Wheeler Aligner package (Li and Durbin, 2009) and read duplicates were removed with Picard (<http://broadinstitute.github.io/picard/>). Variant calling and indel realignments were performed with the Genome Analysis

Toolkit (GATK) (McKenna et al., 2010) and variants were submitted to ANNOVAR for annotation (Wang et al., 2010).

The average sequencing depth was 55-fold with variants being filtered according to pathogenicity, inheritance pattern, and segregation in the family.

Sanger sequencing

We confirmed causative variant candidates by the Sanger sequencing method using an automatic genetic analyzer. *SPG11* PCR primers were designed using Primer3 so that the PCR products would span whole exons and about 35 bp of flanking introns (<http://primer3.ut.ee/>). Primer sequences are listed in the Table 3-2.

Touchdown PCR was done using the PCR Master Mix (Roche) and is described in Table 3-3. PCR amplification products were cleaned with ExoAp. The purified PCR products was split into two and sequenced bidirectionally with the original primers that were used to amplify the region of interest and Big Dye Terminator Kit v.3.1 (Applied Biosystems). Conditions were as follows: 25 cycles of denaturation at 95 °C for 10 s, annealing at 50 °C for 5 s and extension at 60 °C for 4 min. Sequencing reactions were cleaned using CleanSEQ SPRI beads according to the manufacturer's protocol (Agencourt). Sequencing was performed using a 3730 DNA Analyzer (Applied Biosystems). *SPG11* mutation positions are based on NCBI reference sequences: NM_001160227, NP_001153699 (www.ncbi.nlm.nih.gov).

Fibroblasts generation and maintenance

Patients were enrolled with informed consent from the patient and/or their parental guardian. This study was ethically approved by the UCL/University College London Hospital Joint Research Office (99/N103), and written informed consent to perform a skin biopsy and fibroblasts was obtained as appropriate. The 6 mm punch skin biopsies were taken under local anaesthetic at the NHNN. Fibroblasts of the *SPG11* patients were generated at the Institute of Neurology, UCL by Chris Lovejoy.

Fibroblasts were grown at 37°C in 95% air and 5% CO₂ as described in Chapter 2. Fibroblasts of passage number 3 to 5 were used in experiments.

RNA isolation and reverse transcriptase

Total RNA was extracted from cultured skin fibroblasts (90% confluent T75) using Direct-zol™ RNA Miniprep (Zymo Research, USA) according to the manufacturer's instructions and 1 µg was reverse transcribed to first strand cDNA by using random primers and Moloney murine leukemia virus (M-MLV) reverse transcriptase (Promega Corporation, Madison, WI, USA). The concentration and purity of RNA was determined spectrophotometrically.

PCR amplification and sequencing of cDNA

Three primer pairs were designed in flanking exons of those of interest to amplify the coding sequence of exons 22 and 30 of *SPG11* mRNA (Table 5-2). Sanger sequencing was performed as above.

Table 5-2 *SPG11* PCR primer sequences used for PCR and sequencing.
 Primers used for sequencing of cDNA are coloured in purple. F=forward, R=reverse

1F	AGTTAAGCAGAGTGGGAC	21F	TCATTAGAGAGTTCCATGTG
1R	TGAATAATGAAAGAATCAGC	21R	AAGTGATCCTCCTGCTTC
2F	ACTTATTCAACCCTTCTACC	22F	CTGATTTAATTCCATTTGC
2R	ACCTCTATGACTTTTCCTG	22R	AAACACTCACAATTCAATG
3F	ATCAAATCAAATGTACCAG	23F	CTATTCAAACAGAAATGCTC
3R	TTCCTATATCCCAGCTCC	23R	ACACCAGAGTTGTTCAAAG
4F	ACTTCATAGTCATCTGGTTG	24F	TTTCCAGTTCAAGCTAAAG
4R	TAGCCAGTGGTCAGTTATAC	24R	AGGCCTATGTCATGTCTAC
5F	TTAACAGGAGCAGTAGTAAC	25F	CTCTAACATTTTCAGCTCC
5R	TTTAATGAAAGGTACAGC	25R	ATTATCAGCCTTTCCTGTC
6F	TTTTAAGAACATCTTTGCC	26F	CAGGAAATATCCATCTGTAG
6R	GAGGCAGAAAGTAAAATACAG	26R	CATCATTATCTGTTGTTGG
7F	AAAACCATGATGAGTTAAG	27F	TATTTGGCATTATTCATTG
7R	TAAGCAGAGTTAGGGTAATG	27R	CGAGTGAGACACCAAGTC
8F	AGTCTCACCATTAATTC	28F	TTTCTTAGAGGTTCCCAG
8R	ATGACTAAGTTTGGCAAG	28R	AATTCCTAACTACCCCTC
9F	AATAAGACATTGGTCCTG	29F	TTTTCTTTAACCAATTAC
9R	TACCCAAATGTAGTAAATGG	29R	CAGATCAAGACCATCTG
10F	TACCAAGTTTGAATTTTGAC	30F	GATATACTTAGGGAACATTAGC
10R	GAATTCTGTTTCTTCTATTG	30-1F	AACTGGAGAAGGAAAAC
11F	AAATGTATAATCCCATGTTG	30-1R	GAGCCATAGAGAGCTAGG
11R	AATGTCATTATTTCTTAGTGTC	30-2F	GAAATCAGGAGGAAACAG
12F	AGGGTGTCTGTATCTAAC	30-2R	CTTCCTCTTGGAGAXAG
12R	TCTTCCAAGTTTCTTC	31F	ATTCCTGGAAGAGGGCAAT
13F	AATAATCTTTAATCCCAGC	31R	TTATCATCTAAAAGGCTGAC
13R	AGTCCACATAAGAAACTTG	32F	CTGCTGAGGGTGAGGAGTCT
14F	AAAAGAGTGGATGTTCTTG	32R	TGCAATCCAGAACTTGAGAGA
14R	AATATTATTTCCCGAAAGG	33F	AAGGGTTTCAAGCTCAGCAA
15F	CACAGCGAGATCCTGTCTCA	33R	TAGGCATCCAGAGCAGGAAAC
15R	GGATTTATGGCATTTCAAAGGA	34F	CTTTGAGGATTGTGCCATGA
16F	TTTTAAGTAATTGAGACCTAAAC	34R	GCCCAGCCAACCTCAAGTA
16R	AAAGTCACATTCAGGAGTC	35F	GGCATCTGAAAGCAACCACT
17F	TTAAATGCTAATCATCGC	35R	CTTGGGGAGGTCCCTAATTC
17R	TTCACAAGTTTAATACCATTC	36F	TTTAAGGTTTCTCCCTTTAG
18F	TCTCTCAGTTCATTGTTACC	36R	ACATAGTCAAACCCCATC
18R	TTTAAATTCAGCCTTATCC	37-38F	CTATTCTAGCCACGATCAC
19F	ATCTTGTTTCACAAGGTTT	37-38R	GACCTTACCTCTGGGTTT
19R	GAAAGATCTAGAGTGATTTCTG	39F	TTGTTTTCTACAACAGTTTG
20F	GAGCAGACTACCTCTGAAG	39R	TTAGCCATAAAAATTCTTACAC
20R	GAAAAC TAGATTGGCATTAC	40F	TGGGCAACAGAGTAAGAC
		40R	GCTGTCTGAGGAAGAGGAA
21F	AGCTATAGGAGATGCATGGAGT	23R	TGGCTGCTAGATTCAGTGA
29F	AGCTGAGTTACCTGTGGACA	30_1R	CACCACTAGTTGAGATCTGTGC
30_1F	ACGTGGTGCCTTGGATAAG	31R	CTGCTTATGTCTGCTGTGGAC

Table 5-3 SPG11 PCR program for sequencing of genomic and cDNA

Temperature (°C)	Time (min:s)	Number of cycles
94	01:00	
94	00:30	} x15
70	00:30	
72	00:30	
94	00:30	} x16
70*	00:30	
72	00:30	
94	00:30	} x14
65	00:30	
72	00:30	
72	05:00	

*Reducing temperature in each cycle.

Results

Clinical features

The proband and her sister from family F1 (II:1 and II:2;) were the first and second children of healthy, non-consanguineous parents of British descent. At ages 19 and 16 years, respectively, they presented with progressive walking difficulties with additional features of bulbar dysarthria, cognitive problems, limb weakness (proximal power MRC 2/5 and distal 1/5 on examination at the age of 39 and 36, respectively), bladder dysfunction and optic atrophy. At first in their early 20s, limb tone was increased and reflexes were brisk with extensor plantars and no sensory abnormalities but at the ages 39 and 36 reflexes were absent and there was distal sensory loss to pin prick, light touch and temperature. Their fingers were long and tapering, palms were discolored and there was significant limb pain. In addition to having leg oedema the feet of both sisters had strikingly black coloration which improved with massage. Cognitive tests showed an IQ of 54 for the proband, with only a very limited assessment was possible in the sister due to severe motor and language impairment in the context of complex HSP. The overall picture was one of global and severe cognitive impairments, occurring at an early age with relative sparing of visual perceptual functions and normal hearing.

The proband in the Cypriot SPG11 (F1AII:2) family had similar clinical features and initially presented at the age of 21 years with a complex HSP phenotype. When this patient was re-examined and investigated at the age of 42 years she had low tone and absent reflexes along with likely distal sensory abnormalities that were difficult to define with the severe cognitive features but these occurred early in the disease. Her feet showed similar discolouration but she did not suffer from any pain (Table 5-4) and which

is strikingly different to typical *SPG11* patients. Nerve conduction studies show a severe length-dependent axonal sensory-motor polyneuropathy affecting both lower and upper limbs. The neuropathy was compared with other typical *SPG11* cases with complex HSP and was significantly worse (Table 5-4). Brain MRIs in both cases showed that the corpus callosum was thin with periventricular white matter changes and possible cerebellum atrophy (Figure 5-1).

Table 5-4 Nerve conduction studies and electromyography in SPG11 patients.

NCS and EMG in the proband from family 1 (II:1) and family 1A (II:2) reported here as compared with other probands (F2, F4-6, F8, F16 and F26) from different SPG11 families (table 1). Key: NR = no response, Amp = amplitude, lat = latency, DML = distal motor latency, Compound Muscle Action Potential = CMAP), M = moderate, Y=yes, N=No, microvolts (uV), metres per second = m/s, milliseconds = ms.

Case	Motor nerve conduction studies									Sensory nerve conduction studies						EMG		Summary findings of NCS and EMG
	Median nerve			Ulnar nerve			Tibial nerve			Median nerve		Ulnar nerve		Sural nerve		Limbs. Upper:lower		
	DML (ms)	CMAP amp (uV)	MCV (m/s)	Distal lat (ms)	CMAP amp (uV)	MCV (m/s)	Distal lat (ms)	CMAP amp (uV)	MCV (m/s)	SNAP amp (uV)	SCV (m/s)	SNA P amp (uV)	SCV (m/s)	SNA P amp (uV)	SCV (m/s)	Chronic denervation		
F1 II:1	3.3	2.7	48	2.8	2.4	63	5.1	0.3	N/A	12	68	6	60	NR	NR	Y	Y	Severe sensory-motor axonal neuropathy
F1A II:2	4.4	0.4	41	N/A	NR	N/A	4.7	0.1	36	17	50	6	51	NR	NR	Y	Y	Severe sensory-motor axonal neuropathy
F2	3.3	10.7	55	2.4	11.9	58	4	3.9	53	25	62.5	23	59	14	41.5	N	N	Normal NCS/EMG
F4	3.7	0.9	40	4.1	3.7	42	5.5	3.6	43	N/A	N/A	N/A	N/A	11.6	35	M	M	Mild axonal neuropathy
F5	4	4.9	51	2.4	10	61	3.4	5.2	48	28	61	13	67	11	55	N	N	Normal NCS/EMG
F6	3.2	8.3	56	2.3	8.9	62	2.8	3.7	45	23	65	15	64	12	48	N/A	N	Normal NCS/EMG
F8	3.9	7.3	64	N/A	N/A	N/A	4.8	5.3	45	19	61	9	50	6	55	N	M	Mild axonal neuropathy
F16	4.1	6.6	52	N/A	N/A	N/A	5	3.4	42.5	15	57.5	14	53.5	14	41.5	N	N	Normal NCS/EMG
F26	3.6	6.1	53	3.8	3.8	43	5.9	3.3	35	28	54	19	56	9	40	M	M	Mild axonal neuropathy

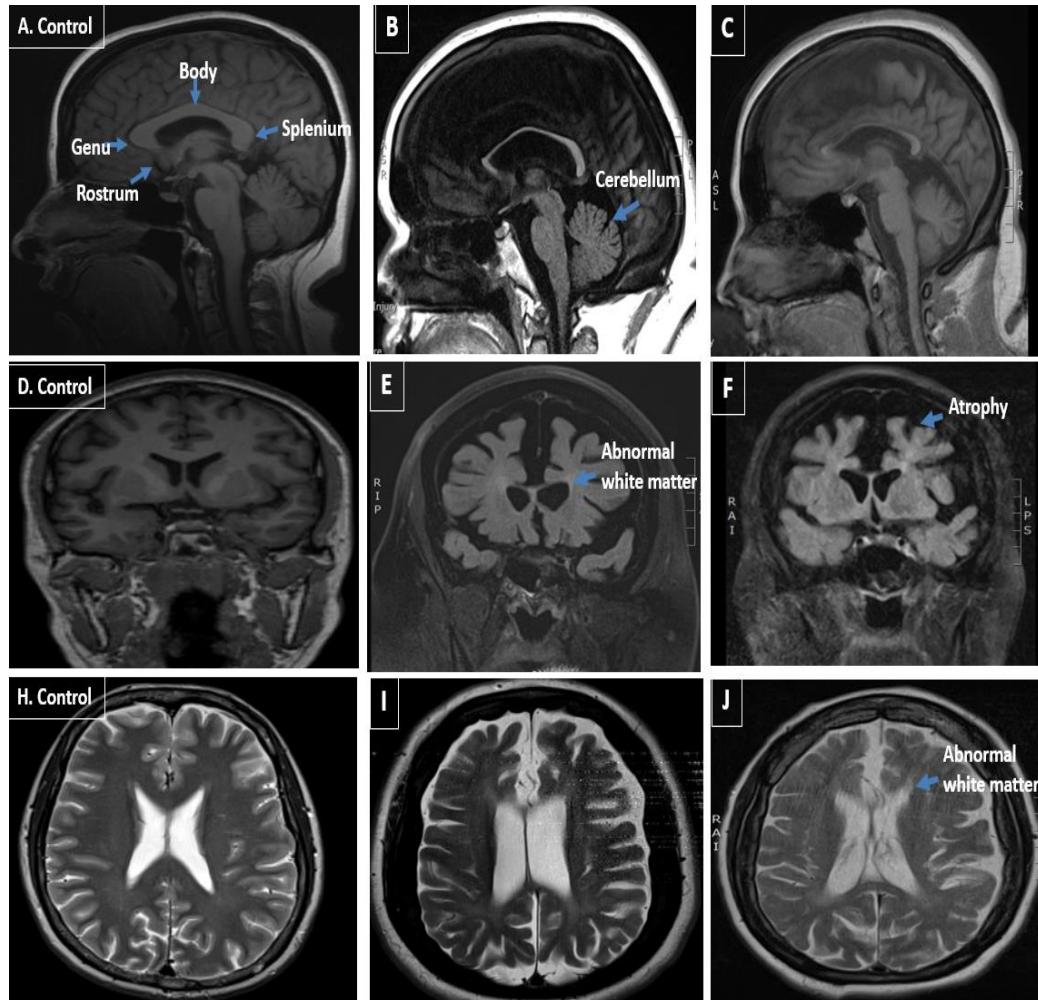


Figure 5-1 Sagittal MRI sequence.

A. control MRI with corpus callosum labelling. B. proband II:1 and C. case II:2 showing thinning of the corpus callosum and cerebral atrophy. Coronal MRI sequence; D. control. E. proband II:1 and F. II:2 showing generalised atrophy with periventricular white matter abnormalities. Axial MRI sequence; H. control. I. proband II:1 and J. II:2 showing periventricular white matter abnormalities.

Genetic studies

To identify the underlying genetic cause, we applied whole-exome sequencing (WES) on the proband (II:1), her affected sister (II:2) and her mother (I:1). Analysis focused on nonsynonymous, splice-site and coding indel variants with a minor allele frequency (MAF) of <0.5 % in the ExAC; (www.exac.broadinstitute.org), EVS; (<http://evs.gs.washington.edu>) and 1000G; (<http://www.1000genomes.org>). From the variants that met these filtering criteria in the proband, a few co-segregated under an autosomal recessive model and at least one was present in the mother. Of these variants, only two involved a gene associated with complex HSP, i.e., the *SPG11* gene. These variants were validated by Sanger sequencing. Segregation analysis confirmed that both affected siblings and their unaffected father were heterozygotes for the *SPG11* variant in exon 22, c.3729delC. Moreover, both affected sisters and their mother were heterozygotes for the variant in exon 30 c.5148dupA, also indicating that these two variants were located on the different alleles (Figure 5-2). The variant in exon 22 is a one bp deletion which creates a frameshift disrupting the sequence from codon S1243. The new reading frame ends in a stop 6 codon positions downstream. Similarly the variant in exon 30 is a one bp duplication which creates a frameshift disrupting the sequence from codon H1717. The new reading frame ends in a stop 3 positions downstream. To analyze the consequence of these mutations, we isolated RNA from the fibroblasts of the two affected sisters and their mother, extracted RNA and carried out RT-PCR. From our data the mutant allele is clearly present in the cDNA (Figure 5-3) and likely to exist as a truncated protein, indicating that very little RNA has been targeted for non-sense mediated mRNA decay. The Cypriot family were found to have a homozygous c.6658_6659delAT, p.M2220Dfs*27 mutation. This is consistent with a typical *SPG11* loss of function mutation.

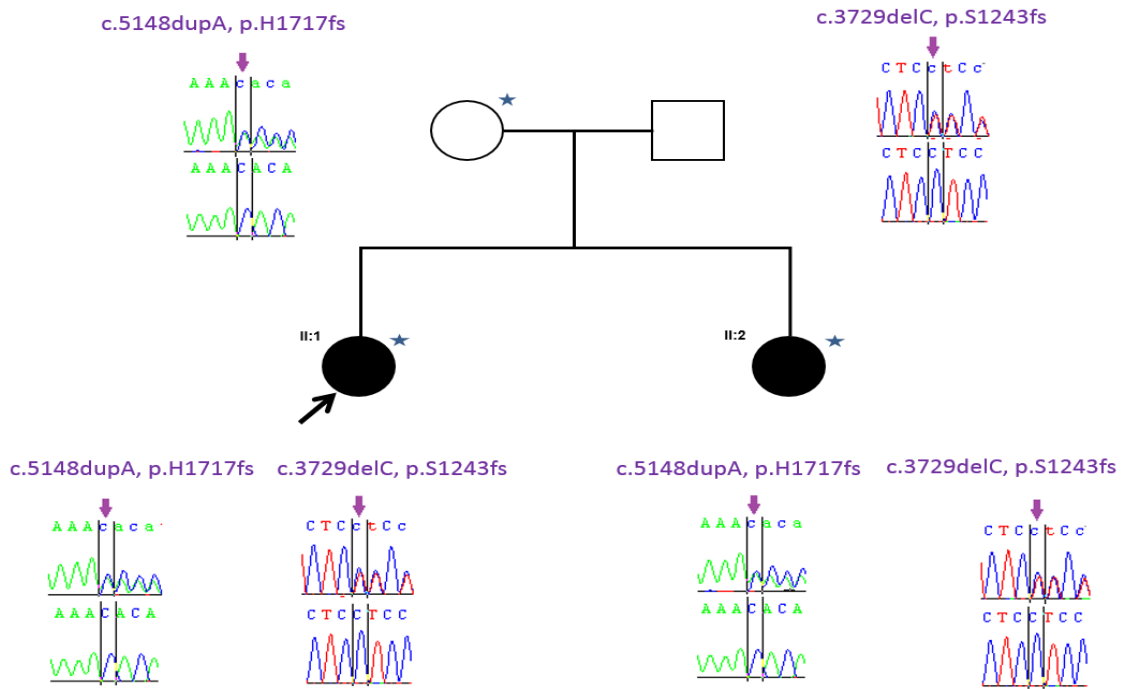


Figure 5-2 Pedigree of the F1 SPG11 family.

Open symbols represent unaffected individuals and filled symbols represent affected individuals. The proband is indicated by an arrow. Stars indicate individuals whose DNA was used for whole exome sequencing and whose skin biopsies were used for fibroblast studies. Sanger sequencing chromatograms surround the symbols and show segregation of mutations. Black bar encompass the sites of interest (mutation over control site).

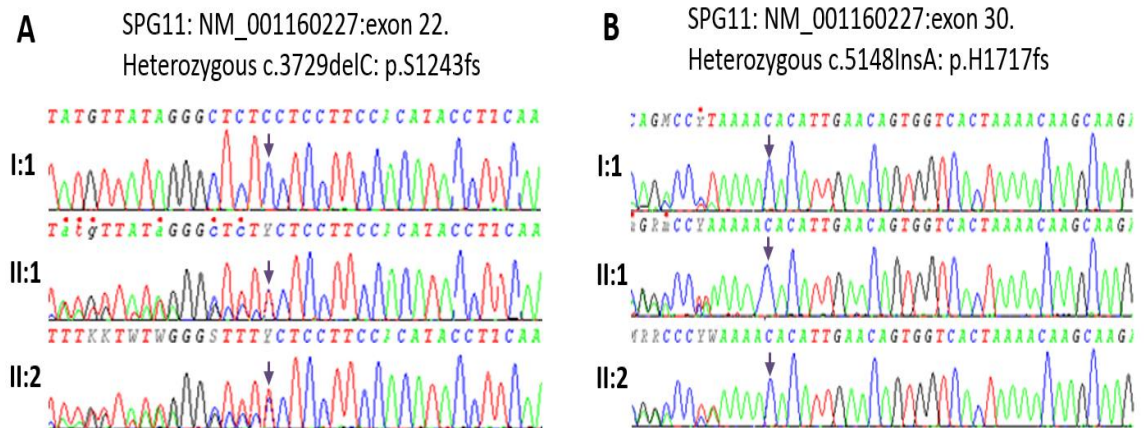


Figure 5-3 cDNA sequencing chromatograms

A. cDNA sequencing chromatograms of the heterozygous exon 22 SPG11 mutation in the mother (I:1 same as control sequence) and two affected siblings (II:1 and II:2) with deletion of a C (arrows). B. cDNA sequencing chromatograms of the heterozygous exon 30 SPG11 mutation in the mother (I:1 same as affected sequence) and two affected siblings (II:1 and II:2) with the insertion of an A (arrow). The mutation is clearly visible in both chromatograms and the peak heights are the same as genomic DNA.

Discussion

In this study, we identified novel compound heterozygous mutations in *SPG11* in a complex HSP family with thin corpus callosum and severe axonal sensory-motor polyneuropathy as a late manifestation of the disease. Moreover they had feet which were oedematous and strikingly blue–black in color as a likely result of fluid dependency and peripheral neuropathy. A recent study by Montecchiani et al. (2016) showed that *SPG11* is the causative gene of a wide spectrum of clinical features, including autosomal recessive CMT2. The severe neuropathy in our case is consistent with neuropathy being a major feature in some, but not all patients with *SPG11* mutations and a complex HSP phenotype as is confirmed in the Cypriot family. An interesting aspect of the two *SPG11* families discussed here is the initial clinical presentation as complex HSP with a later development of an axonal neuropathy clinically and electrophysiologically. As in *SPG11* associated with complex HSP, the variants described by Montecchiani et al. (2016) were scattered throughout the entire DNA sequence, without evidence of ‘hot spots’, and 93 % were truncating mutations. Our findings are consistent with this and other previous studies describing mostly mutations leading to the truncation of the SPG11 protein and consequent loss of function mechanism (Pensato et al., 2014).

In Family 1, based on our cDNA sequencing data, we would expect the protein to be truncated and only little of the mRNA to be targeted for non-sense mediated decay. In our case, one of the truncated forms of the protein is missing the Myb domain (Figure 5-4), and the other one is missing both the Myb and the coil–coil domains whose presence may suggest a role of spatacsin in regulation of gene expression (Liu et al., 2006). In terms of pathology, sural nerve biopsy of SPG11 patients has previously shown loss of unmyelinated nerve fibers and accumulation of intra-axonal pleomorphic membranous material (Hehr et al., 2007). Also, axonal trafficking of vesicles was demonstrated to be impaired in neurons derived from induced pluripotent stem cells of SPG11 patients (Perez-Branguli et al., 2014). Another alteration is in the secretory pathway. Spatacsin has been shown to account for proteins involved in the formation of lysosomes and moreover to interact with components of the AP5 complex involved in membrane sorting of late endosomes (Chang et al., 2014).

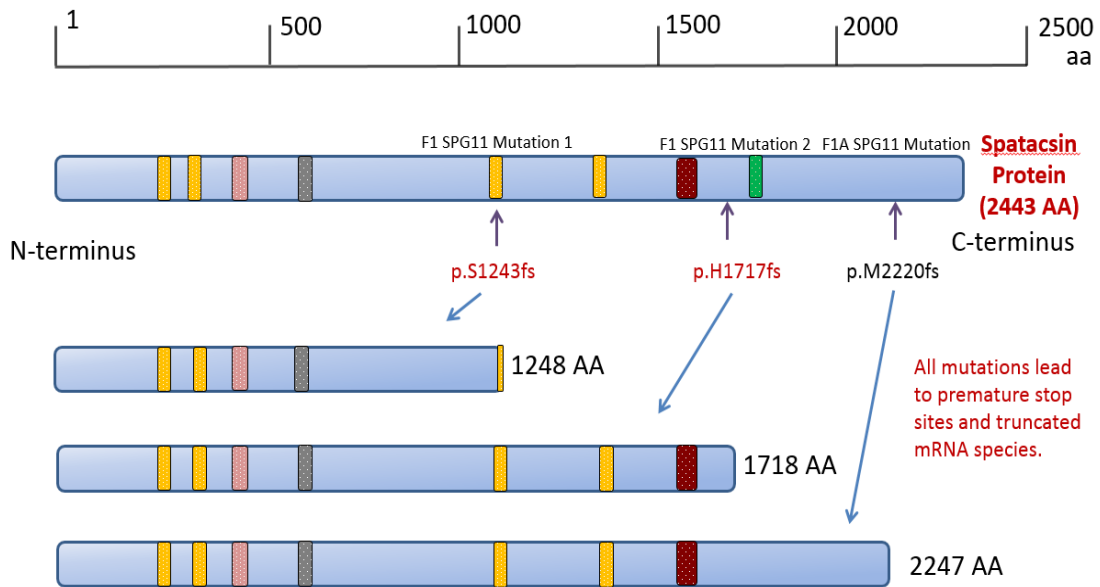


Figure 5-4 Schematic representation of the SPG11 protein.

Mutations that are known are in black and those from this study are in red. Mutation 1 is predicted to truncate the full length protein from 2443 amino acids (AA) to 1248 AA, mutation 2 truncates to 1718 AA and mutation 3 to 2247 AA. Putative functional domains are depicted as rectangles, and their positions within the amino acid sequence are indicated: the transmembrane domain (yellow box; positions, 163–194, 200–240, 1239–1267, and 1471–1493), glycosyl hydroxylase F1 signature (pink box; position, 482–490), leucine zipper (grey box; position, 611–632), coil-coil domain (brown box; position, 1556–1590), and Myb domain (green box; position 1766–1774). Arrows indicate truncating mutations; dotted arrows indicate missense mutations. AA = amino acids.

As our understanding of the hereditary spastic paraplegias increases it is clear that the clinical features are very heterogeneous and the spectrum of signs in disease genes such as *SPG11* can vary substantially. It is noteworthy for clinicians to consider *SPG11* testing in early onset complex HSP or where there is a combination of severe neuropathy and spasticity.

In conclusion, we provide support for the use of whole exome sequencing as a diagnostic tool for identification of mutations in conditions with complex and wide presentations such as HSP. Furthermore, we extend the findings that mutations in *SPG11* are the cause of a spectrum of clinical features including the late manifestation of severe axonal neuropathy.

Chapter 6 *KCNA2* in hereditary spastic paraplegias

Introduction

KCNA2 encodes a member of the potassium channel, voltage-gated, shaker-related subfamily, Kv1.2. The coding region is intronless and the protein contains six membrane-spanning domains, comprising a voltage-sensing (S1–S4) and pore (S5–S6) domain. Homotetrameric Kv1.2 channels form low-threshold, delayed-rectifier Kv channels (Stuhmer et al., 1989) and when coassembled with other Kv1 α -subunits, can generate a diverse array of channel subtypes (Ruppersberg et al., 1990).

Kv1.2 is found in a number of nonsecretory cells, such as vascular (Albarwani et al., 2003) and oesophageal smooth muscle cells (Wade et al., 1999) and cardiac myocytes (Brahmajothi et al., 1996), and it is also present in certain neuronal tissues (Shen et al., 2004). In mammalian brain, Kv1.2 is found prominently along unmyelinated axons and at juxtaparanodes of myelinated axons, but it is also present in the dendrites of some neurons, having an essential role in neuronal excitability and neurotransmitter release (Lai and Jan, 2006). It is expressed in both excitatory and inhibitory neurons (Lorincz and Nusser, 2008).

The physiological importance of Kv1.2 was previously underscored by the finding that Kv1.2 knockout mice have enhanced seizure susceptibility and die in the third postnatal week (Brew et al., 2007) while a missense c.1205T>C (p.Ile402Thr) mutation causes ataxia (Xie et al., 2010).

A recent study identified a recurrent variant in *KCNA2* as a novel cause of HSP in two unrelated families (Helbig et al., 2016). Previously, gain-of-function and dominant-negative mutations in *KCNA2* have been implicated in early-onset epileptic encephalopathies, ataxia, or intellectual disability (Syrbe et al., 2015, Pena and Coimbra, 2015), making this an interesting and unexpected finding, where epilepsy and other neurodegenerative disorders overlap.

In this study we report a *de novo* missense mutation within the Kv1.2 voltage sensor associated with HSP and ataxia. The findings were reported in (Manole et al., 2017b).

Methods

Examination of whole exome sequencing data

The following script was used to query the in-house whole exome database of over 2000 exomes of individuals with inherited neurological disorders:

```
select subjects.subjectid as "subjectid[SID]", * from clinicaldata, subjects,samples,
data,analysis ,coeus.getexonvcf('NM_004974') as exonvcf LEFT JOIN rsnumbers ON
rsnumbers.chrom = exonvcf.chrom and rsnumbers.pos=exonvcf.pos
where analysis.sampleid = data.sampleid and data.sampleid = samples.sampleid and
samples.subjectid = subjects.subjectid and subjects.subjectid = clinicaldata.subjectid
and exonvcf.analysisid = analysis.analysisid
```

From this analysis we identified the same recurrent variant in *KCNA2* found by Helbig et al. (2016) for a *de novo* case with HSP and ataxia.

Sanger sequencing

We next used Sanger sequencing to screen 90 cases with HSP and/or ataxia. PCR primers were designed so that they covered the *KCNA2* gene (NM_004974) and PCR was performed as described in Chapter 3. Primers were:

F1: AATGCTCCTGTGCTTCCTGG; R1: TGATCACCACCCTCTCACAG,
F2:TAGCCCAGTTTCCAGAGACC; R2: TCTCCATCGCTTCTTCTCCC;
F3:AAACATTGCCCATCTTCCGG; R3:GGGATGATGGCCACAATGTC;
F4:GACATTGTGGCCATCATCCC; R4:CCCAATTCTCTCATGCTGGC;
F5:AAGATCCCATCCTCCCCTGA; R5:TCCATTGAGCTGTGAGTACG

Molecular biology

The Arg294His mutations were introduced into the rat Kv1.2 cDNA (in plasmid pAKS2) using a site-directed mutagenesis procedure based on PCR with the proofreading *Pfu* DNA polymerase (Qiagen) [25 cycles of denaturation at 95°C (10 s), annealing at 58°C (5 s) and extension at 68°C (10 min)] followed by the digestion of the PCR reaction with 1 µl (10U/µl) of DpnI at 37°C for 1 h. The DNA sample (100 ng/ µl) was then sent for sequencing in the UCL facility. *In vitro* mRNA synthesis and rigorous quantification were performed as previously described (Chapter 2) (Zerr et al., 1998). Briefly, the mRNA machine (Agilent Technology) was used after the DNA (20-30 ng) was linearized at a unique site with EcoRI (NEB) incubated overnight, then washed with 70% ethanol.

Oocyte injection and electrophysiology

Xenopus oocyte preparation is described in detail in Chapter 2.

Xenopus oocytes were injected with mRNA and incubated at 15°C in MBS containing (in mM): 96 NaCl, 1 KCl, 0.75 CaCl₂, 0.8 MgCl₂ and 10 HEPES (pH 7.4), with 50 U/ml penicillin G and 50 mg/ml streptomycin. Experiments were carried out at room temperature (22–24°C), with continuous superfusion of oocytes with a solution containing (in mM): 96 NaCl, 2 KCl, 1.8 CaCl₂, 1 MgCl₂, 5 HEPES (pH 7.4).

Kv1.2 channel currents were recorded after 24 h with a two-electrode voltage clamp and a GeneClamp 500 amplifier (Axon Instruments, Foster City, CA, USA). Electrodes were filled with 3 M KCl and had resistances between 0.1 and 1 MΩ. Currents were sampled at 5 and 20 kHz and filtered at 1 kHz. For data acquisition and analysis we used Clampex 10.1 and Clampfit 10.1, respectively (Axon Instruments).

Results

We examined whole exome data and performed Sanger sequencing in a cohort of individuals with likely inherited neurological disorders and found one heterozygous *de novo* case with the same mutation described by Helbig et al. (2016) (Figure 6-1). Their third family had a *KCNA2 de novo* mutation, however, had ataxia rather than spasticity at 20 years.

The proband reported here presented as a teenager with progressive walking problems. There was no history of seizures or other neurological features. Clinical examination revealed dysarthria, spastic paraplegia and mild ataxia. The *KCNA2* mutation we identified is a substitution of the first arginine residue in the voltage-sensing S4 segment of Kv1.2 with a histidine residue (c.881G>A, p.R294H).

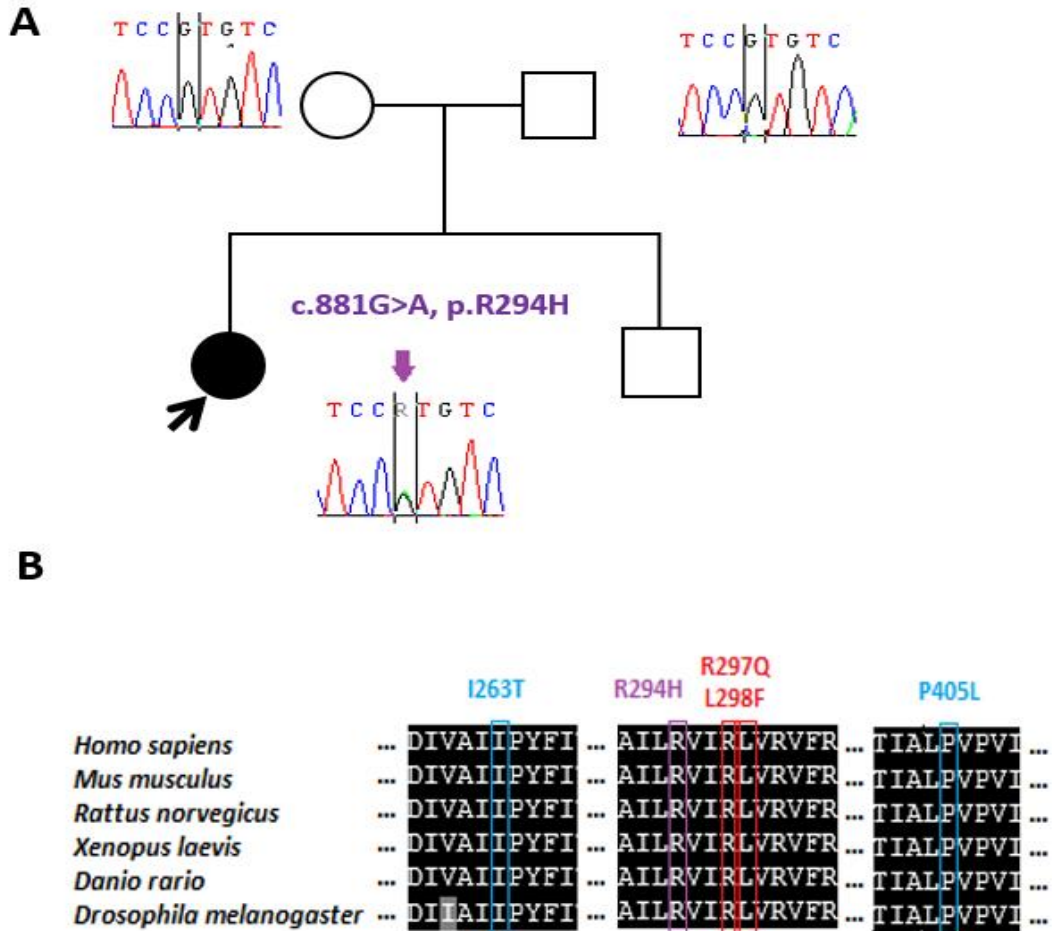


Figure 6-1 KCNA2 family found in this study

A) Pedigree of the *KCNA2* family. Open symbols represent unaffected individuals and filled symbols represent the affected individual. The proband is indicated by an arrow. Sanger sequencing chromatograms surround the symbols and show segregation of mutations. Black bars encompass the sites of interest. B) Structural conservation of the mutated amino acid residues in Kv1.2 across 6 species (single letters = amino acid residues; black = identical; grey = conserved substitution; blue = loss-of-function mutations (Syrbe et al., 2015); red = gain-of-function mutations (Syrbe et al., 2015); purple = mutation found in this study; conservation among species of the affected amino acid residues was determined using Ensembl to retrieve the sequences and ClustalW2 software for multiple sequence alignment.

We performed site-directed mutagenesis on the complementary DNA of *KCNA2*, injected the RNA into *Xenopus laevis* oocytes and recorded currents using two-electrode voltage clamp. The current amplitude of the R294H mutant channel was reduced compared to wild type (I_{\max} (Kv1.2) = $5.7 \pm 0.6 \mu\text{A}$, $n=15$, I_{\max} (R294H) = $2.2 \pm 0.4 \mu\text{A}$, $n=12$, $p < 0.001$, student's t-test) and the voltage dependence of activation was right

shifted ($V_{1/2}$ (Kv1.2) = -19.7 ± 2.1 mV, $n=15$, $V_{1/2}$ (R294H) = -11.2 ± 1.5 mV, $n=12$, $p < 0.01$, student's t-test). Mutation R294H also exerted dominant negative effects when co-expressed with wild type (Figure 6-2).

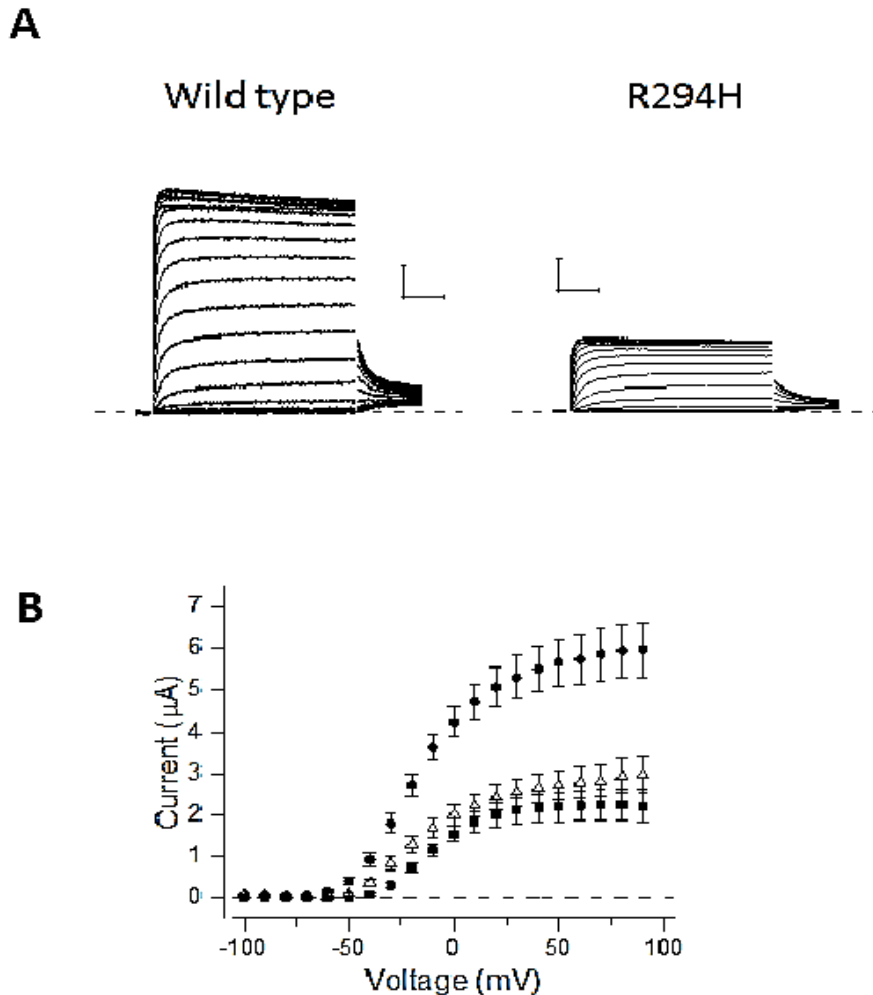


Figure 6-2 Electrophysiology for the Kv1.2 wild-type and mutant channels

A) Representative current traces of wild type and R294H Kv1.2 channels recorded in *Xenopus laevis* oocytes using two electrode voltage clamp. Test voltages ranged from -150 to +90 mV in 10 mV increments, tail voltage was -30 mV. Capacitive transients are not shown. The dashed lines show zero current level. The scale bars are 50 ms and 2 μ A. B) The tail current amplitude is plotted against the test voltage for wild type (solid circles), $n=15$, R294H (solid squares), $n=12$, and wild type/R294H channels (open triangles), $n=16$. Data shows the mean \pm standard error of mean. The dashed lines show zero current level.

Discussion

We have identified a patient with HSP carrying a *de novo* R294H mutation in Kv1.2. Our results confirm that the R294H mutation is pathogenic, exerting a loss of function effect, consistent with published data (Helbig et al., 2016). Other gain of function mutations in the voltage sensor (R297Q and L298F) as well as loss of function mutations outside the voltage sensor (I263T and P405L) have been described before in this channel (Syrbe et al., 2015) (Figure 6-2).

Much of the machinery associated with voltage-gated potassium (Kv) channel activation is localized to a voltage-sensing domain that comprises the transmembrane helices S1-S4, and includes a series of regularly spaced basic (Arg, Lys) residues in the S4 helix, together with acidic (Asp, Glu) residues in S2 and S3 helices (Aggarwal and MacKinnon, 1996).

The highly conserved R294 residue is the first of seven positively charged, the movement of which causes the central Kv1.2 pore to open and allow K⁺ ions to pass through based on their electrochemical gradient (Long et al., 2005). Mutations at these conserved arginine residues have been shown to lead to ion leakage across the membrane and lead to an omega current, which is distinct from the main pore ionic current (Delemotte et al., 2010). Based on homology with the Shaker homologue channel the change to a histidine is predicted to lead to proton conduction at hyperpolarized potentials, a feature which does not occur in wild-type channels (Starace and Bezanilla, 2004). Moreover, it is only this specific substitution at this particular position within the entire channel that is expected to cause such biophysical change.

These findings suggest that the R294H mutation in *KCNA2* results in loss of normal Kv1.2 function and might lead to a proton conduction at hyperpolarized potentials. This may explain the neurodegenerative phenotype associated with the R294H mutation and account for the phenotypic difference in R294H mutation carriers compared to patients with other mutations who have epileptic encephalopathies (Syrbe et al., 2015).

The discovery of *KCNA2* mutations in epilepsy, ataxia and HSP extends the phenotypes that can be associated with this gene but also highlights the clinical importance of the position of the mutated amino acid residue (Kara et al., 2016). Further studies are required to better understand the molecular basis of this novel phenotype and how the specific mutation leads to spastic paraplegia.

Chapter 7 *KCNA1* in episodic ataxia and malignant hyperthermia

Introduction

Episodic ataxia type 1 (EA1) is a rare autosomal dominant neurological disorder and was the first ion channel disease (channelopathy) to be associated with defects in a potassium channel (VanDyke et al., 1975). The disease affects both central and peripheral nerve functions, giving symptomatic attacks of imbalance and uncontrolled movements (Ashizawa et al., 1983). During attacks some individuals may experience vertigo, blurred vision, diplopia, nausea, headache, diaphoresis, clumsiness, stiffening of the body, dysarthric speech and difficulty in breathing (VanDyke et al., 1975). An inability of the motor nerve to repolarise sufficiently between action potentials will give rise to repetitive muscle action potentials and the clinical findings of myokymia (fine twitching of groups of muscles and intermittent cramps and stiffness) and muscle stiffness. In addition, the characteristic interictal myokymia may be detected clinically or may only be apparent by surface or needle electromyography (EMG). The cerebellar attacks may last from seconds to minutes, recurring up to 30 times a day, and might be precipitated by caffeine, hormonal changes, sudden movement, surprise or emotion. The mechanism by which these triggers initiate attacks is largely unknown (Ashizawa et al., 1983). The treatment response is variable, but many families have responded well to either carbamazepine or acetazolamide (Green et al., 2010).

The EA1 locus was mapped to chromosome 12p13 (Browne et al., 1994) and the gene that encodes for the voltage-gated delayed rectifier potassium channel Kv1.1 was later named *KCNA1*. Potassium channels regulate neuromuscular transmission, control the release of δ -aminobutyric acid (GABA) from cerebellar basket cells onto Purkinje cells (Herson et al., 2003), and modulate synaptic transmission in the hippocampus (Geiger and Jonas, 2000). The Kv1.1 channel contains four pore-forming α subunits which each have six transmembrane helices. The N-terminus is associated with β subunits that can modify the inactivation properties of the channel as well as affect expression levels (Kullmann and Hanna, 2002). The C-terminus is complexed to a PDZ domain protein that is responsible for channel targeting (Kullmann and Hanna, 2002). The channels usually occur as heterotetramers in combination with Kv1.2 or Kv1.4 subunits. The Kv1.1 channel is localized in a variety of brain regions including cerebral cortex, bulbus

olfactorius, hippocampus, retina, basal nuclei, thalamus, fiber tracts of the cerebrum and brain stem, and in regions affected in EA1 such as cerebellar nuclei, Purkinje, basket and granular cells of the cerebellum and juxtaparanodal regions of nodes of Ranvier of peripheral nerves (Wang et al., 1993).

Over 30 missense mutations and one truncation mutation in positions highly conserved among the voltage-dependent Kv1 channel superfamily have been reported: one causing hypomagnesemia, three causing myokymia without EA, and the remainder responsible for EA1 with varying associated symptoms and severities (Jen et al., 2007). *In vitro* expression studies indicate that all mutations impair Kv1.1 function. However, the consequences of distinct mutations vary substantially, from small increases in the voltage threshold or time taken for channel activation to complete absence of potassium flux (Eunson et al., 2000, Rea et al., 2002).

The *Kcna1* knockout mouse (*Kcna1*^{-/-}), which lacks Kv1.1 channels, suffers from epileptic seizures but not episodic ataxia (Smart et al., 1998). A knock-in mouse model bearing the human EA1 mutation V408A was created by homologous recombination (Herson et al., 2003) and in contrast to the *Kcna1* null mutation this is embryonic lethal in the homozygous state. However, heterozygous V408A/+ mice exhibit stress-induced loss of motor coordination that is ameliorated by acetazolamide as well as attenuated cerebellar Purkinje signalling, which has been attributed to action potential broadening at basket cell boutons leading to increased GABA release (Herson et al., 2003, Begum et al., 2016). Functional homomeric Kv1.1 channels are tetrameric structures composed of four identical monomers (MacKinnon, 1991) and if wild-type and mutant alleles are expressed, both homomeric and heteromeric channels may be formed. This leads to a difficulty in exploring the effects of the mutations due to a large number of possible channel stoichiometries. Ideally, the mutated channel has to be coexpressed with both its wild-type counterpart (to reproduce the heterozygous situation in affected patients) and with other members of the Kv1 family (mainly Kv1.2 and Kv1.4) and accessory subunits.

Zerr et al. (1998) studied the effects of five Kv1.1 mutations in *Xenopus oocyte*, an expression system that has been successfully used to analyse the electrophysiological properties of cloned potassium channels. The mutation F249I, situated in the first cytoplasmic loop, showed reduced levels of protein and may affect EA1 symptoms by both dominant negative and haplotype insufficiency mechanisms. F249I subunits were

relatively unstable, but intact subunits assembled with wild-type subunits. Therefore, F249I subunits may demonstrate reduced current amplitudes when expressed alone or with wild-type subunits because of a reduction in the number of channels in the membrane as well as possible effects on the single-channel currents.

Prof Grace Yoon from the Hospital for Sick Children, University of Toronto, has found a family presenting with episodic ataxia and malignant hyperthermia (MH), for whom testing of the *CACNA1A*, *CACNA1S*, *SCN1A*, *CACNB4*, *SLC1A3*, *ATPIA2* and *RYR1* genes has been negative. Testing of the *KCNA1* gene revealed a variant of unknown clinical significance c.7468T>G (p.F249C). In this report we describe the electrophysiological consequences of this mutation. The findings were reported in (Mestre et al., 2016).

Methods

Molecular biology

The F249C and Y379V mutations were introduced into the human Kv1.1 cDNA (in plasmid pMT2LF) using a site-directed mutagenesis procedure based on PCR with the proofreading *Pfu* DNA polymerase (Qiagen) [25 cycles of denaturation at 95°C (10 s), annealing at 50°C (5 s) and extension at 60°C (10 min)] followed by the digestion of the PCR reaction with 1 µl (10U/µl) of DpnI at 37°C for 1 h. The DNA sample (100 ng/µl) was then sent for sequencing in the UCL facility. *In vitro* mRNA synthesis and rigorous quantification were performed as previously described (Chapter 2) (Zerr et al., 1998). Briefly, the mRNA machine (Agilent Technology) was used after the DNA (20–30 ng) was linearized at a unique site with NheI (NEB), incubated overnight, then washed with 70% ethanol.

Oocyte injection and electrophysiology

Xenopus oocyte preparation is described in detail in Chapter 2.

Xenopus oocytes were injected with mRNA and incubated at 15°C in MBS containing (in mM): 96 NaCl, 1 KCl, 0.75 CaCl₂, 0.8 MgCl₂ and 10 HEPES (pH 7.4), with 50 U/ml penicillin G and 50 mg/ml streptomycin. Experiments were carried out at room temperature (22–24°C), with continuous superfusion of oocytes with a solution containing (in mM): 96 NaCl, 2 KCl, 1.8 CaCl₂, 1 MgCl₂, 5 HEPES (pH 7.4).

Kv1.1 channel currents were recorded after 24 h with a two-electrode voltage clamp and a GeneClamp 500 amplifier (Axon Instruments, Foster City, CA, USA). Electrodes were filled with 3 M KCl and had resistances between 0.1 and 1 MΩ. Currents were sampled at 5 and 20 kHz and filtered at 1 kHz. For data acquisition and analysis we used Clampex 10.1 and Clampfit 10.1, respectively (Axon Instruments).

Results

For details on the genetic and phenotypic results of this family see (Mestre et al., 2016). All family members with symptoms consistent with episodic ataxia carried the c.746T>G (p.Phe249Cys) mutation (Figure 7-1). The mutation also segregated with family members who had a confirmed diagnosis of MH susceptibility.

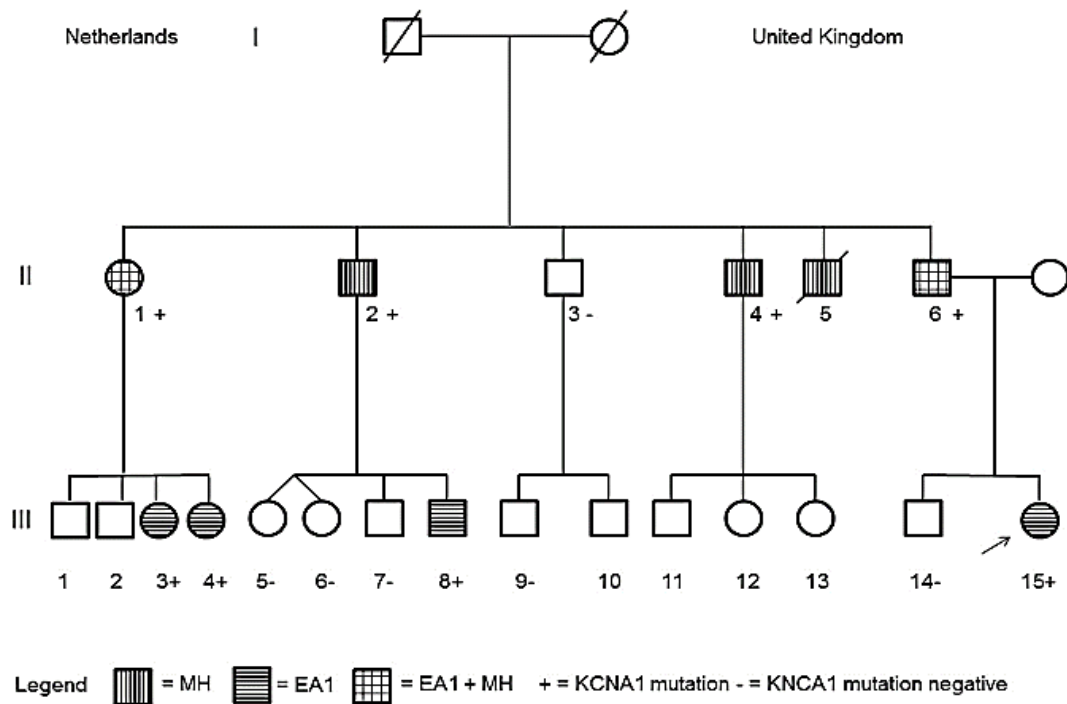


Figure 7-1 *KCNA1* family pedigree.

Horizontal bars denote individuals with EA1. Vertical bars denote individuals with MH. Phe249Cys *KCNA1* mutation status is indicated as plus sign or minus sign. Modified from (Mestre et al., 2016).

To determine the functional consequences of the EA1 mutation, equal amounts of wild-type and F249C mRNAs were injected separately and together with varying stoichiometry into *Xenopus* oocytes, and currents were examined in the two-electrode voltage-clamp configuration. The oocytes expressing F249C had virtually no current

amplitudes measured at 40 mV compared with oocytes expressing wild-type subunits (Figure 7-2). Other methods of obtaining higher levels of expression were tested either by injecting more mRNA or by waiting longer after injection, but currents were still not detected. F249I has previously been reported as not forming functional channels (Adelman, 1995). To check for the possibility of assembly between the F249C and wild-type (according to a binomial distribution (MacKinnon, 1991) or just forming homomeric EA and wild-type channels), equal amounts of F249C to wild-type mRNAs were coinjected. Compared with currents recorded from oocytes injected with the same total amount of mRNA for wild type only (homozygous wild-type condition), the current amplitudes were reduced in oocytes coinjected with half wild-type mRNA and half mRNA for F249C mutant.

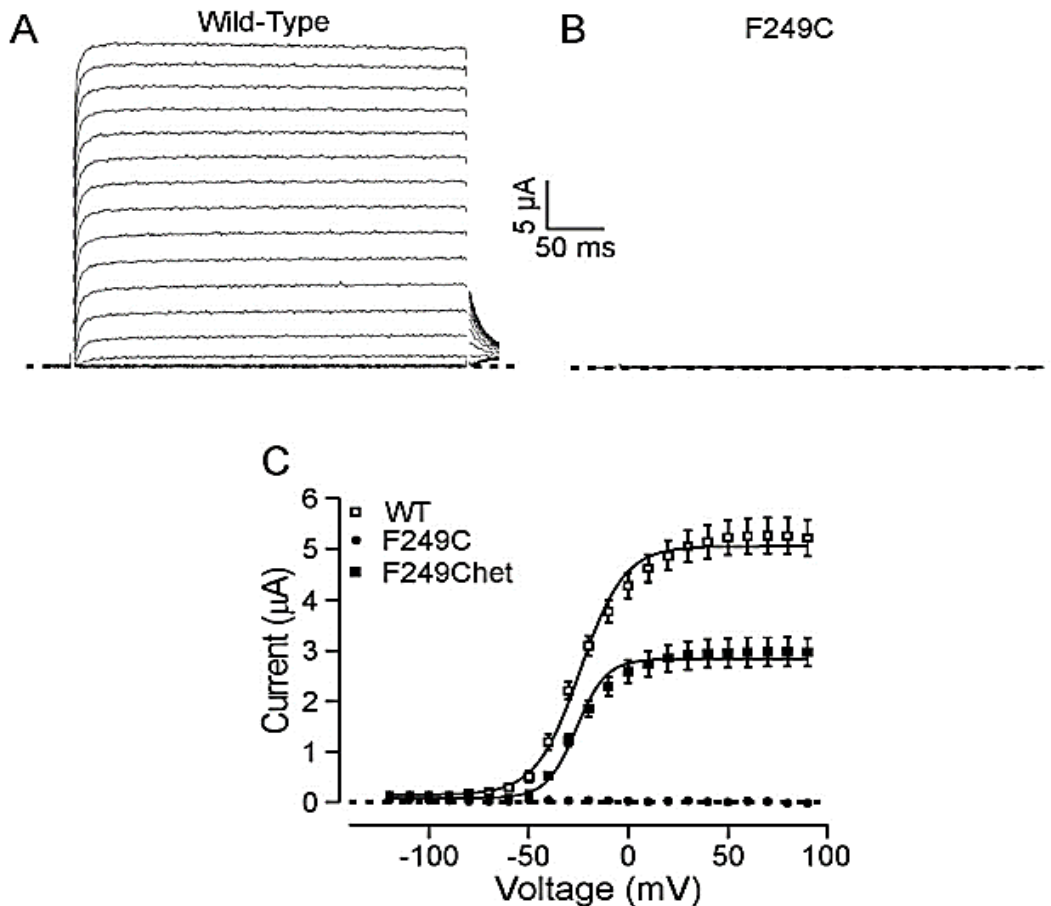


Figure 7-2 Electrophysiological characterization of Phe249Cys mutant

Electrophysiological characterization of Phe249Cys mutant channels. K^+ currents after expression of the A) wild-type (WT) channels or of the B) Phe249Cys channels on *Xenopus laevis* oocytes. Capacitive transients at beginning of the voltage steps are not shown. C) Current–voltage relationship of WT (n= 27), Phe249Cys (F249C, n=12), and heterozygous Phe249Cys channels (F249Chet, n=23). Solid lines show fit of Boltzman equation to the mean data.

Comparison of current recordings of coexpression of mutant F249C obtained at a test pulse potential of 20 mV and a tail potential of -50 mV demonstrated kinetics that were similar to those of homomeric wild-type channels (Table 7-1). The data obtained follows a Boltzmannian distribution and can be fitted according to the equation (1):

$$(1) \quad f(V) = \frac{I_{max}}{1 + e^{(V_{mid} - V)/V_c}} + C$$

where V_{mid} is the potential of half-activation, and V_c is a slope factor.

Table 7-1 Characterization of currents from oocytes coexpressing subunits.

Voltage-dependent parameters of activation (V_{mid} and V_c) were obtained from the Boltzmann equation described in Equation 1. Time constant for activation at 20 mV (τ_{fast}) and deactivation at -40 mV were determined from exponential fits (n=12).

	Voltage-dependent parameters				Activation		Deactivation	
	V_{mid}	S.E	V_c	S.E	τ_{fast} (msec)	S.E.	τ (msec)	S.E
Wild type (WT)	-23.9	0.98	13.3	0.81	1.65	0.34	12.2	0.87
WT_F249C_1:1	-25.9	0.64	9.5	0.17	2.06	0.46	11.0	0.67
WT_F249C_1:4	-25.6	1.53	8.7	1.36	4.00	0.11	13.8	0.33

Pharmacological response

The Kv1.1 channel contains a tyrosine residue within the P loop that endows homomeric channels with high sensitivity to TEA ($K_i = 0.2\text{--}0.4$ mM). Substitution of a valine at this position has been shown to reduce sensitivity to TEA by 100-fold (MacKinnon and Yellen, 1990). In oocytes coexpressing TEA insensitive (TEA-tagged) and TEA-sensitive subunits, the dose response to TEA reflects the number of tyrosine containing subunits within the channel.

To test if the p.Phe249Cys subunits could form heterotetramers with WT subunits, we made the p.Phe249Cys channel insensitive to TEA block. Both the wild type and the F249C mutant were altered in their sensitivity to external TEA (TEA-tagged). When co-expressed together with WT subunits in a 1:1 ratio, the sensitivity of WT/Phe249Cys-Tyr379Val channels was reduced ($p < 0.001$) (Figure 7-3).

The data points for wild type and for wild type and TEA tagged F249C were fitted with a single binding isotherm giving K_i values of 0.4 mM and 3 mM respectively. The TEA tagged wild type and hybrid wild type were less than 50% inhibited and thus a value for the K_i is not quoted. This reduction in TEA-sensitivity was much smaller than when the WT channels were co-expressed with WT subunits made insensitive to TEA block (Figure 7-3). To test if the co-expression of p.Phe249Cys may negatively influence the function of the WT subunits, we injected an increasing amount of Phe249Cys mRNA at a constant amount of WT mRNA. As the concentration of p.Phe249Cys mRNA increased, the current amplitude decreased (Figure 7-4).

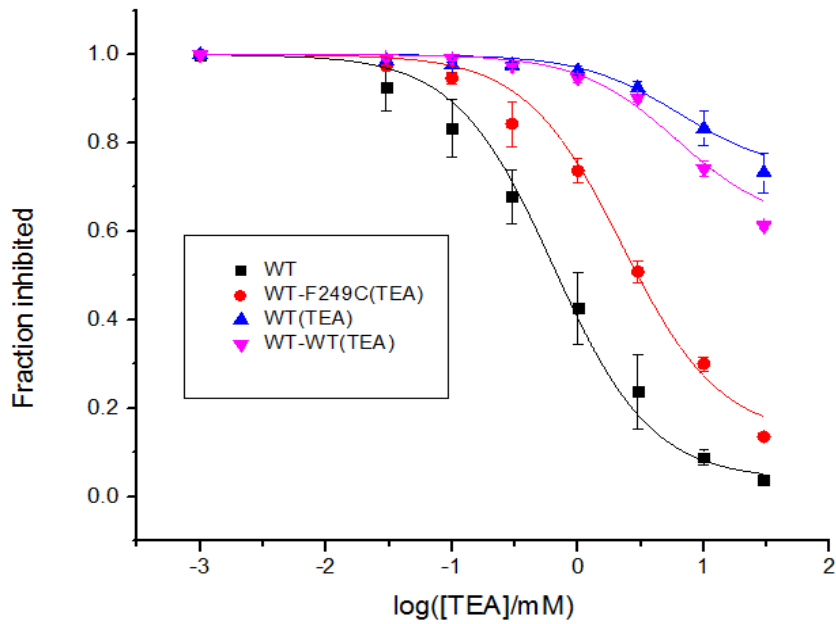


Figure 7-3 Mean TEA dose–response data.

Mean TEA dose–response data for *Xenopus laevis* oocytes injected with WT ($n = 10$), TEA insensitive WT (WT-TEA, $n = 4$), a 1:1 mix of WT and WT-TEA ($n = 8$), or a 1:1 mix of WT and TEA insensitive Phe249Cys mRNA (F249C-TEA, $n = 6$). Solid lines show fit of equation $I = Ki/([TEA] + Ki)$ to the mean data.

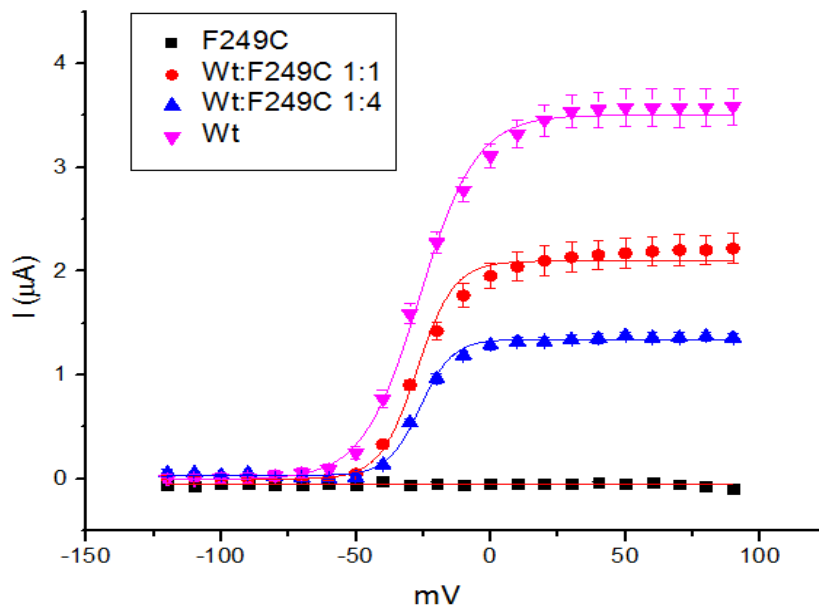


Figure 7-4 Mean current–voltage data

Mean current–voltage data for *Xenopus laevis* oocytes injected with 50 ng WT mRNA (WT, $n = 22$), 50 ng WT and 50 ng Phe249Cys mRNA (WT + F249C, $n = 23$), or 50 ng WT and 200 ng Phe249Cys mRNA (WT + F249C*4, $n = 17$). Solid lines show fit of Boltzman equation to the mean data.

Discussion

We report a novel c.746T>G (p.Phe249Cys) mutation of *KCNA1* co-segregating in a two-generation family clinically diagnosed with EA or myokymia and MH susceptibility. The Phe249 amino acid residue is located in the intracellular loop between transmembrane segments TM1 and TM2 within the voltage-sensing domain of the Kv1.1 channel. It is highly conserved across species indicating that the phenylalanine at position 249 is essential for normal channel function. The mutant F249C is non-functional, but the mutant coassembles with wild-type subunits without changing its voltage dependence and kinetic properties. Coexpression with the wild-type channel leads to reduced levels of protein (less than 50% when mixed in a 1:1 ratio) suggesting that, similarly to F249I mutation (Zerr et al., 1998), F249C leads to EA1 symptoms by both dominant negative and haplotype insufficiency mechanisms. In addition, the electrophysiology data suggests that the mutant subunit can co-assemble with the WT subunits and may reduce the functional expression of the heterotetramer in the cell surface. Of interest, in all family members in whom MH susceptibility was documented, the p.Phe249Cys mutation segregated very well.

Malignant hyperthermia results most often from exposure to potent inhalation anesthetics such as succinylcholine, but also from environmental temperature, mitigating drugs administered simultaneously, and a degree of stress (McCarthy et al., 2000). The pathophysiologic changes are due to uncontrolled rise of myoplasmic calcium, which activates biochemical processes related to muscle activation: enhanced intracellular calcium, oxygen consumption, carbon dioxide production, ATP breakdown and heat generation (Merritt et al., 2017). Presumably, the declining levels of ATP lead to failure of membrane integrity and release of potassium and creatine kinase, although the exact steps in the process have not been definitively demonstrated (McCarthy et al., 2000). In most cases the syndrome is caused by a defect in the ryanodine receptor (RYR). Over 90 mutations have been identified in the RYR-1 gene located on chromosome 19q13.1, and at least 25 are causal for malignant hyperthermia (Merritt et al., 2017). The channel is closely associated with other proteins and structures such as the dihydropyridine calcium channel located at the plasma membrane, which mediates transfer of voltage change to the RYR1 receptor. This association is responsible for coupling the depolarization at the plasma membrane with the activation of the RYR1

receptor and the concomitant release of calcium from the sarcoplasmic reticulum (Merritt et al., 2017).

In subject II-6, genetic testing of *RYR1* and *CACNA1S* followed by exome sequencing was negative. These findings raise an important question regarding a potential contribution of the p.Phe249Cys *KCNA1* mutation to MH in this family. The fatal MH event in subject II-5 may have been caused by functionally impaired Kv1.1 channels precipitated by exposure to anesthesia. Volatile anesthetics are known to have an inhibitory effect on Kv1.1 channels (Friederich et al., 2001), and *KCNA1* knock-out mice have muscle hyperexcitability (Zhou et al., 1998). The effect of volatile anesthetics on a mutated channel with reduced current could lead to increase in excitability of the peripheral nervous system, which expresses Kv1.1 channels, and secondarily maintain cardiac and skeletal muscle contraction with dysregulation of Ca²⁺ homeostasis. Loss-of-function mutation in Kv1.1 channels may potentially induce a thermoregulatory defect in hypothalamic neurons that mediate rapid core body temperature changes (D'Adamo et al., 2014), as seen in MH. We postulate that the p.Phe249Cys *KCNA1* mutation could have precipitated the MH event in this family.

In conclusion, we report a novel *KCNA1* mutation associated with an EA1 phenotype and a possible association with MH. The current report broadens the phenotypes associated with *KCNA1* mutations to include possible susceptibility to MH. Further investigations are required to establish how the F249C mutant Kv1.1 channel might affect the depolarization at the plasma membrane and subsequently calcium release.

Chapter 8 Modelling of episodic ataxia 1 with iPSC-derived neurons

Introduction

Embryonic stem cells (ESCs) and induced pluripotent stem cells (iPSCs) are currently being used to generate *in vitro* disease models as well as large populations of healthy neurons to explore the therapeutic potential of transplantation (Santostefano et al., 2015, Shi et al., 2012). The main advantages of patient-specific iPSC are that the effects of patient-relevant mutations can be studied in the correct genetic and cellular background and also that they avert the needs of immune suppressors in cells-based therapy. The most efficient neural induction of iPSCs is thought to be using the dual inhibition of the SMAD signalling pathway (Chambers et al., 2009). This involves the synergistic inhibition of the BMP and TGF β pathways to attain rapid and uniform neural conversion of pluripotent cells. The newly formed fetal human neural precursors may then be patterned into neuronal cell types with the wanted regional identities using combinations of morphogens, small molecules, growth factors and transcription factors (Chambers et al., 2009). In this study additional overexpression of one of the basic helix-loop-helix (bHLH) proneural proteins, Neurogenin 2 (Ngn2) was also performed. This is a master regulator of the neurogenic machinery and is critical for specification of cortical neuron fate (Britz et al., 2006). Ngn2 (encoded by *Neurog2*) is expressed in the late G1 phase nuclei and is excluded from the G2/M phase nuclei. Overexpression of Ngn2 in mouse spinal cord precursors promotes cell cycle exit by rapidly downregulating a subset of cyclins that act at the G1–S phase transition of the cell cycle (Britz et al., 2006). Human iPSCs have also been converted into neurons by forced expression of Ngn2, which generates a homogenous population of glutamatergic excitatory neurons with abundant synapse formation (Britz et al., 2006). For the purpose of this study biopsies from several EA1 families with different Kv1.1 mutations were taken. One family (affected mother and daughter) harbours the C185W mutation, previously characterized in HEK cells (Tomlinson et al., 2013). No potassium currents were observed upon its expression but also no intracellular aggregates were detected, confirming that the C185W mutants were not being retained in the cytoplasm. More recently this mutation has in addition been associated with markedly atypical symptoms, including long-lasting attacks of jerking muscle contractions associated with hyperthermia, severe migraine, and a relatively short-sleep phenotype (D'Adamo et al., 2014). Another biopsy case has the T226R

mutation, which is associated with a form of EA1 that is complicated by contractures and epilepsy (Zuberi et al., 1999). It was reported that this mutation would exert a dominant negative effect on the wild-type allele and more recently that it markedly enhanced the release of neurotransmitter in transduced rat hippocampal neurons (Heeroma et al., 2009). However the interpretation of the data was made difficult by the likelihood of an overexpressed Kv1.1 compared to the native channels.

To determine the neuronal consequences of the Kv1.1 mutation in the work reported here, somatic cell reprogramming (Okita et al., 2011, Takahashi and Yamanaka, 2006) was used to generate iPSCs from individuals with EA1. The iPSC lines were then differentiated into neurons using conditions that favour the generation of cortical neurons.

Methods

Ethics approval and consent

This study was granted ethical approval by the National Research Ethics Service Committee of the NHNN (UCLH REC number 99/N103). Written informed consent to perform a skin biopsy and fibroblasts were obtained from all patients and/or parental guardians. The control fibroblast lines were provided by the BioBank.

Cell culture and reprogramming to induced pluripotent state

Fibroblasts were cultured in conditions as described in Chapter 2 in DMEM supplemented with 10% FBS. Reprogramming for 3 age matched control and 3 patient lines was achieved using nucleofection (program U20) with 3 µg of episomal plasmids (pCLXE-hOct3/4-shp53, pCLXE- hSox2-Klf4, pCLXE- hLmyc-Lin2) that were electroporated into 3.6×10^5 fibroblasts with a Amaxa™ Basic Nucleofector™ for Primary Mammalian Fibroblasts (Okita et al., 2011). Conditions used for electroporation were 1650 V, 10 ms width, and 3 pulses. Six days post-nucleofection, fibroblasts were re-plated in 10 cm dishes and 6-well plates. After ~2 weeks putative iPSC colonies were identified and were manually picked and transferred onto Geltrex (Gibco) coated plates. A number of iPSC lines derived from each donor with stable and typical hESC-like morphology were then expanded in Essential 8™ Medium with 0.5 mM EDTA splits (detailed in Chapter 2).

RT-PCR for checking for integration of episomal plasmids

RNA from passage 10 iPSCs was extracted using TRIzol, as per manufacturer's instructions. The concentration and purity of RNA was determined spectrophotometrically. 1 µg of RNA was used for a DNase I reaction and reverse transcribed to first strand cDNA by using random primers and M-MLV as described in Chapter 3. Primers used to check for the presence of the backbone of the episomal plasmid were: EBNA-1_Forward: ATC AGG GCC AAG ACA TAG AGA TG and EBNA-1_Reverse: GCC AAT GCA ACT TGG ACG TT. GoTaq® Green Master Mix was used and the PCRs were performed with the following protocol: 95°C-2 min, (95°C-30 s, 60°C-30 s, 72°C-1 min) X 40, 72°C-5 min, and 4°C-hold. A positive control (integrated clone) was provided by Dr Charlie Arber.

Karyotyping of iPSCs

iPSCs were prepared as live cells in T25 flasks and sent to TDL Genetics, The Doctors Laboratory, London for karyotyping.

DNA extraction and Sanger sequencing of *KCNA1* mutations in iPSCs

Genomic DNA was extracted from cells with DNeasy (Qiagen) according to the manufacturer's instructions. PCR and Sanger sequencing for the *KCNA1* gene were performed as described in Chapter 2. Primers used were:

F1:CTGGTCCCTGGCTGCTTC; R1:CTCAGGGGGTCTGAAGTAGC;
F2:TCGAGACGCAGCTCAAGAC; R2:GGCGCTGGTACTCCTTCTC;
F3:GTGCCCTGGACATGTTCTC; R3:TGAAGAAGTCCGTCTTGCTG;
F4:CCCTTCTTCATCGTGGAAAC; R4:CGATCTTGCCTCCAATTGTC;
F5:AAGCTGAGTCGCACTTCTCC; R5:AGCTGCTAAGTGGGGCTTTT

Standard lentivirus production and concentration procedure

The Tet-O-Ngn-t2a-GFP-Blasticidin and rtTA plasmids was kindly provided by Prof Vania Broccoli together with the lentivirus helper plasmids, pRSV-Rev, VSVG and pMDL. For lentivirus production, plasmids were prepared using the Endofree Plasmid Maxi kit (Qiagen) according to manufacturer's protocol after transformation into Stbl3™ cells (Invitrogen). Production of 3rd generation lentivirus was performed using the combined ratio of Tet-O-Ngn-t2a-GFP-Blasticidin/rtTA, pMDL, VSVG and pRSV-Rev plasmid at 4:2:1:1, respectively. Lipofectamine 2000 (Invitrogen) reagents were

used and 80 µg of mixed DNA plasmid was transfected into 293T HEK cells according to the manufacturer's protocol. 24 h post-transfection, the viral supernatant was harvested and replaced with DMEM supplemented with 10% FBS and incubated at 5% CO₂ prior to the second collection of viral supernatant. A second collection was made after a further 30 h. The conditioned medium from the two harvests was combined and passed through a 0.45 µm pore PVDF Millex-HV filter (Millipore). Filtered supernatant was then added to 36 mL polylallylmer conical tubes and ultracentrifuged at 20,000 g for 2 h. Virus pellets were resuspended in dPBS, aliquoted, and snap-frozen in liquid N₂.

Cortical neuronal differentiation

To start with, iPSCs were differentiated into cortical neurons using the Livesey protocol with some modifications (Shi et al., 2012). In brief, iPSCs were cultured in an adherent monolayer on Geltrex-coated plates. Neural induction was achieved using dual SMAD inhibition (1 µM dorsomorphin and 10 µM SB431542) in neural maintenance media (DMEM/F-12, neurobasal, N-2, B-27, 5 µg/ml insulin, 1 mM L-glutamine, 100 µM non-essential amino acids, 100 µM 2-mercaptoethanol, 50 units/ml penicillin and 50 mg/ml streptomycin). After the formation of a neuroepithelial sheet, cells were passaged with Dispase II (Sigma) as small clusters onto wells coated with laminin. The subsequent differentiating cells were allowed to form neural rosettes in the presence of b-FGF and passaged until confluent and then frozen as cortical neural progenitor stocks. RT-qPCR and immunofluorescence microscopy confirmed the adoption of cortical identity. Neuronal age was reckoned from the day of neural induction. At ~ day 35, NPC were differentiated to neurons using forced expression of Ngn2 as previously described (Zhang et al., 2013). Briefly, NPCs were plated on matrigel- (BD Biosciences) -coated coverslips in neural maintenance media with StemPro® Accutase®. On day -1, lentivirus prepared as described above (0.83 µl/well of 24 well plate) was added in fresh neural maintenance media. On day 0, the culture medium was replaced with Neurobasal-A media (Invitrogen) containing human BDNF (10 µg/l, PeproTech). Doxycycline (2 mg/l, Clontech) was added on day 0 to induce Tet-O gene expression, and retained in the medium until the end of the experiment. On day 1, a 48 h blasticidin (Invivogen, 30 µg/ml) and hygromycin (Invivogen, 30 µg/ml) selection period was started. After day 2, 50% of the medium in each well was exchanged every 2 days. Neurons were assessed between 3 and 4 weeks in culture.

Generation of iN cells from human iPSCs

iPSCs were treated with Accutase (Innovative Cell Technologies) and plated as dissociated cells in 24 well plates (1.5×10^4 cells/well) on day -2. Cells were plated on matrigel- (BD Biosciences) -coated coverslips in mTeSR™1 containing 2 μ M thiazovivin (Bio Vision). On day -1, lentiviruses prepared as described above (0.83 μ l/well of 24 well plate) were added (1:1 ratio) in fresh mTeSR™1 medium. On day 0, the culture medium was replaced with N2/DMEM/F12/NEAA (Invitrogen) containing human BDNF (10 μ g/l, PeproTech), and mouse laminin (0.2 mg/l, Invitrogen). Doxycycline (2 g/l, Clontech) was added on day 0 to induce TetO gene expression, and retained in the medium until the end of the experiment. On day 1, a 48 h blasticidin (Invivogen, 30 μ g/ml) and hygromycin (Invivogen, 30 μ g/ml) selection period was started. On day 2, mouse neurons (isolated from P0–P1 mouse pups, see Chapter 2 for method) were added in Neurobasal medium supplemented with B27/Glutamax (Invitrogen). After day 2, 50% of the medium in each well was exchanged every 2 days. iN cells were assayed between 3 and 4 weeks in culture in most experiments.

qPCR for pluripotency and neural markers

RNA was extracted and reverse transcribed as described above. qPCR was performed using Fast SYBR Green Master Mix (Applied Biosystems) and run on a ViiA 7 System (Applied Biosystems). Samples were assayed with 3 technical replicates. Data was analyzed using the $2^{-\Delta\Delta C_t}$ method and expression was normalized to GAPDH/PBDG expression (Livak and Schmittgen, 2001). Primers are listed in Table 8-1.

Table 8-1 qPCR primer sequences for pluripotency and neural markers

Pluripotency markers		Neural markers	
OCT3/4 F	CCC CAG GGC CCC ATT TTG GTA CC	OTX2 F	TGCCAAAAAGAAGACATCTCCA
OCT3/4 R	ACC TCAGTT TGA ATG CAT GGG AGA GC	OTX2 R	AAGCTGGGCTCCAGATAGACAC
KLF4 F	ACC CAT CCT TCC TGC CCG ATC AGA	NESTIN F	AGCAGGAGAAACAGGGCCTAC
KLF4 R	TTG GTAATG GAG CGG CGG GAC TTG	NESTIN R	CTCTGGGGTCTTAGGGAATTG
SOX2 F	TTC ACA TGT CCC AGC ACT ACC AGA	SOX1 F	GGAAGGTCATGTCCGAGGCC
SOX2 R	TCA CATGTG TGA GAG GGG CAG TGT GC	SOX1 R	ACTTGTCTTCTTGAGCAGCG
NEUROG2 F	TCAAGAAGACCCGTAGACTGAAGG	NEUROG2 R F	AACTCCACGTCCCCATACAG
NEUROG2 R	GTGAGTGCCAGATGTAGTTG	NEUROG2 R R	GAGGTGCATAACGGTGCTTCT
GAPDH F	ACC ACA GTC CAT GCC ATC AC	FOXA2 F	ATT GCT GGT CGT TTG TTG TG
GAPDH R	TCC ACCACC CTG TTG CTG TA	FOXA2 R	TGT ACG TGT TCA TGC CGT TC
Myc F	CTGAAGAGGACTTGTTCGCGAAAC	Pax6 F	AACAGACACAGCCCTCACAAACA
Myc R	TCTCAAGACTCAGCCAAGGTTGTG	Pax6 R	CGGGAAGTTGAACTGGAAGTGC
KLF4 F	GGTCGGACCACCTCGCCTT ACAC	GFAP F	CTGCGGCTCGATCAACTCA
KLF4 R	CTCAGTTGGGAAGTTGACCA	GFAP R	TCCAGCGACTCAATCTTCCTC
DNMT3B F	ATAAGTCGAAGGTGCGTCGT	Atp5h F	GCTGGGCGAAAAGTTGCTCTA
DNMT3B R	GGCAACA TCTGAAGCCA TTT	Atp5h R	CCAGTCGATAGCTGGTGGATT
Rex1 F	CCGAGACCACGTCTGTGCGG	KCNA1 HF	TAGTGCAGTGTACTTTGCCGA
Rex1 R	AGCGCTTTCCGCACCCTTCA	KCNA1 HR	GTCACCGTATCCTACAGTGGT
PBDG F	GGAGCCATGTCTGGTAACGG	KCNA1 RF	TAGTGCAGTGTACTTTGCCGA
PBDG R	CCACGCGAA TCACTCTCA TCT	KCNA1 R	GTCACCGTATCCCACAGTGGT

Immunofluorescence

In order to detect pluripotency or neural markers, cells were fixed with 4% paraformaldehyde for 15 min at room temperature (25 °C), rinsed three times with phosphate-buffered saline (PBS) and stored at 4 °C before analysis. Cells were permeabilised with 0.1% Triton X-100 in PBS (PBST) for 10 min, and then incubated in 5% BSA/PBST at room temperature for 30 min. All primary antibodies were diluted in 5% BSA/PBST and incubated with cells at 4 °C in a humidified chamber for 12–16 h. Corresponding secondary antibodies in 5% BSA/PBST were then added and incubated for 1 h at room temperature. Cells were then washed once with DAPI (1 µg/mL) in PBST for 10 min and twice with PBST for 5 min. Primary antibodies and the dilutions used are listed in Table 8-2.

Table 8-2 Primary antibodies used in this study and their details.

Primary Ab	Clonality/ Animal source	Dilution	Supplier/Catalogue Number
Pluripotency			
hNanog	Poly IgG Goat	1:100	R&D AF1997
hSox2	Poly IgG Goat	1:200	R&D AF2018
hTRA-1-60	Mono IgM Mouse	1:100	Santa Cruz sc-21705
hOct-3/4 (C-10)	Mono IgG Mouse	1:100	Santa Cruz sc-5279
Endoderm			
hGATA-4	Mono IgG Mouse	1:100	Santa Cruz sc-25310
FoxA2/hHNF3b	Poly IgG Goat	1:100	R&D AF2400
hSox17	Poly IgG Goat	1:200	R&D AF1924
Mesoderm			
hBrachyury	Poly IgG Goat	1:100	R&D AF2085
hEomes	Poly IgG Rabbit	1:600	Abcam ab23345
Neuroectoderm			
Nestin	Mono IgG Mouse	1:100	Abcam ab22035
hSox1	Poly IgG Goat	1:100	R&D AF3369
hPax6	Poly IgG Rabbit	1:100	Covance
Neural Differentiation			
hSox2	Poly IgG Goat	1:200	R&D AF2018
Nestin	Mono IgG Mouse	1:100	Abcam ab22035
hSox1	Poly IgG Goat	1:100	R&D AF3369
hPax6	Poly IgG Rabbit	1:100	Covance
GFAP	Chicken polyclonal to GFAP	1:600	Abcam ab4674
Foxg1	Poly IgG Rabbit	1:300	Abcam ab18259
Otx1	Mono IgG Mouse	1:300	Merkmillipore MAB5602
Tbr1	Poly IgG Rabbit	1:300	ABCAM ab31940

Immunofluorescence panNav

In order to detect mouse anti-PanNav clone K58/35 (1:50, Sigma-Aldrich, catalog number S8809), cells were fixed with 4% PFA for 15 min at room temperature (25°C), rinsed three times with phosphate-buffered saline (PBS) and stored at 4 °C before analysis. On retrieval, cells were washed 3 times in 50 mM NH₄Cl before incubation for 5 min in 50 mM NH₄Cl. Cells were then permeabilised for 10 min in PBST and incubated in 5% BSA/PBST at room temperature for 35 min. All primary antibodies were diluted in 5% BSA/PBST and incubated with cells at 4 °C in a humidified chamber for 12–16 h. Typically mouse anti-PanNav was used with rabbit anti-β3-tubulin (1:300) and chicken anti-GFP (1:500). Cells were washed twice in 5% BSA/PBST, then incubated for 10 min in PBST. Corresponding secondary antibodies in 5% BSA/PBST were then added and incubation performed for 1 h at room temperature. Cells were then incubated for 10 min in 5% BSA/PBST, washed in 5% BSA/PBST, followed by PBS, then incubated with DAPI (1 µg/mL) in PBS for 10 min.

Electrophysiological recordings

All recordings were conducted at 25°C, 20–30 days after plating. The patch pipette solution contained: 125 mM K-gluconate, 10 mM NaCl, 4.6 mM MgCl₂, 4 mM Na₂-ATP, 15 mM creatine phosphate, 1 mM EGTA and 20 U/ml phosphocreatine kinase (pH 7.3). The standard extracellular solution used in all experiments contained 125 mM NaCl, 2.5 mM KCl, 2 mM MgCl₂, 2 mM CaCl₂, 30 mM glucose, 0.01 mM NBQX, 0.05 mM APV, and 25 mM HEPES (pH 7.4). Patch pipettes had a resistance of 3-5 MΩ in current clamp. After membrane rupture, cells were held at -70 mV. Currents were recorded using an Axopatch 700B amplifier (Molecular Devices). Data were acquired and analysed using LabView software (V.10.0, National Instruments) with in-house acquisition programs (DMK). Data were sampled at 20 kHz and filtered at 5 kHz. Graphs were plotted using Origin (V.9.0). The liquid junction potential for K-gluconate was calculated to be 14.6 mV with Clampex Junction Potential calculator but was not corrected for.

Results

Generation and validation of the iPSCs lines

To determine the neuronal consequences of the Kv1.1 mutation, we used somatic cell reprogramming to generate induced pluripotent stem cells from skin fibroblasts of patients with EA1. A total of 12 stable clones for the corresponding 6 lines were produced (Table 8-3). All lines could be maintained in culture for at least 30 passages without loss of pluripotency or self-renewal capability using standard iPSC culture conditions, both in feeder-free conditions and on mouse embryonic fibroblast (MEF) feeder cells. The genomes of all our lines appeared to be cytogenetically stable; all exhibited normal karyotypes after reprogramming and more than 15 passages in culture, ruling out the presence of gross chromosomal abnormalities. In addition all the lines used in this study were tested for the presence of an integrated episomal plasmid after passage 8. No traces of genomic integration or residual episomal plasmid retention were observed (Figure 8-1).

Table 8-3 Characterization of iPSC generated in this study

iPS ID	Age at biopsy (years)	Gender	Mutation	Integration	Karyotype
CKJ2F	16	F	c.555C>G, p.C185W	No	Normal
CKJ3G				No	Normal
SP2i	36	F	c.555C>G, p.C185W	No	Normal
SP2j				No	Normal
Das2D	45	F	c.677C>G, p.T226R	No	Normal
Das13E				No	Normal
73E38	20	F	Normal control	No	Normal
73O41				No	Normal
151B	44	M	Normal control	No	Normal
152E				No	Normal
624A	38	M	Normal control	No	Normal
626C				No	Normal

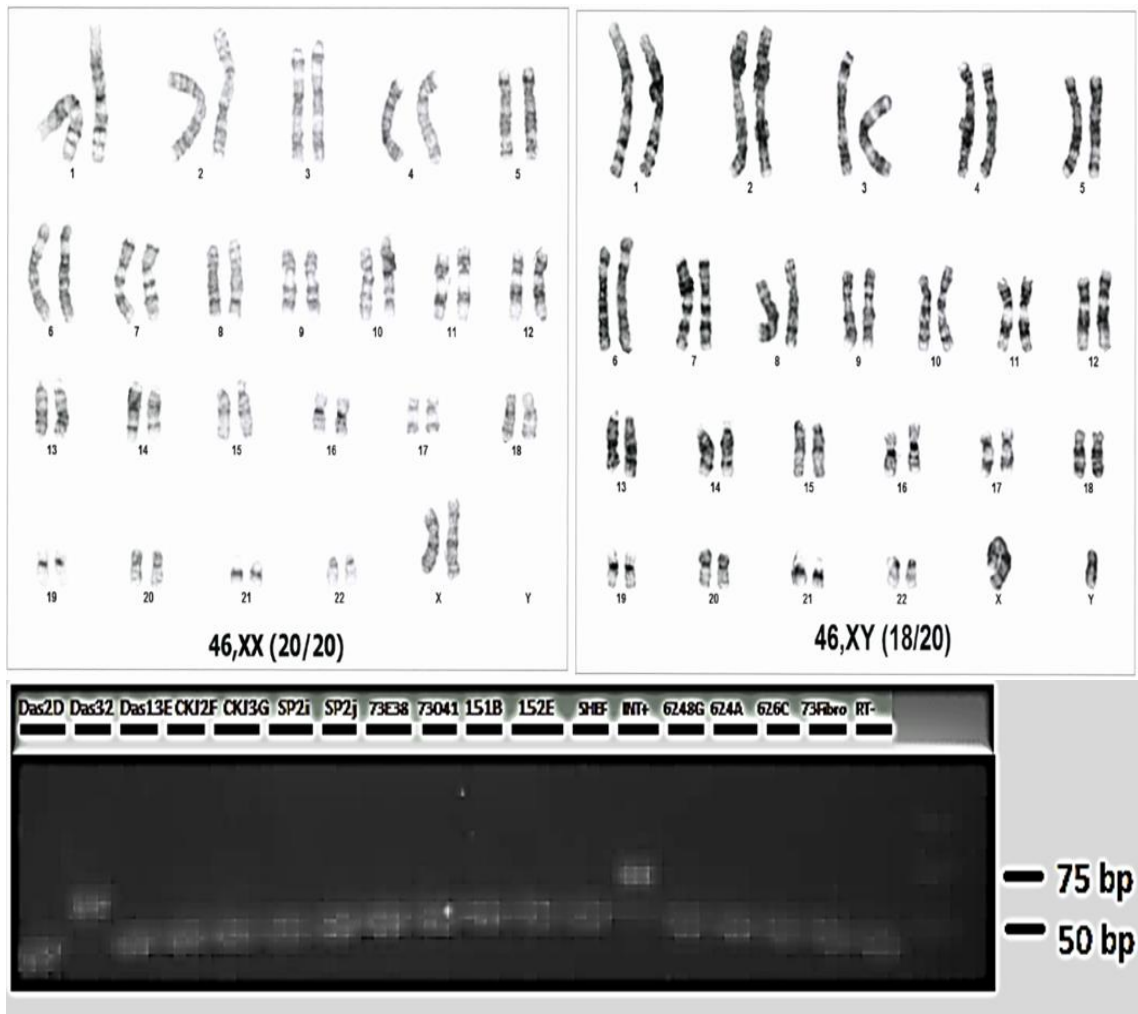


Figure 8-1 Validation characteristics of iPSC used in this study

Top: Example of G-band staining showing a normal karyotype for 73E38 (left) and 152E (right) lines. Bottom: 1.8% agarose DNA gel for PCR of cDNA used in this study. DNA ladder (on the right) is in bp. The expected size of the bands is 61 bp. Shef is an embryonic stem cell line, INT+ is a positive control and 73Fibro is a fibroblasts line. Das32 is a clone that has an integrated episomal plasmid and so discarded from further experiments.

To verify that the newly-derived iPSC lines were pluripotent stem cells, we assessed expression of the pluripotency markers. In addition to exhibiting extracellular staining patterns for both SSEA and TRA-1 proteins, all colonies showed distinct nuclear staining when assayed for NANOG and OCT4 immunoreactivity (Figure 8-2). All iPSC lines generated compact colonies with morphology comparable to those of ESC controls.

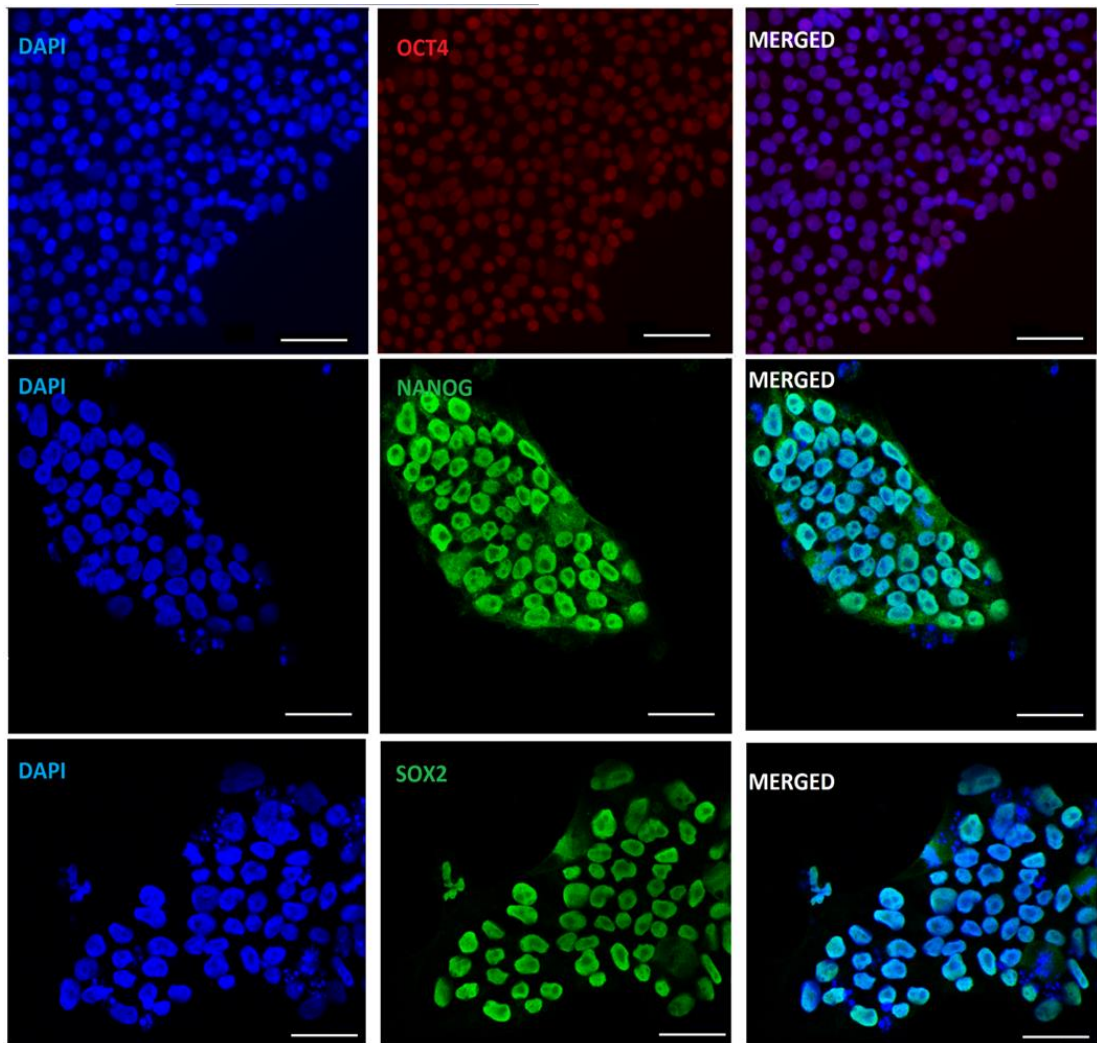


Figure 8-2 Stain for pluripotency markers of the iPSCs

Confocal microscopy images of staining for pluripotency markers of the generated iPSCs. Examples of images to show the presence of OCT-4 (red), NANOG (green), and SOX2 (green) immunofluorescence staining images of DAS2D. Nuclei were counterstained with DAPI (blue). Scale bar represents 80 μm for the top row images and 40 μm for the rest.

To confirm that the observed expression of pluripotency-associated genes was of endogenous origin, we performed qPCR with primers designed to specifically amplify the endogenous OCT4, SOX2, NANOG, L-MYC, S100, KLF4, REX1 and DNMT3B transcripts (Figure 8-3). A parental fibroblast line (73E/O) was used as a negative control (data not shown).

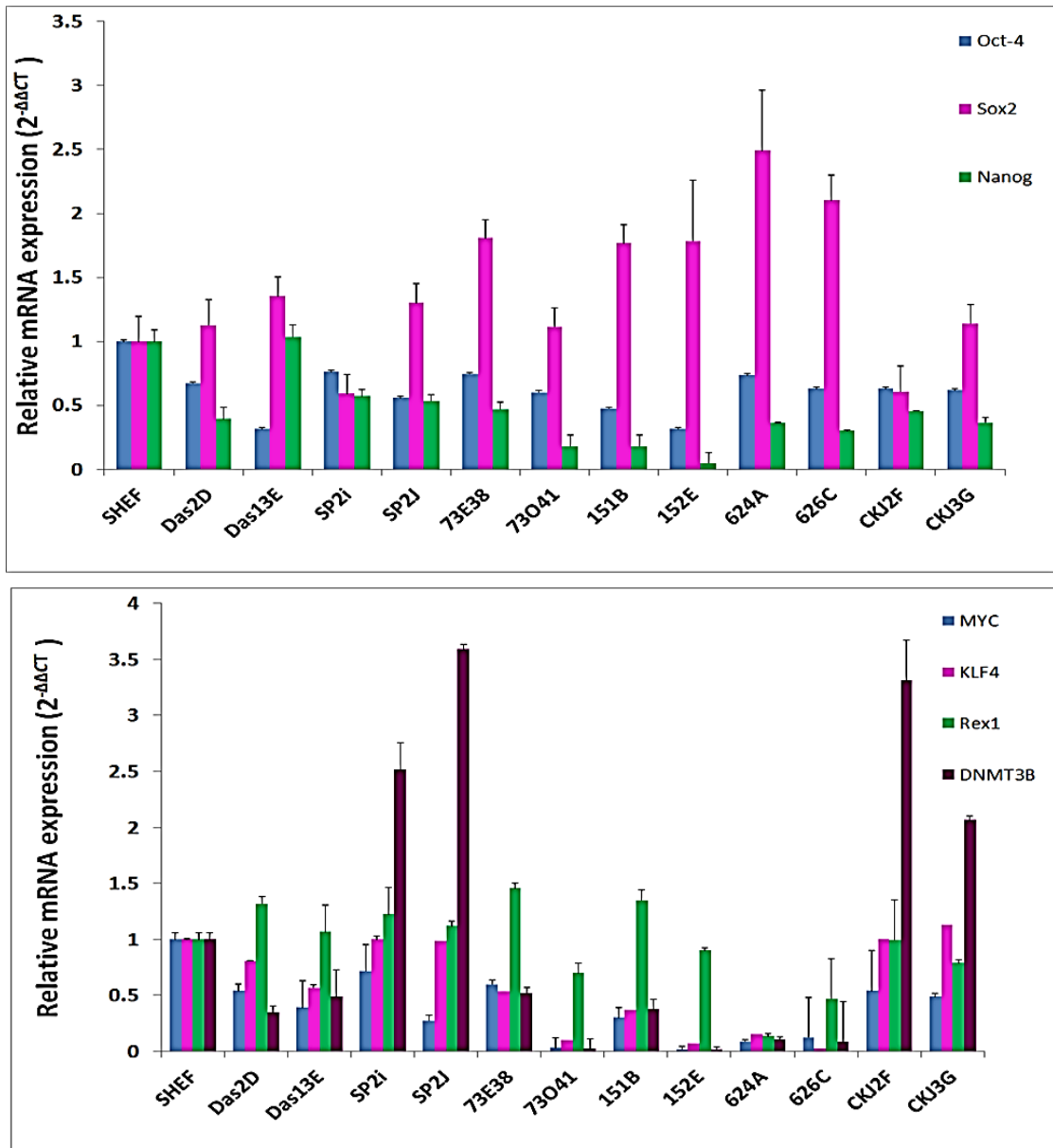


Figure 8-3 q-PCR testing for expression of endogenous pluripotency factors. Quantitative PCR testing for expression of endogenous pluripotency factors (NANOG, REX1, OCT4, SOX2, KLF4, S100, DNMT3B and MYC) in all 12 human iPSC lines. Shef is an embryonic stem cell line used as a reference. Data were generated from at least three independent experiments and was normalized to Shef. Data shows mean \pm SEM.

Furthermore the generated human iPSC lines from this study also exhibited differentiation into representative cell types from all three germ layers *in vitro* based on the structures resembling endoderm, mesoderm and neuroectoderm, indicating the pluripotency of these lines (data not shown).

Neural differentiation of the iPSC lines

Firstly, we generated cortical neurons using a well-established protocol with small molecule dual SMAD inhibition for neural induction, followed by plating of neuroepithelial cells for final differentiation. As expected these cells expressed the intermediate filament protein nestin and Sox1 neural precursor markers, as well as other markers indicative of an NPC phenotype, especially after day 30 (Figure 8-4).

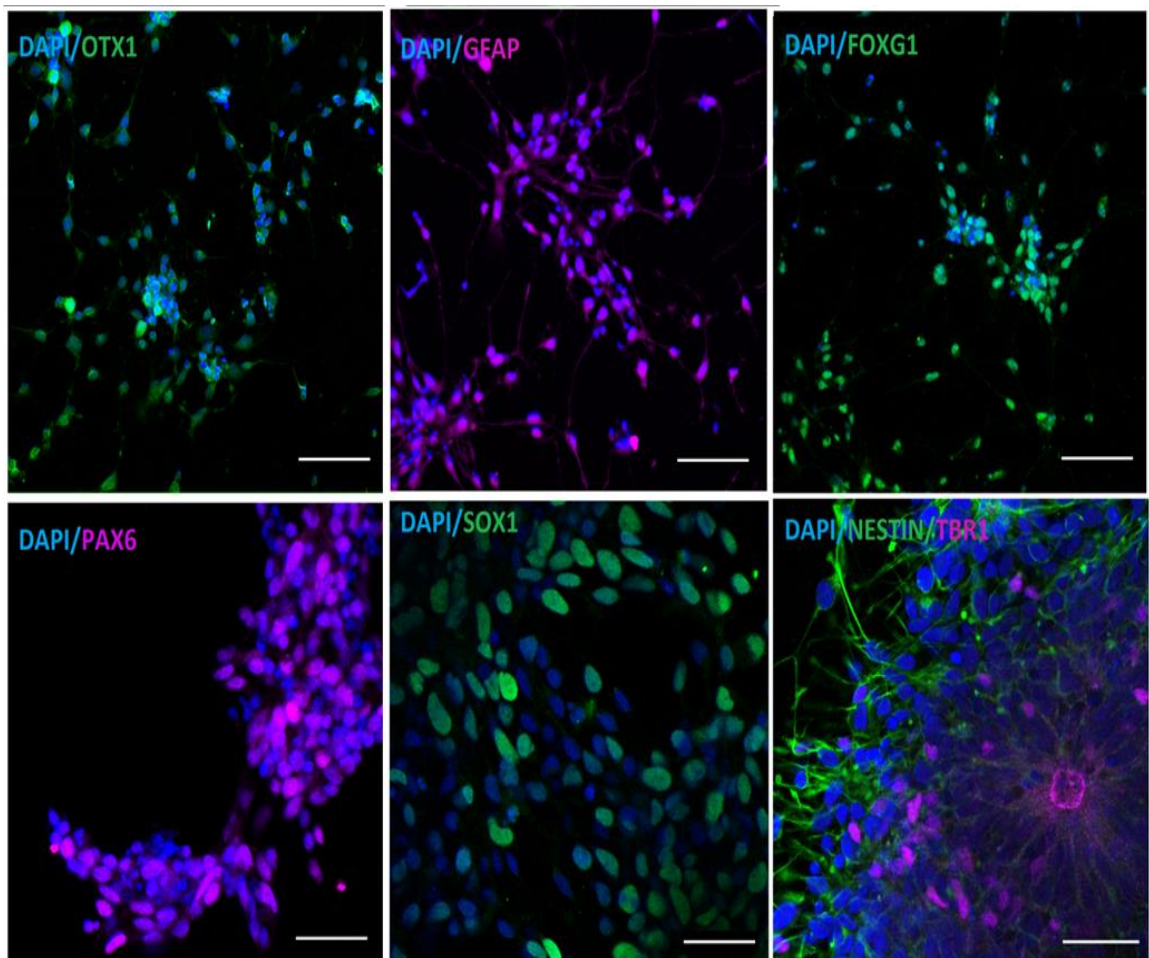


Figure 8-4 Staining for neuronal precursor markers of 73O41

Confocal microscopy images of human iPSC-derived neocortical cortical stem/progenitor cells (73O41). Top images are immunofluorescence staining to confirm the cortical identity of induced neural tissue (Otx1 and Foxg1) as well as the presence of astroglia (GFAP). Scale bar, 80 μm . Bottom images are for Pax6⁺ primary cortical stem/progenitor cells at day 15 validated for cortical identity by Sox1. Additionally, Tbr1⁺ secondary progenitor cells form a basal layer around the rosette structure at day 35. Nuclei are stained with DAPI (blue). Scale bar, 40 μm .

Over the course of neuronal differentiation, cultures showed the expected increase in expression of neuronal genes. An example is given in Figure 8-5 where a clone is compared to a human embryonic line. In addition the figure illustrates the relative levels of mRNA for Ngn2 between the Shef NPC and mature rat cortical primary cultures. The prediction would be that since Ngn2 is expressed in the late G1 phase nuclei and has the ability to drive neuronal differentiation, its requirement would be less in a post mitotic cell. Indeed, the relative levels of the mRNA for Ngn2 are seven times lower in the rat neurons compared to the NPC.

It is thought that Kv1.1 is expressed in the adult cortical rat neurons (Hallows and Tempel, 1998), so we looked at the possibility that it may be expressed at the NPC (Figure 8-5). However, it appears that is not the case.

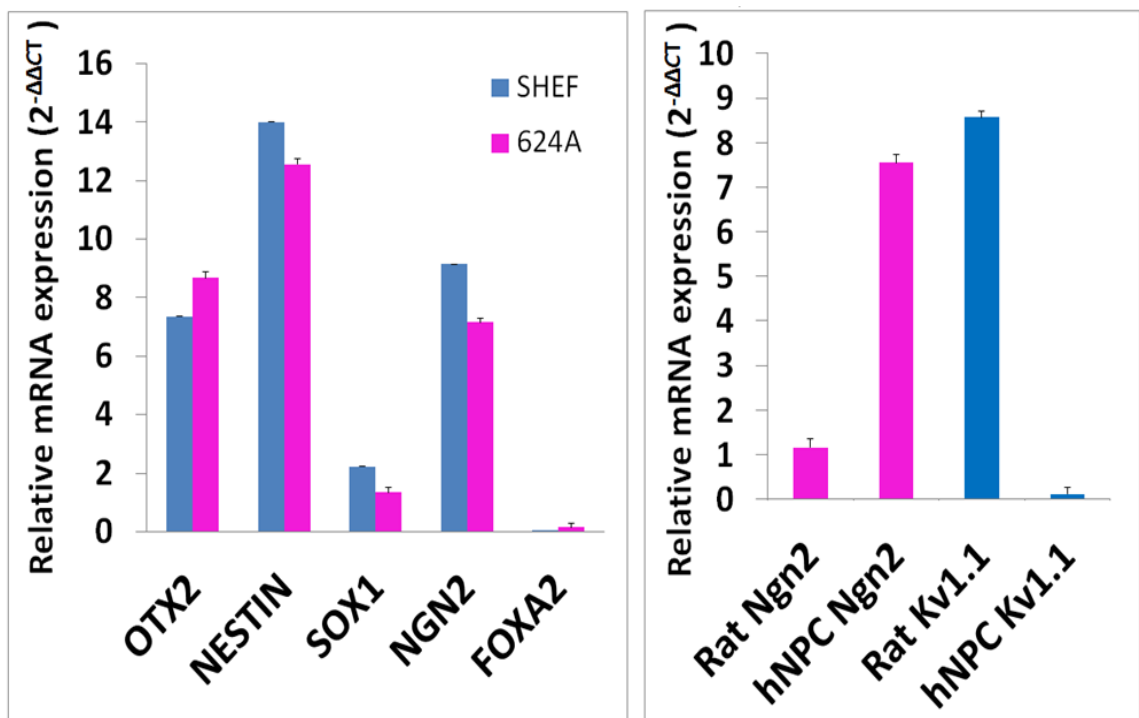


Figure 8-5 qPCR for neural markers

Quantitative RT-PCR measurements of the expression of the NPC markers Otx2, Nestin, Sox1, Ngn2 and FoxA2 in the first three weeks after neuron induction. Data was generated from at least 2 independent experiments. Data for the line was normalized to Shef results for better comparison. B) Quantification of selected mRNA levels in primary rat cortical neurons (DIV 28) and Shef NPC after 4 weeks of neural induction. Data shows mean \pm SEM.

Data for the human iPSC- derived neurons

We next converted the newly formed NPCs from the different lines into neurons by forced expression of the transcription factor Ngn2. However, contrary to the previous strategy of transducing from the iPSC stage, we overexpressed Ngn2 at the NPC stage since it was predicted to provide less variability and require less optimization (Prof Vania Broccoli, personal communication). We had previously used a form of the lentivirus containing Tet-O-Ngn-t2a-Puro, without a fluorescent marker, and since the selection with puromycin (1 $\mu\text{g/ml}$) was unreliable there was no way of telling which cells were virally transduced. Later we started using the lentivirus containing the Tet-O-Ngn-t2a-GFP-Blasticidin plasmid with a GFP reporter and another resistance cassette (provided by Gaia Collasante). However this antibiotic selection proved unreliable and we could not determine the transduction efficiency since most NPC continued to divide in these culture conditions. We stained iPSC-derived neurons at 21 days after induction for GFP (to identify cells with viral transduction) and also for expression of Na_v channels (Pan Na_v) in the axon initial segment. This has a high density of sodium channels and likely plays a role in action potential formation (Kole, 2011). Four weeks after the doxycycline induction of Ngn2 and GFP it became evident that very few of the GFP positive cells were also positive for pan Na_v stain (Figure 8-6). This post-hoc immunostaining was somewhat in agreement with the very low proportion of cells (4 out of 84) exhibiting action potentials and having properties similar to those published in this system (Zhang et al., 2013), so the protocol was dropped.

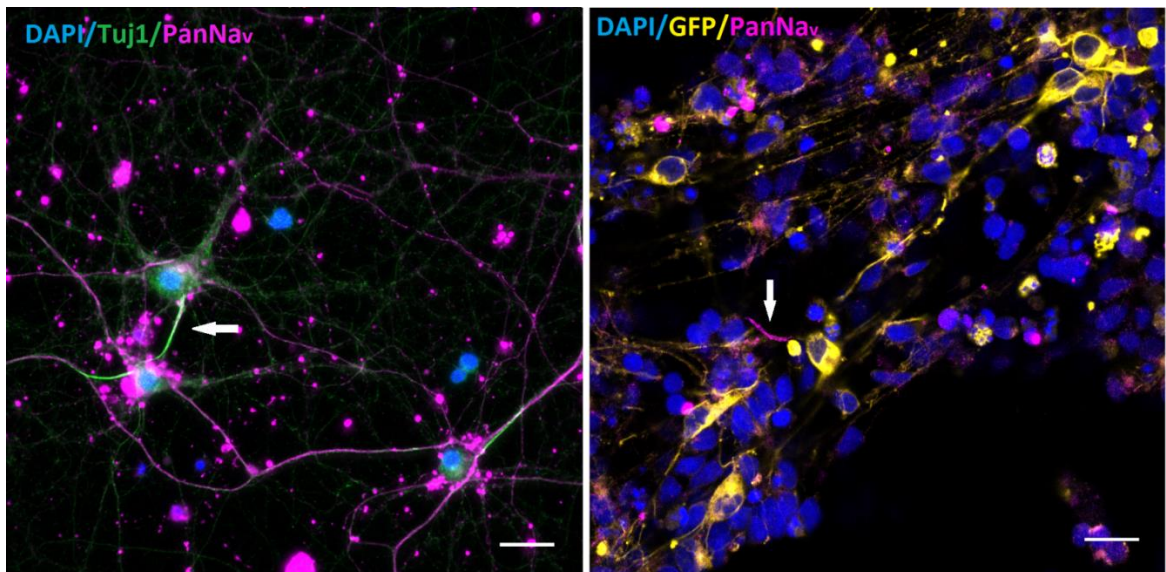


Figure 8-6 Staining for panNav

Confocal microscopy images of primary mouse hippocampal neurons (left) and human iPSC-derived neurons (Shef, right) three weeks after viral transduction. White arrows show positive panNav stain in the axonal initial segment. Nuclei are stained with DAPI (blue). Scale bar, 20 μ m.

Electrophysiological data for the human iN neurons

We next converted the iPSCs directly to neurons to give induced neuronal (iN) cells by forced expression of the transcription factor Ngn2. We used the lentivirus containing the Tet-O-Ngn-t2a-GFP-Blasticidin plasmid with a GFP reporter and another resistance cassette (provided by Gaia Collasante). In this condition the antibiotic selection was successful, however the proportion of cells (19 out of 211 for 152E; 14 out of 169 for SP2i) exhibiting repetitive firing and having properties similar to those published for this system was low and culture batch dependent. Most neurons fired one action potential or none at all and the data for these was discarded. Action potential generation was examined by injecting 0.5 s depolarizing currents of increasing amplitudes (Figure 8-7). Detailed electrophysiological measurements of intrinsic properties were performed among the group of neurons that were defined as mature based on their ability to fire mature action potentials repetitively in response to current injection. Passive and active membrane properties were quantified and compared in order to evaluate differences between lines. Statistical analysis of 152E and SP2i iN neurons (chosen based on the input resistance) from the same batch revealed no difference of the passive and active

properties (Table 8-4 and 8-5; Mann-Whitney U-test). There was also no difference in the firing frequency (data not shown).

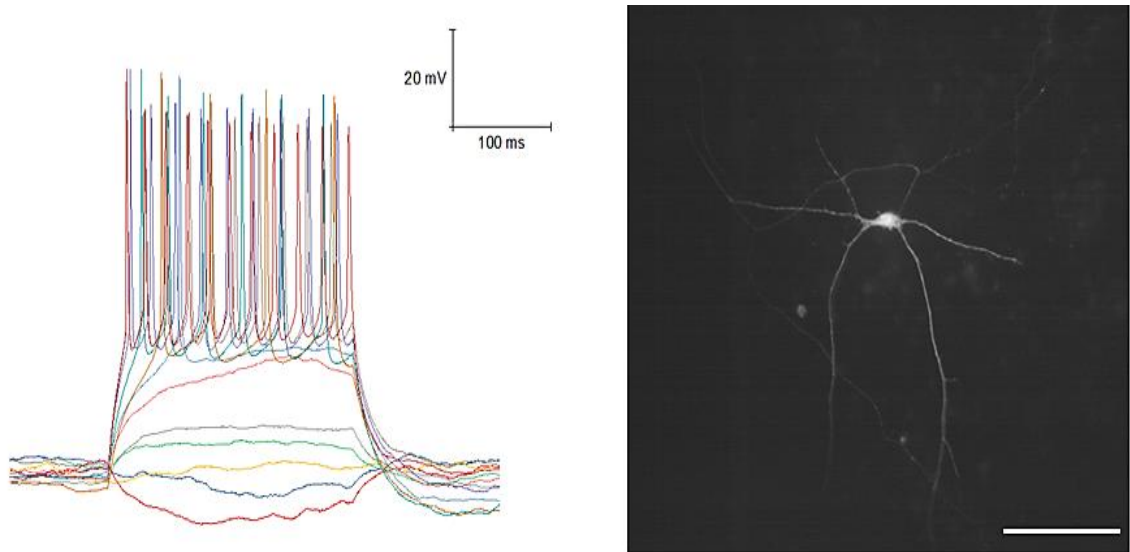


Figure 8-7 Electrophysiological data for the human iN neurons

Left: examples of traces of action potentials at current threshold from 152E. Right: DIC microscopy overlaid with fluorescence image of iN cells derived from 152E, three weeks after viral transduction. Scale bar, 50 μm .

Table 8-4 Parameters of 152E iN neurons

Parameters	N1	N2	N3	N4	N5	N6
Resting membrane potential (mV)	-55.0	-45.0	-49.0	-60.0	-39.0	-59.0
Capacitance (pF)	25.5	29.1	33.2	14.4	18.0	25.0
Input resistance ($\text{M}\Omega$)	447.0	459.0	355.5	696.0	528.7	396.0
Spike voltage threshold (mV)	-28.3	-24.1	-28.5	-32.9	-29.9	-30.7
Spike amplitude (mV)	47.3	38.5	53.3	51.3	41.2	49.2
$\frac{1}{2}$ Width (ms)	1.6	2.1	1.3	1.5	1.8	1.4
90-10 decay (ms)	1.5	1.5	1.2	1.8	1.9	1.3
AHP (mV)	9.9	39.0	15.6	4.0	29.1	10.1

Table 8-5 Parameters of SP2i iN neurons

Parameters	N1	N2	N3	N4	N5	N6
Resting membrane potential (mV)	-35.0	-39.0	-42.0	-54.0	-59.0	-59.0
Capacitance (pF)	56.6	33.9	26.0	24.5	40.9	18.0
Input resistance (M Ω)	812.5	559.5	653.8	726.0	356.0	838.9
Spike voltage threshold (mV)	-29.2	-30.4	-29.8	-41.2	-30.1	-26.9
Spike amplitude (mV)	55.8	68.4	54.2	39.7	54.1	49.3
$\frac{1}{2}$ Width (ms)	1.3	1.8	1.3	2.5	1.3	1.5
90-10 decay (ms)	1.3	2.4	1.2	3.1	1.2	1.4
AHP (mV)	5.7	1.7	15.0	3.2	13.9	10.5

Discussion

The purpose of this study was to investigate the neuronal consequences of the Kv1.1 mutations and the first step was to generate induced pluripotent stem cells from skin fibroblasts of patients with EA1. A total of 12 stable clones for the corresponding 6 lines were produced. The colonies were initially selected based on having a similar morphology to ESCs. Next the standard assays were performed, namely detection of pluripotency markers (through RT-qPCR and/or immunostaining), confirmation of absence of episomal plasmid and cytogenetic analysis. The results of RT-qPCR indicated that iPSCs generated in this study expressed pluripotency markers such as Oct4, Sox2, Rex1, and Myc. Indeed, it has recently been shown that Rex1 is essential for pluripotency and reprogramming, and its depletion leads to loss of self-renewal capacity and full differentiation potential (Son et al., 2013). Additionally, immunofluorescence results showed that our iPSCs expressed pluripotent markers such as Oct4, Sox2, Nanog, SSEA-3 and TRA-1-60 at the protein level. The iPSC lines generated also appeared not to have traces of genomic integration of episomal plasmids and their karyotype was normal. One hallmark characteristic of ESCs and iPSCs is their developmental potential to differentiate into all cell types in the human body (Thomson

et al., 1998). In order to evaluate the developmental capability of the generated iPSCs, the cells were successfully differentiated *in vitro* into various mature cell types representing the three germ layers. Next iPSCs were differentiated into cortical neurons using the Livesey protocol with some modifications (Shi et al., 2012). Published analysis for the generation of relative numbers of different classes of cortical neurons from iPSCs demonstrated that approximately equal numbers of deep- and upper-layer neurons are produced in this system, and these proportions are moreover predicted to be reproducible across different ESC and iPSC lines (Shi et al., 2012). Upon neural induction, the first emerging neuroectodermal cells in the neural plate are known to develop an anterior fate characterized by expression of transcription factors such as Foxg1 and Otx1/2 (Hebert and Fishell, 2008). Indeed our NPCs show positive stain for these transcription factors. The primary cortical progenitor cells generated from iPSCs subsequently give rise to all populations of secondary intermediate progenitor cells, which we have confirmed by immunostaining and confocal microscopy. Early-born deep-layer neurons were observed in our culture based on the staining for Tbr1, and since these are found at the periphery of each neural rosette, it is also possible that they would be positive for Ki67 stain. If the cultures were left for over 3 months then approximately equal proportions of deep- and upper-layer neurons would be expected to be generated (Shi et al., 2012). Ngn2 is expressed in the late G1 phase nuclei and the mechanism by which the protein drives neural differentiation has been described (Ali et al., 2011). Briefly, in an active cycle where cyclin-cdk (cyclin-dependent kinase) levels are high, Ngn2 is in a hyperphosphorylated form. In this state it has a reduced DNA binding affinity that is sufficient only to activate the progenitor-associated target promoters that have open chromatin (Figure 8-8). As the cell cycle lengthens, cyclin-cdk activity is reduced and Ngn2 phosphorylation decreases, resulting in an increase in DNA-binding affinity. Therefore as the cdk levels decrease, the level of progenitor gene expression remains static, but the expression of differentiation genes increases. Indeed, a phosphomutant form of Ngn2 that has all nine serine-proline sites mutated to serine-alanine, and so cannot be phosphorylated by cdks, shows a significantly enhanced ability to drive neuronal differentiation both *in vitro* and *in vivo*, supporting this model (Ali et al., 2011). Another important aspect of the mechanism is the oscillatory nature of protein expression for Ngn2 (Shimojo et al., 2008). When its expression oscillates, Ngn2 induces the maintenance of progenitor cells, but when its expression is sustained, Ngn2 induces

neuronal differentiation (Figure 8-8). This is probably because many downstream genes respond rather slowly to Ngn2 expression and only quickly responding genes such as Notch ligand gene Delta-like1 are selectively induced leading to activation of Notch signaling and the maintenance of progenitor cells (Shimojo et al., 2011).

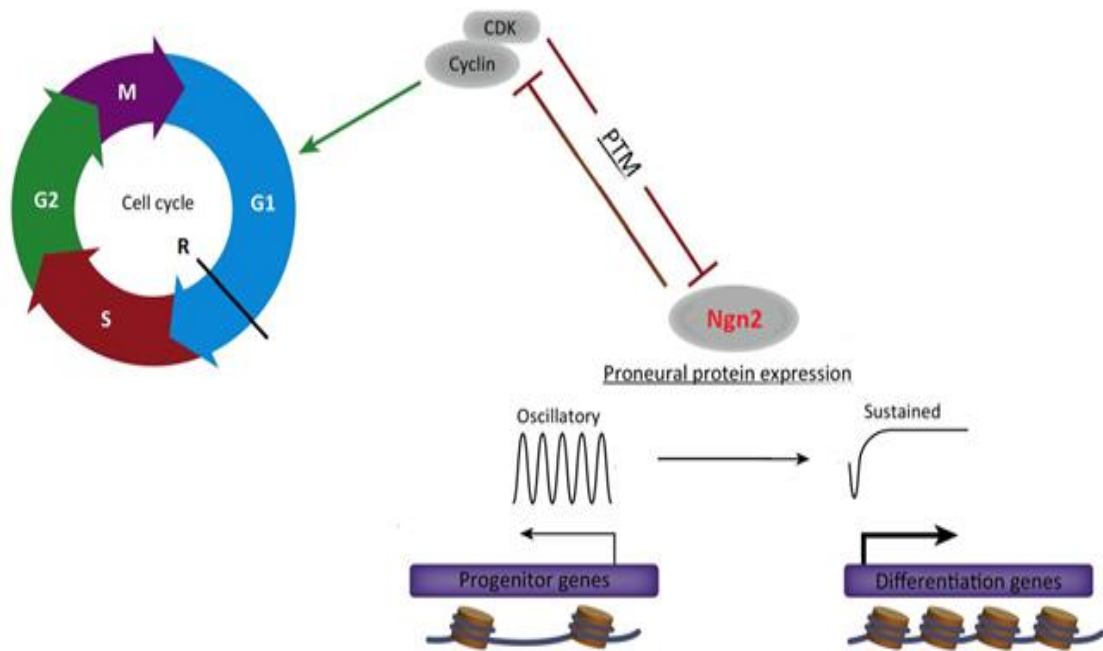


Figure 8-8 Mechanism for cell cycle and neuronal differentiation coordination.

The eukaryotic cell cycle comprises sequential phases: two gap phases (G1 and G2), during which cell growth occurs, and the intervening S phase when nuclear DNA is replicated. M phase (mitosis) constitutes nuclear division and cytokinesis. Transition between phases is driven by specific combinations of cdks with their respective activating cyclin partners, shown in the diagram adjacent to their approximate position in the cell cycle. Active cyclin-cdk complexes drive progression through the cell cycle, but additionally inhibit the expression of differentiation-associated genes by post-translational modification (PTM) of proneural proteins such as Ngn2. An oscillatory expression pattern of Ngn2 is associated with the progenitor state, whereas sustained expression is required to promote differentiation (Hardwick and Philpott, 2014). Progenitor-associated genes often have a relatively more accessible and open chromatin state, whereas the promoters of differentiation genes may require extensive remodeling. Adapted from (Shimojo et al., 2011).

Despite the clear success of generating highly functional neurons, it is also apparent that these cultures often comprise neuronal populations of heterogeneous electrophysiological states (Prilutsky et al., 2014). Several reports of patch-clamping experiments have demonstrated a significant variability of functional maturity among

cell lines, cell batches and even within the same culture dish (Wu et al., 2007, Hu et al., 2010, Belinsky et al., 2011).

In this study we chose to overexpress Ngn2 from the NPC stage in order to achieve a more rapid and reliable homogenous population of neurons (Britz et al., 2006). This did not give a desirable outcome and the protocol was dropped.

We then co-cultured iN cells with mouse cortical primary culture (containing neurons and astrocytes) as this has been shown to enhance the development of electrophysiological parameters (Braun et al., 2012), although it may also increase tissue culture variability (Tang et al., 2013). In this study, the number of cells exhibiting repetitive firing and having properties similar to those published in this work was low and culture batch dependent so this protocol was not pursued further.

The main advantages of patient-specific iPSC are that the effects of patient-relevant mutations can be studied in the correct genetic and cellular background and also that they avert the needs of immune suppressors in cells-based therapy. Some limitations include considerable phenotypic variability that is unrelated to their genotypes, low efficiency of differentiations that cannot provide a consistent platform for drug screening or diagnosis, in addition of being very expensive to culture. PSCs, whether derived from blastocysts or generated by somatic cell reprogramming, differ substantially from canonical mouse embryonic stem cells, which are able to generate homogenous populations of differentiated neurons, and are considered to represent a later phase of epiblast development, termed primed pluripotency (Hackett and Surani, 2014). Dramatic molecular and functional differences exist between different pluripotent cells, which subsequently influence their characteristics, function and safety (Davidson et al., 2015). Published protocols have been able to convert primed human PSCs into a more naive-like phenotype (Davidson et al., 2015). In the future protocols for neural differentiation from this naïve state are expected to give rise to homogeneous populations which will provide more disease relevant information.

Patch clamping is the current gold standard to demonstrate the functionality of a neuronal culture but it is low throughput and provides information for only a low percentage of neurons. This technical limitation precludes a thorough characterization of the functional maturity of the neurons. In order to circumvent this, Gage and colleagues first defined a continuum of poor to highly functional electrophysiological states of differentiated neurons and demonstrated a multimodal machine-learning

strategy to identify new molecular features that predict the physiological states of single neurons, independently of the time spent *in vitro* (Bardy et al., 2016). They then selected a neurophysiological biomarker GDAP1L1, infected neuronal cell lines with a GDAP1L1-eGFP lentivirus and isolated highly functional human neurons (Bardy et al., 2016). Strategies such as these to deliver electrophysiologically homogeneous human neurons have the potential to assist in the modelling and treatment of neurological disorders.

More recently, current-clamp recordings from buttons of cerebellar basket cells and primary hippocampal neurons respectively showed that presynaptic spikes were broadened by pharmacological blockade of Kv1.1 or by a dominant EA1-associated mutation, whereas somatic recordings fail to detect such changes (Begum et al., 2016, Vivekananda et al., 2017). This should be taken into account in future work on modelling EA1.

In conclusion, the directed differentiation of human iPSCs into functional, region-specific neural cells is a key step to realizing their therapeutic promise for the treatment of various neural disorders including EA1. Future applications for iPSC-derived models of EA1 include drug testing and the ability to investigate the mutagenic diversity encountered in EA1 patients.

Conclusions and future work

This thesis has utilised a variety of genetic and functional techniques to investigate five neurological disorders presenting with progressive or episodic neurological symptoms. First, Chapter 3 expands the clinic-genetic spectrum of riboflavin transporter genes to include twenty patients and a range of novel mutations. Clinical case histories were reviewed and pathological evaluation of brain and spinal cord of two patients with confirmed *SLC52A3* mutations who presented either in infancy or in later childhood was undertaken. Although the anatomical distribution of the symmetrical lesions differed in both cases, the morphology of the lesions was identical and moreover matched the pathology seen in mitochondrial encephalopathies (Tanji et al., 2001, Filosto et al., 2007). Finally, a series of experiments in patients' fibroblasts and *Drosophila* were performed to identify the underlying effects of loss of RFVT function on neuronal integrity and mitochondrial function. Our findings implicate mitochondrial dysfunction as a downstream consequence of riboflavin transporter gene defects and validate riboflavin esters as a potential therapeutic strategy. Work has now been started to evaluate mitochondrial oxygen consumption and membrane potential as well as mitochondrial structure in the *Drosophila* model of BVVLS. .

Chapter 4 presents cases with several similarities to the previously reported Saudi family carrying the homozygous *SBF1* variant p.Asp443Asn (Alazami et al., 2014, Bohlega et al., 2011). All except one individual became immobile before their 40s, indicating a severe neuropathy in both families. All Saudi brothers developed facial weakness; in addition, one of them had mild dysarthria and another had dysphagia, (Bohlega et al., 2011). Electrophysiology was consistent with an axonal neuropathy in all individuals although sensory/motor NCVs were decreased in one of the Saudi brothers. Nerve biopsy in both probands showed a decreased number of myelinated axons with no onion bulbs. Some of the features observed in the Saudi family, however, were mild (ophthalmoparesis) or absent (cognitive impairment, microcephaly and syndactyly) in our cases. Given this phenotypic variability and the previous association of *SBF1* with CMT4B3, additional studies are needed to define the clinical spectrum of *SBF1*-related neuropathies.

Chapter 5 provides support for the use of whole exome sequencing as a diagnostic tool for identification of mutations in conditions with complex and wide presentations such as HSP. Furthermore, we extended the findings that mutations in *SPG11* are the cause

of a spectrum of clinical features including the late manifestation of severe axonal neuropathy.

Chapter 6 extends the phenotypes associated with mutations in *KCNA2* to encompass epilepsy, ataxia and HSP, but also highlights the clinical importance of the position of the mutated amino acid residue. Further studies are required to better understand the molecular basis of this novel phenotype and how the specific mutation leads to spastic paraplegia.

Chapter 7 broadens the phenotypes associated with *KCNA1* mutations to include possible susceptibility to MH. Further investigations are necessary to establish how the F249C mutant Kv1.1 channel might affect the depolarization at the plasma membrane and subsequently calcium release.

In Chapter 8, the directed differentiation of human iPSCs into functional, region-specific neural cells was achieved. This is a key step to realizing their therapeutic promise for the treatment of various neural disorders such as EA1. For future work, current-clamp recordings at buttons may prove to be a preferable strategy for the modelling EA1.

Overall the work in this thesis contributes to current research on the functional genetics of neurological disorders. The findings of such studies will hopefully lead to the introduction of new diagnostic tools and the discovery of potential targets for new and more effective medications and preventive measures.

For the future I have secured a postdoctoral position in US in a lab which focuses on modelling neurodegenerative and neuropsychiatric disorders using iPSCs and directly reprogrammed neurons and by looking at specific cellular phenotypes, such as neuronal connectivity, neuronal firing properties and gene expression profiles. This methodology represents a strategy for understanding the basic biological aspects underlying complex neuropsychiatric and neurodevelopmental disease and could potentially have important clinical outcomes such as development of diagnostic tools and new therapies.

References

- ADELMAN, J. P. 1995. Proteins that interact with the pore-forming subunits of voltage-gated ion channels. *Curr Opin Neurobiol*, 5, 286-95.
- AGGARWAL, S. K. & MACKINNON, R. 1996. Contribution of the S4 segment to gating charge in the Shaker K⁺ channel. *Neuron*, 16, 1169-77.
- ALAZAMI, A. M., ALZHRANI, F., BOHLEGA, S. & ALKURAYA, F. S. 2014. SET binding factor 1 (SBF1) mutation causes Charcot-Marie-tooth disease type 4B3. *Neurology*, 82, 1665-6.
- ALBARWANI, S., NEMETZ, L. T., MADDEN, J. A., TOBIN, A. A., ENGLAND, S. K., PRATT, P. F. & RUSCH, N. J. 2003. Voltage-gated K⁺ channels in rat small cerebral arteries: molecular identity of the functional channels. *J Physiol*, 551, 751-63.
- ALI, F., HINDLEY, C., MCDOWELL, G., DEIBLER, R., JONES, A., KIRSCHNER, M., GUILLEMOT, F. & PHILPOTT, A. 2011. Cell cycle-regulated multi-site phosphorylation of Neurogenin 2 coordinates cell cycling with differentiation during neurogenesis. *Development*, 138, 4267-77.
- ANAND, G., HASAN, N., JAYAPAL, S., HUMA, Z., ALI, T., HULL, J., BLAIR, E., MCSHANE, T. & JAYAWANT, S. 2012. Early use of high-dose riboflavin in a case of Brown-Vialetto-Van Laere syndrome. *Developmental medicine and child neurology*, 54, 187-9.
- ASHIZAWA, T., BUTLER, I. J., HARATI, Y. & ROONGTA, S. M. 1983. A dominantly inherited syndrome with continuous motor neuron discharges. *Ann Neurol*, 13, 285-90.
- AZZEDINE, H., BOLINO, A., TAIEB, T., BIROUK, N., DI DUCA, M., BOUHOUCHE, A., BENAMOU, S., MRABET, A., HAMMADOUCHE, T., CHKILI, T., GOUIDER, R., RAVAZZOLO, R., BRICE, A., LAPORTE, J. & LEGUERN, E. 2003. Mutations in MTMR13, a new pseudophosphatase homologue of MTMR2 and Sbf1, in two families with an autosomal recessive demyelinating form of Charcot-Marie-Tooth disease associated with early-onset glaucoma. *American journal of human genetics*, 72, 1141-53.
- BAETS, J., DECONINCK, T., DE VRIENDT, E., ZIMON, M., YPERZEELE, L., VAN HOORENBEECK, K., PEETERS, K., SPIEGEL, R., PARMAN, Y., CEULEMANS, B., VAN BOGAERT, P., POU-SERRADELL, A., BERNERT, G., DINOPOULOS, A., AUER-GRUMBACH, M., SALLINEN, S. L., FABRIZI, G. M., PAULY, F., VAN DEN BERGH, P., BILIR, B., BATTALOGLU, E., MADRID, R. E., KABZINSKA, D., KOCHANSKI, A., TOPALOGLU, H., MILLER, G., JORDANOVA, A., TIMMERMAN, V. & DE JONGHE, P. 2011. Genetic spectrum of hereditary neuropathies with onset in the first year of life. *Brain : a journal of neurology*, 134, 2664-76.

- BAKER, S. K. & TARNOPOLSKY, M. A. 2003. Targeting cellular energy production in neurological disorders. *Expert Opin Investig Drugs*, 12, 1655-79.
- BANSAGI, B., GRIFFIN, H., WHITTAKER, R. G., ANTONIADI, T., EVANGELISTA, T., MILLER, J., GREENSLADE, M., FORESTER, N., DUFF, J., BRADSHAW, A., KLEINLE, S., BOCZONADI, V., STEELE, H., RAMESH, V., FRANKO, E., PYLE, A., LOCHMULLER, H., CHINNERY, P. F. & HORVATH, R. 2017. Genetic heterogeneity of motor neuropathies. *Neurology*, 88, 1226-1234.
- BARDY, C., VAN DEN HURK, M., KAKARADOV, B., ERWIN, J. A., JAEGER, B. N., HERNANDEZ, R. V., EAMES, T., PAUCAR, A. A., GORRIS, M., MARCHAND, C., JAPPELLI, R., BARRON, J., BRYANT, A. K., KELLOGG, M., LASKEN, R. S., RUTTEN, B. P., STEINBUSCH, H. W., YEO, G. W. & GAGE, F. H. 2016. Predicting the functional states of human iPSC-derived neurons with single-cell RNA-seq and electrophysiology. *Mol Psychiatry*, 21, 1573-1588.
- BARRETO, L. C., OLIVEIRA, F. S., NUNES, P. S., DE FRANCA COSTA, I. M., GARCEZ, C. A., GOES, G. M., NEVES, E. L., DE SOUZA SIQUEIRA QUINTANS, J. & DE SOUZA ARAUJO, A. A. 2016. Epidemiologic Study of Charcot-Marie-Tooth Disease: A Systematic Review. *Neuroepidemiology*, 46, 157-65.
- BEGUM, R., BAKIRI, Y., VOLYNSKI, K. E. & KULLMANN, D. M. 2016. Action potential broadening in a presynaptic channelopathy. *Nat Commun*, 7, 12102.
- BELINSKY, G. S., MOORE, A. R., SHORT, S. M., RICH, M. T. & ANTIC, S. D. 2011. Physiological properties of neurons derived from human embryonic stem cells using a dibutyryl cyclic AMP-based protocol. *Stem Cells Dev*, 20, 1733-46.
- BIRCH-MACHIN, M. A., BRIGGS, H. L., SABORIDO, A. A., BINDOFF, L. A. & TURNBULL, D. M. 1994. An evaluation of the measurement of the activities of complexes I-IV in the respiratory chain of human skeletal muscle mitochondria. *Biochem Med Metab Biol*, 51, 35-42.
- BOHLEGA, S., ALAZAMI, A. M., CUPLER, E., AL-HINDI, H., IBRAHIM, E. & ALKURAYA, F. S. 2011. A novel syndromic form of sensory-motor polyneuropathy is linked to chromosome 22q13.31-q13.33. *Clinical Genetics*, 79, 193-5.
- BOLINO, A., MUGLIA, M., CONFORTI, F. L., LEGUERN, E., SALIH, M. A., GEORGIU, D. M., CHRISTODOULOU, K., HAUSMANOWA-PETRUSEWICZ, I., MANDICH, P., SCHENONE, A., GAMBARDELLA, A., BONO, F., QUATTRONE, A., DEVOTO, M. & MONACO, A. P. 2000. Charcot-Marie-Tooth type 4B is caused by mutations in the gene encoding myotubularin-related protein-2. *Nature Genetics*, 25, 17-9.

- BOSCH, A. M., ABELING, N. G., IJLST, L., KNOESTER, H., VAN DER POL, W. L., STROOMER, A. E., WANDERS, R. J., VISSER, G., WIJBURG, F. A., DURAN, M. & WATERHAM, H. R. 2011. Brown-Vialetto-Van Laere and Fazio Londe syndrome is associated with a riboflavin transporter defect mimicking mild MADD: a new inborn error of metabolism with potential treatment. *Journal of inherited metabolic disease*, 34, 159-64.
- BRAHMAJOTHI, M. V., MORALES, M. J., LIU, S., RASMUSSEN, R. L., CAMPBELL, D. L. & STRAUSS, H. C. 1996. In situ hybridization reveals extensive diversity of K⁺ channel mRNA in isolated ferret cardiac myocytes. *Circ Res*, 78, 1083-9.
- BRAND, A. H. & PERRIMON, N. 1993. Targeted gene expression as a means of altering cell fates and generating dominant phenotypes. *Development*, 118, 401-15.
- BRAUN, H., GUNTHER-KERN, A., REYMANN, K. & ONTENIENTE, B. 2012. Neuronal differentiation of human iPS-cells in a rat cortical primary culture. *Acta Neurobiol Exp (Wars)*, 72, 219-29.
- BREW, H. M., GITTELMAN, J. X., SILVERSTEIN, R. S., HANKS, T. D., DEMAS, V. P., ROBINSON, L. C., ROBBINS, C. A., MCKEE-JOHNSON, J., CHIU, S. Y., MESSING, A. & TEMPEL, B. L. 2007. Seizures and reduced life span in mice lacking the potassium channel subunit Kv1.2, but hypoexcitability and enlarged Kv1 currents in auditory neurons. *J Neurophysiol*, 98, 1501-25.
- BRITZ, O., MATTAR, P., NGUYEN, L., LANGEVIN, L. M., ZIMMER, C., ALAM, S., GUILLEMOT, F. & SCHUURMANS, C. 2006. A role for proneural genes in the maturation of cortical progenitor cells. *Cereb Cortex*, 16 Suppl 1, i138-51.
- BROWN, C. 1894. Infantile amyotrophic lateral sclerosis of the family type. *J Nerv Ment Dis* 19, 707-16.
- BROWNE, D. L., GANCHER, S. T., NUTT, J. G., BRUNT, E. R., SMITH, E. A., KRAMER, P. & LITT, M. 1994. Episodic ataxia/myokymia syndrome is associated with point mutations in the human potassium channel gene, KCNA1. *Nat Genet*, 8, 136-40.
- BUCKNER, R. L. 2013. The cerebellum and cognitive function: 25 years of insight from anatomy and neuroimaging. *Neuron*, 80, 807-15.
- CHAMBERS, S. M., FASANO, C. A., PAPAPETROU, E. P., TOMISHIMA, M., SADELAIN, M. & STUDER, L. 2009. Highly efficient neural conversion of human ES and iPS cells by dual inhibition of SMAD signaling. *Nat Biotechnol*, 27, 275-80.
- CHANG, J., LEE, S. & BLACKSTONE, C. 2014. Spastic paraplegia proteins spastizin and spatacsin mediate autophagic lysosome reformation. *J Clin Invest*, 124, 5249-62.

- CHARCOT, J. M. & MARIE, P. 1886. Sur une forme particulière d'atrophie musculaire progressive, souvent familiale débutant par les pieds et les jambes et atteignant plus tard les mains. . *Revue de medecine*, 6, 97–138.
- COUTINHO, P., BARROS, J., ZEMMOURI, R., GUIMARAES, J., ALVES, C., CHORAO, R., LOURENCO, E., RIBEIRO, P., LOUREIRO, J. L., SANTOS, J. V., HAMRI, A., PATERNOTTE, C., HAZAN, J., SILVA, M. C., PRUD'HOMME, J. F. & GRID, D. 1999. Clinical heterogeneity of autosomal recessive spastic paraplegias: analysis of 106 patients in 46 families. *Arch Neurol*, 56, 943-9.
- COZZOLINO, M. & CARRI, M. T. 2012. Mitochondrial dysfunction in ALS. *Prog Neurobiol*, 97, 54-66.
- D'ADAMO, M. C., GALLENMULLER, C., SERVETTINI, I., HARTL, E., TUCKER, S. J., ARNING, L., BISKUP, S., GROTTESI, A., GUGLIELMI, L., IMBRICI, P., BERNASCONI, P., DI GIOVANNI, G., FRANCIOLINI, F., CATACUZZENO, L., PESSIA, M. & KLOPSTOCK, T. 2014. Novel phenotype associated with a mutation in the KCNA1(Kv1.1) gene. *Front Physiol*, 5, 525.
- DAVIDSON, K. C., MASON, E. A. & PERA, M. F. 2015. The pluripotent state in mouse and human. *Development*, 142, 3090-9.
- DAYAL, A. M., JENKINS, M. E., JOG, M. S., KIMPINSKI, K., MACDONALD, P. & GOFTON, T. E. 2017. Palliative Care Discussions in Multiple System Atrophy: A Retrospective Review. *Can J Neurol Sci*, 44, 276-282.
- DELEMOTTE, L., TREPTOW, W., KLEIN, M. L. & TAREK, M. 2010. Effect of sensor domain mutations on the properties of voltage-gated ion channels: molecular dynamics studies of the potassium channel Kv1.2. *Biophys J*, 99, L72-4.
- DIETZL, G., CHEN, D., SCHNORRER, F., SU, K. C., BARINOVA, Y., FELLNER, M., GASSER, B., KINSEY, K., OPPEL, S., SCHEIBLAUER, S., COUTO, A., MARRA, V., KELEMAN, K. & DICKSON, B. J. 2007. A genome-wide transgenic RNAi library for conditional gene inactivation in Drosophila. *Nature*, 448, 151-6.
- DISTELMAIER, F., KOOPMAN, W. J., VAN DEN HEUVEL, L. P., RODENBURG, R. J., MAYATEPEK, E., WILLEMS, P. H. & SMEITINK, J. A. 2009. Mitochondrial complex I deficiency: from organelle dysfunction to clinical disease. *Brain*, 132, 833-42.
- EFTHYMIOU, S., MANOLE, A. & HOULDEN, H. 2016. Next-generation sequencing in neuromuscular diseases. *Curr Opin Neurol*, 29, 527-36.

- EUNSON, L. H., REA, R., ZUBERI, S. M., YOUROUKOS, S., PANAYIOTOPOULOS, C. P., LIGUORI, R., AVONI, P., MCWILLIAM, R. C., STEPHENSON, J. B., HANNA, M. G., KULLMANN, D. M. & SPAUSCHUS, A. 2000. Clinical, genetic, and expression studies of mutations in the potassium channel gene KCNA1 reveal new phenotypic variability. *Ann Neurol*, 48, 647-56.
- FILOSTO, M., TOMELLERI, G., TONIN, P., SCARPELLI, M., VATTEMI, G., RIZZUTO, N., PADOVANI, A. & SIMONATI, A. 2007. Neuropathology of mitochondrial diseases. *Biosci Rep*, 27, 23-30.
- FINSTERER, J., LOSCHER, W., QUAETHOFF, S., WANSCHITZ, J., AUER-GRUMBACH, M. & STEVANIN, G. 2012. Hereditary spastic paraplegias with autosomal dominant, recessive, X-linked, or maternal trait of inheritance. *J Neurol Sci*, 318, 1-18.
- FIRESTEIN, R., NAGY, P. L., DALY, M., HUIE, P., CONTI, M. & CLEARY, M. L. 2002. Male infertility, impaired spermatogenesis, and azoospermia in mice deficient for the pseudophosphatase Sbf1. *J Clin Invest*, 109, 1165-72.
- FOLEY, A. R., MENEZES, M. P., PANDRAUD, A., GONZALEZ, M. A., AL-ODAIB, A., ABRAMS, A. J., SUGANO, K., YONEZAWA, A., MANZUR, A. Y., BURNS, J., HUGHES, I., MCCULLAGH, B. G., JUNGBLUTH, H., LIM, M. J., LIN, J. P., MEGARBANE, A., URTIZBEREA, J. A., SHAH, A. H., ANTONY, J., WEBSTER, R., BROOMFIELD, A., NG, J., MATHEW, A. A., O'BYRNE, J. J., FORMAN, E., SCOTO, M., PRASAD, M., O'BRIEN, K., OLPIN, S., OPPENHEIM, M., HARGREAVES, I., LAND, J. M., WANG, M. X., CARPENTER, K., HORVATH, R., STRAUB, V., LEK, M., GOLD, W., FARRELL, M. O., BRANDNER, S., PHADKE, R., MATSUBARA, K., MCGARVEY, M. L., SCHERER, S. S., BAXTER, P. S., KING, M. D., CLAYTON, P., RAHMAN, S., REILLY, M. M., OUVRIER, R. A., CHRISTODOULOU, J., ZUCHNER, S., MUNTONI, F. & HOULDEN, H. 2014. Treatable childhood neuronopathy caused by mutations in riboflavin transporter RFVT2. *Brain*, 137, 44-56.
- FRIEDERICH, P., BENZENBERG, D., TRELAKIS, S. & URBAN, B. W. 2001. Interaction of volatile anesthetics with human Kv channels in relation to clinical concentrations. *Anesthesiology*, 95, 954-8.
- FROLUND, B., GRIEBE, T. & NIELSEN, P. H. 1995. Enzymatic activity in the activated-sludge floc matrix. *Appl Microbiol Biotechnol*, 43, 755-61.
- FUKUI, H. & MORAES, C. T. 2007. Extended polyglutamine repeats trigger a feedback loop involving the mitochondrial complex III, the proteasome and huntingtin aggregates. *Hum Mol Genet*, 16, 783-97.
- GANDHI, S., WOOD-KACZMAR, A., YAO, Z., PLUN-FAVREAU, H., DEAS, E., KLUPSCH, K., DOWNWARD, J., LATCHMAN, D. S., TABRIZI, S. J., WOOD, N. W., DUCHEN, M. R. & ABRAMOV, A. Y. 2009. PINK1-associated Parkinson's disease is caused by neuronal vulnerability to calcium-induced cell death. *Mol Cell*, 33, 627-38.

- GEIGER, J. R. & JONAS, P. 2000. Dynamic control of presynaptic Ca²⁺ inflow by fast-inactivating K⁺ channels in hippocampal mossy fiber boutons. *Neuron*, 28, 927-39.
- GIANCASPERO, T. A., LOCATO, V., DE PINTO, M. C., DE GARA, L. & BARILE, M. 2009. The occurrence of riboflavin kinase and FAD synthetase ensures FAD synthesis in tobacco mitochondria and maintenance of cellular redox status. *Febs j*, 276, 219-31.
- GINSBERG, L., MALIK, O., KENTON, A. R., SHARP, D., MUDDLE, J. R., DAVIS, M. B., WINER, J. B., ORRELL, R. W. & KING, R. H. 2004. Coexistent hereditary and inflammatory neuropathy. *Brain*, 127, 193-202.
- GOLPICH, M., AMINI, E., MOHAMED, Z., AZMAN ALI, R., MOHAMED IBRAHIM, N. & AHMADIANI, A. 2016. Mitochondrial Dysfunction and Biogenesis in Neurodegenerative diseases: Pathogenesis and Treatment. *CNS Neurosci Ther*.
- GRAVELEY, B. R., BROOKS, A. N., CARLSON, J. W., DUFF, M. O., LANDOLIN, J. M., YANG, L., ARTIERI, C. G., VAN BAREN, M. J., BOLEY, N., BOOTH, B. W., BROWN, J. B., CHERBAS, L., DAVIS, C. A., DOBIN, A., LI, R., LIN, W., MALONE, J. H., MATTIUZZO, N. R., MILLER, D., STURGILL, D., TUCH, B. B., ZALESKI, C., ZHANG, D., BLANCHETTE, M., DUDOIT, S., EADS, B., GREEN, R. E., HAMMONDS, A., JIANG, L., KAPRANOV, P., LANGTON, L., PERRIMON, N., SANDLER, J. E., WAN, K. H., WILLINGHAM, A., ZHANG, Y., ZOU, Y., ANDREWS, J., BICKEL, P. J., BRENNER, S. E., BRENT, M. R., CHERBAS, P., GINGERAS, T. R., HOSKINS, R. A., KAUFMAN, T. C., OLIVER, B. & CELNIKER, S. E. 2011. The developmental transcriptome of *Drosophila melanogaster*. *Nature*, 471, 473-9.
- GREEN, P., WISEMAN, M., CROW, Y. J., HOULDEN, H., RIPHAGEN, S., LIN, J. P., RAYMOND, F. L., CHILDS, A. M., SHERIDAN, E., EDWARDS, S. & JOSIFOVA, D. J. 2010. Brown-Vialetto-Van Laere syndrome, a ponto-bulbar palsy with deafness, is caused by mutations in c20orf54. *Am J Hum Genet*, 86, 485-9.
- GREENE, J. C., WHITWORTH, A. J., KUO, I., ANDREWS, L. A., FEANY, M. B. & PALLANCK, L. J. 2003. Mitochondrial pathology and apoptotic muscle degeneration in *Drosophila parkin* mutants. *Proc Natl Acad Sci U S A*, 100, 4078-83.
- HAACK, T. B., MAKOWSKI, C., YAO, Y., GRAF, E., HEMPEL, M., WIELAND, T., TAUER, U., AHTING, U., MAYR, J. A., FREISINGER, P., YOSHIMATSU, H., INUI, K., STROM, T. M., MEITINGER, T., YONEZAWA, A. & PROKISCH, H. 2012. Impaired riboflavin transport due to missense mutations in SLC52A2 causes Brown-Vialetto-Van Laere syndrome. *Journal of inherited metabolic disease*, 35, 943-8.
- HACKETT, J. A. & SURANI, M. A. 2014. Regulatory principles of pluripotency: from the ground state up. *Cell Stem Cell*, 15, 416-30.

- HALLOWS, J. L. & TEMPEL, B. L. 1998. Expression of Kv1.1, a Shaker-like potassium channel, is temporally regulated in embryonic neurons and glia. *J Neurosci*, 18, 5682-91.
- HARDWICK, L. J. & PHILPOTT, A. 2014. Nervous decision-making: to divide or differentiate. *Trends Genet*, 30, 254-61.
- HARGREAVES, I. P., HEALES, S. J. & LAND, J. M. 1999. Mitochondrial respiratory chain defects are not accompanied by an increase in the activities of lactate dehydrogenase or manganese superoxide dismutase in paediatric skeletal muscle biopsies. *J Inherit Metab Dis*, 22, 925-31.
- HAWKINS, F. & KOTTON, D. N. 2015. Embryonic and induced pluripotent stem cells for lung regeneration. *Ann Am Thorac Soc*, 12 Suppl 1, S50-3.
- HEBERT, J. M. & FISHELL, G. 2008. The genetics of early telencephalon patterning: some assembly required. *Nat Rev Neurosci*, 9, 678-85.
- HEEROMA, J. H., HENNEBERGER, C., RAJAKULENDRAN, S., HANNA, M. G., SCHORGE, S. & KULLMANN, D. M. 2009. Episodic ataxia type 1 mutations differentially affect neuronal excitability and transmitter release. *Dis Model Mech*, 2, 612-9.
- HEHR, U., BAUER, P., WINNER, B., SCHULE, R., OLMEZ, A., KOEHLER, W., UYANIK, G., ENGEL, A., LENZ, D., SEIBEL, A., HEHR, A., PLOETZ, S., GAMEZ, J., ROLFS, A., WEIS, J., RINGER, T. M., BONIN, M., SCHUIERER, G., MARIENHAGEN, J., BOGDAHN, U., WEBER, B. H., TOPALOGLU, H., SCHOLS, L., RIESS, O. & WINKLER, J. 2007. Long-term course and mutational spectrum of spatacsin-linked spastic paraplegia. *Ann Neurol*, 62, 656-65.
- HELBIG, K. L., HEDRICH, U. B., SHINDE, D. N., KREY, I., TEICHMANN, A. C., HENTSCHEL, J., SCHUBERT, J., CHAMBERLIN, A. C., HUETHER, R., LU, H. M., ALCARAZ, W. A., TANG, S., JUNGBLUTH, C., DUGAN, S. L., VAINIONPAA, L., KARLE, K. N., SYNOFZIK, M., SCHOLS, L., SCHULE, R., LEHESJOKI, A. E., HELBIG, I., LERCHE, H. & LEMKE, J. R. 2016. A recurrent mutation in KCNA2 as a novel cause of hereditary spastic paraplegia and ataxia. *Ann Neurol*, 80.
- HENRIQUES, B. J., OLSEN, R. K., BROSS, P. & GOMES, C. M. 2010. Emerging roles for riboflavin in functional rescue of mitochondrial beta-oxidation flavoenzymes. *Curr Med Chem*, 17, 3842-54.
- HERSON, P. S., VIRK, M., RUSTAY, N. R., BOND, C. T., CRABBE, J. C., ADELMAN, J. P. & MAYLIE, J. 2003. A mouse model of episodic ataxia type-1. *Nat Neurosci*, 6, 378-83.
- HIRANO, R., TAKASHIMA, H., UMEHARA, F., ARIMURA, H., MICHIZONO, K., OKAMOTO, Y., NAKAGAWA, M., BOERKOEL, C. F., LUPSKI, J. R., OSAME, M. & ARIMURA, K. 2004. SET

binding factor 2 (SBF2) mutation causes CMT4B with juvenile onset glaucoma. *Neurology*, 63, 577-80.

- HNIA, K., VACCARI, I., BOLINO, A. & LAPORTE, J. 2012. Myotubularin phosphoinositide phosphatases: cellular functions and disease pathophysiology. *Trends in Molecular Medicine*, 18, 317-27.
- HO, G., YONEZAWA, A., MASUDA, S., INUI, K., SIM, K. G., CARPENTER, K., OLSEN, R. K., MITCHELL, J. J., RHEAD, W. J., PETERS, G. & CHRISTODOULOU, J. 2011. Maternal riboflavin deficiency, resulting in transient neonatal-onset glutaric aciduria Type 2, is caused by a microdeletion in the riboflavin transporter gene GPR172B. *Hum Mutat*, 32, E1976-84.
- HOGLINGER, G. U., CARRARD, G., MICHEL, P. P., MEDJA, F., LOMBES, A., RUBERG, M., FRIGUET, B. & HIRSCH, E. C. 2003. Dysfunction of mitochondrial complex I and the proteasome: interactions between two biochemical deficits in a cellular model of Parkinson's disease. *J Neurochem*, 86, 1297-307.
- HU, B. Y., WEICK, J. P., YU, J., MA, L. X., ZHANG, X. Q., THOMSON, J. A. & ZHANG, S. C. 2010. Neural differentiation of human induced pluripotent stem cells follows developmental principles but with variable potency. *Proc Natl Acad Sci U S A*, 107, 4335-40.
- HUGHES, R. 2008. Peripheral nerve diseases: the bare essentials. *Pract Neurol*, 8, 396-405.
- INTOH, A., SUZUKI, N., KOSZKA, K. & EGGAN, K. 2016. SLC52A3, A Brown-Vialetto-van Laere syndrome candidate gene is essential for mouse development, but dispensable for motor neuron differentiation. *Hum Mol Genet*, 25, 1814-23.
- ISHIURA, H., TAKAHASHI, Y., HAYASHI, T., SAITO, K., FURUYA, H., WATANABE, M., MURATA, M., SUZUKI, M., SUGIURA, A., SAWAI, S., SHIBUYA, K., UEDA, N., ICHIKAWA, Y., KANAZAWA, I., GOTO, J. & TSUJI, S. 2016. Molecular epidemiology and clinical spectrum of hereditary spastic paraplegia in the Japanese population based on comprehensive mutational analyses. *J Hum Genet*, 61, 363-4.
- JANG, Y. Y. & YE, Z. 2016. Gene correction in patient-specific iPSCs for therapy development and disease modeling. *Hum Genet*, 135, 1041-58.
- JAYADEV, S. & BIRD, T. D. 2013. Hereditary ataxias: overview. *Genet Med*, 15, 673-683.
- JEN, J. C., GRAVES, T. D., HESS, E. J., HANNA, M. G., GRIGGS, R. C. & BALOH, R. W. 2007. Primary episodic ataxias: diagnosis, pathogenesis and treatment. *Brain*, 130, 2484-93.

- JOHNSON, J. O., GIBBS, J. R., MEGARBANE, A., URTIZBEREA, J. A., HERNANDEZ, D. G., FOLEY, A. R., AREPALLI, S., PANDRAUD, A., SIMON-SANCHEZ, J., CLAYTON, P., REILLY, M. M., MUNTONI, F., ABRAMZON, Y., HOULDEN, H. & SINGLETON, A. B. 2012. Exome sequencing reveals riboflavin transporter mutations as a cause of motor neuron disease. *Brain*, 135, 2875-82.
- KARA, E., TUCCI, A., MANZONI, C., LYNCH, D. S., ELPIDOROU, M., BETTENCOURT, C., CHELBAN, V., MANOLE, A., HAMED, S. A., HARIDY, N. A., FEDEROFF, M., PREZA, E., HUGHES, D., PITTMAN, A., JAUNMUKTANE, Z., BRANDNER, S., XIROMERISIOU, G., WIETHOFF, S., SCHOTTLAENDER, L., PROUKAKIS, C., MORRIS, H., WARNER, T., BHATIA, K. P., KORLIPARA, L. V., SINGLETON, A. B., HARDY, J., WOOD, N. W., LEWIS, P. A. & HOULDEN, H. 2016. Genetic and phenotypic characterization of complex hereditary spastic paraplegia. *Brain*, 139, 1904-18.
- KIM, S. A., VACRATIS, P. O., FIRESTEIN, R., CLEARY, M. L. & DIXON, J. E. 2003. Regulation of myotubularin-related (MTMR)2 phosphatidylinositol phosphatase by MTMR5, a catalytically inactive phosphatase. *Proceedings of the National Academy of Sciences of the United States of America*, 100, 4492-7.
- KING, T. S. 1967. Preparations of succinate-cytochrome c reductase and the cytochrome b-c1 particle. *Methods Enzymology*, 10, 217-235.
- KOLE, M. H. 2011. First node of Ranvier facilitates high-frequency burst encoding. *Neuron*, 71, 671-82.
- KULLMANN, D., HOULDEN, H. & LUNN, M. 2016. Mechanisms of Neurological Disease. *Neurology*. John Wiley & Sons, Ltd.
- KULLMANN, D. M. & HANNA, M. G. 2002. Neurological disorders caused by inherited ion-channel mutations. *Lancet Neurol*, 1, 157-66.
- LAI, H. C. & JAN, L. Y. 2006. The distribution and targeting of neuronal voltage-gated ion channels. *Nat Rev Neurosci*, 7, 548-62.
- LAPORTE, J., BEDEZ, F., BOLINO, A. & MANDEL, J. L. 2003. Myotubularins, a large disease-associated family of cooperating catalytically active and inactive phosphoinositides phosphatases. *Human Molecular Genetics*, 12 Spec No 2, R285-92.
- LAURENS, B., VERGNET, S., LOPEZ, M. C., FOUBERT-SAMIER, A., TISON, F., FERNAGUT, P. O. & MEISSNER, W. G. 2017. Multiple System Atrophy - State of the Art. *Curr Neurol Neurosci Rep*, 17, 41.

- LEZI, E. & SWERDLOW, R. H. 2012. Mitochondria in neurodegeneration. *Adv Exp Med Biol*, 942, 269-86.
- LI, H. & DURBIN, R. 2009. Fast and accurate short read alignment with Burrows-Wheeler transform. *Bioinformatics*, 25, 1754-60.
- LIENHART, W.-D., GUDIPATI, V. & MACHEROUX, P. 2013. The human flavoproteome. *Archives of Biochemistry and Biophysics*, 535, 150-162.
- LIN, M. T. & BEAL, M. F. 2006. Mitochondrial dysfunction and oxidative stress in neurodegenerative diseases. *Nature*, 443, 787-95.
- LIU, J., ZHENG, Q., DENG, Y., CHENG, C. S., KALLENBACH, N. R. & LU, M. 2006. A seven-helix coiled coil. *Proc Natl Acad Sci U S A*, 103, 15457-62.
- LIVAK, K. J. & SCHMITTGEN, T. D. 2001. Analysis of relative gene expression data using real-time quantitative PCR and the 2^{(-Delta Delta C(T))} Method. *Methods*, 25, 402-8.
- LO GIUDICE, T., LOMBARDI, F., SANTORELLI, F. M., KAWARAI, T. & ORLACCHIO, A. 2014. Hereditary spastic paraplegia: clinical-genetic characteristics and evolving molecular mechanisms. *Exp Neurol*, 261, 518-39.
- LONG, S. B., CAMPBELL, E. B. & MACKINNON, R. 2005. Voltage sensor of Kv1.2: structural basis of electromechanical coupling. *Science*, 309, 903-8.
- LORINCZ, A. & NUSSER, Z. 2008. Cell-type-dependent molecular composition of the axon initial segment. *J Neurosci*, 28, 14329-40.
- LUNN, M., HANNA, M., HOWARD, R., PARTON, M., RAHMAN, S., REILLY, M., SIDLE, K. & TURNER, C. 2016. Nerve and Muscle Disease. *Neurology*. John Wiley & Sons, Ltd.
- LUPSKI, J. R., DE OCA-LUNA, R. M., SLAUGENHAUPT, S., PENTAO, L., GUZZETTA, V., TRASK, B. J., SAUCEDO-CARDENAS, O., BARKER, D. F., KILLIAN, J. M., GARCIA, C. A., CHAKRAVARTI, A. & PATEL, P. I. 1991. DNA duplication associated with Charcot-Marie-Tooth disease type 1A. *Cell*, 66, 219-32.
- MACKINNON, R. 1991. Determination of the subunit stoichiometry of a voltage-activated potassium channel. *Nature*, 350, 232-5.
- MACKINNON, R. & YELLEN, G. 1990. Mutations affecting TEA blockade and ion permeation in voltage-activated K⁺ channels. *Science*, 250, 276-9.

- MAGRANE, J., CORTEZ, C., GAN, W. B. & MANFREDI, G. 2014. Abnormal mitochondrial transport and morphology are common pathological denominators in SOD1 and TDP43 ALS mouse models. *Hum Mol Genet*, 23, 1413-24.
- MAGRANE, J., HERVIAS, I., HENNING, M. S., DAMIANO, M., KAWAMATA, H. & MANFREDI, G. 2009. Mutant SOD1 in neuronal mitochondria causes toxicity and mitochondrial dynamics abnormalities. *Hum Mol Genet*, 18, 4552-64.
- MALAFRONTI, P., CLARK, H. B., CASTANEDA-SANCHEZ, I., RAISANEN, J. & HATANPAA, K. J. 2013. Brown-Vialetto-Van Laere syndrome: clinical and neuropathologic findings with immunohistochemistry for C20orf54 in three affected patients. *Pediatr Dev Pathol*, 16, 364-71.
- MANCUSO, M., ORSUCCI, D., VOLPI, L., CALSOLARO, V. & SICILIANO, G. 2010. Coenzyme Q10 in neuromuscular and neurodegenerative disorders. *Curr Drug Targets*, 11, 111-21.
- MANOLE, A., CHELBAN, V., HARIDY, N. A., HAMED, S. A., BERARDO, A., REILLY, M. M. & HOULDEN, H. 2016. Severe axonal neuropathy is a late manifestation of SPG11. *Journal of Neurology*, 263, 2278-2286.
- MANOLE, A., FRATTA, P. & HOULDEN, H. 2014. Recent advances in bulbar syndromes: genetic causes and disease mechanisms. *Curr Opin Neurol*, 27, 506-14.
- MANOLE, A., HORGA, A., GAMEZ, J., RAGUER, N., SALVADO, M., SAN MILLAN, B., NAVARRO, C., PITTMANN, A., REILLY, M. M. & HOULDEN, H. 2017a. SBF1 mutations associated with autosomal recessive axonal neuropathy with cranial nerve involvement. *Neurogenetics*, 18, 63-67.
- MANOLE, A. & HOULDEN, H. 2015. Riboflavin Transporter Deficiency Neuronopathy. *GeneReviews® [Internet]*, Seattle (WA): University of Washington, Seattle; 1993-2016.
- MANOLE, A., MANNIKKO, R., HANNA, M. G., KULLMANN, D. M. & HOULDEN, H. 2017b. De novo KCNA2 mutations cause hereditary spastic paraplegia. *Ann Neurol*, 81, 326-328.
- MANTO, M. & MARMOLINO, D. 2009. Cerebellar ataxias. *Curr Opin Neurol*, 22, 419-29.
- MARAT, A. L., DOKAINISH, H. & MCPHERSON, P. S. 2011. DENN domain proteins: regulators of Rab GTPases. *The Journal of biological chemistry*, 286, 13791-800.
- MARTYN, C. N. & HUGHES, R. A. 1997. Epidemiology of peripheral neuropathy. *J Neurol Neurosurg Psychiatry*, 62, 310-8.

- MASSEY, V. 2000. The chemical and biological versatility of riboflavin. *Biochem Soc Trans*, 28, 283-96.
- MAZZO, F., ZWART, R., SERRATTO, G. M., GARDINIER, K. M., PORTER, W., REEL, J., MARAULA, G. & SHER, E. 2016. Reconstitution of synaptic ion channels from rodent and human brain in *Xenopus* oocytes: a biochemical and electrophysiological characterization. *J Neurochem*, 138, 384-96.
- MCCARTHY, T. V., QUANE, K. A. & LYNCH, P. J. 2000. Ryanodine receptor mutations in malignant hyperthermia and central core disease. *Hum Mutat*, 15, 410-7.
- MCINNES, J. 2013. Insights on altered mitochondrial function and dynamics in the pathogenesis of neurodegeneration. *Transl Neurodegener*, 2, 12.
- MCKENNA, A., HANNA, M., BANKS, E., SIVACHENKO, A., CIBULSKIS, K., KERNYTSKY, A., GARIMELLA, K., ALTSHULER, D., GABRIEL, S., DALY, M. & DEPRISTO, M. A. 2010. The Genome Analysis Toolkit: a MapReduce framework for analyzing next-generation DNA sequencing data. *Genome Res*, 20, 1297-303.
- MEHTA, S. L. & LI, P. A. 2009. Neuroprotective role of mitochondrial uncoupling protein 2 in cerebral stroke. *J Cereb Blood Flow Metab*, 29, 1069-78.
- MENZIES, F. M., COOKSON, M. R., TAYLOR, R. W., TURNBULL, D. M., CHRZANOWSKA-LIGHTOWLERS, Z. M., DONG, L., FIGLEWICZ, D. A. & SHAW, P. J. 2002. Mitochondrial dysfunction in a cell culture model of familial amyotrophic lateral sclerosis. *Brain*, 125, 1522-33.
- MERRITT, A., BOOMS, P., SHAW, M. A., MILLER, D. M., DALY, C., BILMEN, J. G., STOWELL, K. M., ALLEN, P. D., STEELE, D. S. & HOPKINS, P. M. 2017. Assessing the pathogenicity of RYR1 variants in malignant hyperthermia. *Br J Anaesth*, 118, 533-543.
- MESTRE, T. A., MANOLE, A., MACDONALD, H., RIAZI, S., KRAEVA, N., HANNA, M. G., LANG, A. E., MANNIKKO, R. & YOON, G. 2016. A novel KCNA1 mutation in a family with episodic ataxia and malignant hyperthermia. *Neurogenetics*, 17, 245-249.
- MILEDI, R., PARKER, I. & SUMIKAWA, K. 1982. Properties of acetylcholine receptors translated by cat muscle mRNA in *Xenopus* oocytes. *Embo j*, 1, 1307-12.
- MONTECCHIANI, C., PEDACE, L., LO GIUDICE, T., CASELLA, A., MEARINI, M., GAUDIELLO, F., PEDROSO, J. L., TERRACCIANO, C., CALTAGIRONE, C., MASSA, R., ST GEORGE-HYSLOP, P. H., BARSOTTINI, O. G., KAWARAI, T. & ORLACCHIO, A. 2016. ALS5/SPG11/KIAA1840 mutations cause autosomal recessive axonal Charcot-Marie-Tooth disease. *Brain*, 139, 73-85.

- NAKHRO, K., PARK, J. M., HONG, Y. B., PARK, J. H., NAM, S. H., YOON, B. R., YOO, J. H., KOO, H., JUNG, S. C., KIM, H. L., KIM, J. Y., CHOI, K. G., CHOI, B. O. & CHUNG, K. W. 2013. SET binding factor 1 (SBF1) mutation causes Charcot-Marie-Tooth disease type 4B3. *Neurology*, 81, 165-73.
- NORTHROP-CLEWES, C. A. & THURNHAM, D. I. 2012. The discovery and characterization of riboflavin. *Ann Nutr Metab*, 61, 224-30.
- O'HALLORAN, C. J., KINSELLA, G. J. & STOREY, E. 2012. The cerebellum and neuropsychological functioning: a critical review. *J Clin Exp Neuropsychol*, 34, 35-56.
- OKITA, K., MATSUMURA, Y., SATO, Y., OKADA, A., MORIZANE, A., OKAMOTO, S., HONG, H., NAKAGAWA, M., TANABE, K., TEZUKA, K., SHIBATA, T., KUNISADA, T., TAKAHASHI, M., TAKAHASHI, J., SAJI, H. & YAMANAKA, S. 2011. A more efficient method to generate integration-free human iPS cells. *Nat Methods*, 8, 409-12.
- PALOMO, G. M. & MANFREDI, G. 2015. Exploring new pathways of neurodegeneration in ALS: the role of mitochondria quality control. *Brain Res*, 1607, 36-46.
- PENA, S. D. & COIMBRA, R. L. 2015. Ataxia and myoclonic epilepsy due to a heterozygous new mutation in KCNA2: proposal for a new channelopathy. *Clin Genet*, 87, e1-3.
- PENSATO, V., CASTELLOTTI, B., GELLERA, C., PAREYSON, D., CIANO, C., NANETTI, L., SALSANO, E., PISCOSQUITO, G., SARTO, E., EOLI, M., MORONI, I., SOLIVERI, P., LAMPERTI, E., CHIAPPARINI, L., DI BELLA, D., TARONI, F. & MARIOTTI, C. 2014. Overlapping phenotypes in complex spastic paraplegias SPG11, SPG15, SPG35 and SPG48. *Brain*, 137, 1907-20.
- PEREZ-BRANGULI, F., MISHRA, H. K., PROTS, I., HAVLICEK, S., KOHL, Z., SAUL, D., RUMMEL, C., DORCA-AREVALO, J., REGENSBURGER, M., GRAEF, D., SOCK, E., BLASI, J., GROEMER, T. W., SCHLOTZER-SCHREHARDT, U., WINKLER, J. & WINNER, B. 2014. Dysfunction of spatacsin leads to axonal pathology in SPG11-linked hereditary spastic paraplegia. *Hum Mol Genet*, 23, 4859-74.
- PERKINS, L. A., HOLDERBAUM, L., TAO, R., HU, Y., SOPKO, R., MCCALL, K., YANG-ZHOU, D., FLOCKHART, I., BINARI, R., SHIM, H. S., MILLER, A., HOUSDEN, A., FOOS, M., RANDKELV, S., KELLEY, C., NAMGYAL, P., VILLALTA, C., LIU, L. P., JIANG, X., HUAN-HUAN, Q., WANG, X., FUJIYAMA, A., TOYODA, A., AYERS, K., BLUM, A., CZECH, B., NEUMULLER, R., YAN, D., CAVALLARO, A., HIBBARD, K., HALL, D., COOLEY, L., HANNON, G. J., LEHMANN, R., PARKS, A., MOHR, S. E., UEDA, R., KONDO, S., NI, J. Q. & PERRIMON, N. 2015. The Transgenic RNAi Project at Harvard Medical School: Resources and Validation. *Genetics*, 201, 843-52.
- POWERS, H. J. 2003. Riboflavin (vitamin B-2) and health. *Am J Clin Nutr*, 77, 1352-60.

- PRILUTSKY, D., PALMER, N. P., SMEDEMARK-MARGULIES, N., SCHLAEGER, T. M., MARGULIES, D. M. & KOHANE, I. S. 2014. iPSC-derived neurons as a higher-throughput readout for autism: promises and pitfalls. *Trends Mol Med*, 20, 91-104.
- RAGAN, C. I., WILSON, M. T., DARLEY-USMAR, V.M, LOWE, P.N 1987. Subfractionation of mitochondria and isolation of the proteins of oxidative phosphorylation. *Mitochondria: a practical approach*, IRL Press Limited, Oxford, England, 79-112.
- REA, R., SPAUSCHUS, A., EUNSON, L. H., HANNA, M. G. & KULLMANN, D. M. 2002. Variable K(+) channel subunit dysfunction in inherited mutations of KCNA1. *J Physiol*, 538, 5-23.
- REILLY, M. M., MURPHY, S. M. & LAURA, M. 2011. Charcot-Marie-Tooth disease. *J Peripher Nerv Syst*, 16, 1-14.
- REILLY, M. M. & SHY, M. E. 2009. Diagnosis and new treatments in genetic neuropathies. *J Neurol Neurosurg Psychiatry*, 80, 1304-14.
- RIEMENSPERGER, T., KITTEL, R. J. & FIALA, A. 2016. Optogenetics in Drosophila Neuroscience. *Methods Mol Biol*, 1408, 167-75.
- ROBINSON, F. L., NIESMAN, I. R., BEISWENGER, K. K. & DIXON, J. E. 2008. Loss of the inactive myotubularin-related phosphatase Mtmr13 leads to a Charcot-Marie-Tooth 4B2-like peripheral neuropathy in mice. *Proc Natl Acad Sci U S A*, 105, 4916-21.
- ROSSOR, A. M., EVANS, M. R. & REILLY, M. M. 2015. A practical approach to the genetic neuropathies. *Pract Neurol*, 15, 187-98.
- ROSSOR, A. M., TOMASELLI, P. J. & REILLY, M. M. 2016. Recent advances in the genetic neuropathies. *Curr Opin Neurol*, 29, 537-48.
- RUANO, L., MELO, C., SILVA, M. C. & COUTINHO, P. 2014. The global epidemiology of hereditary ataxia and spastic paraplegia: a systematic review of prevalence studies. *Neuroepidemiology*, 42, 174-83.
- RUPPERSBERG, J. P., SCHROTER, K. H., SAKMANN, B., STOCKER, M., SEWING, S. & PONGS, O. 1990. Heteromultimeric channels formed by rat brain potassium-channel proteins. *Nature*, 345, 535-7.
- RUSS, W. P. & ENGELMAN, D. M. 2000. The GxxxG motif: a framework for transmembrane helix-helix association. *J Mol Biol*, 296, 911-9.

- RUSSO, F. B., CUGOLA, F. R., FERNANDES, I. R., PIGNATARI, G. C. & BELTRÃO-BRAGA, P. C. B. 2015. Induced pluripotent stem cells for modeling neurological disorders. *World Journal of Transplantation*, 5, 209-221.
- SANTOSTEFANO, K. E., HAMAZAKI, T., BIEL, N. M., JIN, S., UMEZAWA, A. & TERADA, N. 2015. A practical guide to induced pluripotent stem cell research using patient samples. *Lab Invest*, 95, 4-13.
- SAPORTA, A. S., SOTTILE, S. L., MILLER, L. J., FEELY, S. M., SISKIND, C. E. & SHY, M. E. 2011. Charcot-Marie-Tooth disease subtypes and genetic testing strategies. *Ann Neurol*, 69, 22-33.
- SASAKI, S. 2010. Determination of altered mitochondria ultrastructure by electron microscopy. *Methods Mol Biol*, 648, 279-90.
- SASAKI, S. & IWATA, M. 2007. Mitochondrial alterations in the spinal cord of patients with sporadic amyotrophic lateral sclerosis. *J Neuropathol Exp Neurol*, 66, 10-6.
- SATHASIVAM, S. 2008. Brown-Vialetto-Van Laere syndrome. *Orphanet J Rare Dis*, 3, 9.
- SCAGLIA, F. & NORTHROP, J. L. 2006. The mitochondrial myopathy encephalopathy, lactic acidosis with stroke-like episodes (MELAS) syndrome: a review of treatment options. *CNS Drugs*, 20, 443-64.
- SENDEREK, J., BERGMANN, C., WEBER, S., KETELSEN, U. P., SCHORLE, H., RUDNIK-SCHONEBORN, S., BUTTNER, R., BUCHHEIM, E. & ZERRES, K. 2003. Mutation of the SBF2 gene, encoding a novel member of the myotubularin family, in Charcot-Marie-Tooth neuropathy type 4B2/11p15. *Human Molecular Genetics*, 12, 349-56.
- SHAKHER, J. & STEVENS, M. J. 2011. Update on the management of diabetic polyneuropathies. *Diabetes Metab Syndr Obes*, 4, 289-305.
- SHEN, W., HERNANDEZ-LOPEZ, S., TKATCH, T., HELD, J. E. & SURMEIER, D. J. 2004. Kv1.2-containing K⁺ channels regulate subthreshold excitability of striatal medium spiny neurons. *J Neurophysiol*, 91, 1337-49.
- SHEPHARD, J. A. A. G., P.B. 1969. Citrate synthase from rat liver. *Methods in Enzymology*, 13, 11-19.
- SHI, Y., KIRWAN, P. & LIVESEY, F. J. 2012. Directed differentiation of human pluripotent stem cells to cerebral cortex neurons and neural networks. *Nat Protoc*, 7, 1836-46.

- SHIMOJO, H., OHTSUKA, T. & KAGEYAMA, R. 2008. Oscillations in notch signaling regulate maintenance of neural progenitors. *Neuron*, 58, 52-64.
- SHIMOJO, H., OHTSUKA, T. & KAGEYAMA, R. 2011. Dynamic expression of notch signaling genes in neural stem/progenitor cells. *Front Neurosci*, 5, 78.
- SMART, S. L., LOPANTSEV, V., ZHANG, C. L., ROBBINS, C. A., WANG, H., CHIU, S. Y., SCHWARTZKROIN, P. A., MESSING, A. & TEMPEL, B. L. 1998. Deletion of the K(V)1.1 potassium channel causes epilepsy in mice. *Neuron*, 20, 809-19.
- SON, M. Y., CHOI, H., HAN, Y. M. & CHO, Y. S. 2013. Unveiling the critical role of REX1 in the regulation of human stem cell pluripotency. *Stem Cells*, 31, 2374-87.
- SOUTHGATE, L., DAFOU, D., HOYLE, J., LI, N., KINNING, E., CRITCHLEY, P., NEMETH, A. H., TALBOT, K., BINDU, P. S., SINHA, S., TALY, A. B., RAGHAVENDRA, S., MULLER, F., MAHER, E. R. & TREMBATH, R. C. 2010. Novel SPG11 mutations in Asian kindreds and disruption of spatacsin function in the zebrafish. *Neurogenetics*, 11, 379-89.
- STARACE, D. M. & BEZANILLA, F. 2004. A proton pore in a potassium channel voltage sensor reveals a focused electric field. *Nature*, 427, 548-53.
- STÜHMER, W. 1998. Electrophysiologic recordings from *Xenopus* oocytes. *Methods in Enzymology*, 293, 280-300.
- STUHMER, W., RUPPERSBERG, J. P., SCHROTER, K. H., SAKMANN, B., STOCKER, M., GIESE, K. P., PERSCHKE, A., BAUMANN, A. & PONGS, O. 1989. Molecular basis of functional diversity of voltage-gated potassium channels in mammalian brain. *Embo j*, 8, 3235-44.
- SUN, Y. M., LU, C. & WU, Z. Y. 2016. Spinocerebellar ataxia: relationship between phenotype and genotype - a review. *Clin Genet*, 90, 305-14.
- SYRBE, S., HEDRICH, U. B., RIESCH, E., DJEMIE, T., MULLER, S., MOLLER, R. S., MAHER, B., HERNANDEZ-HERNANDEZ, L., SYNOFZIK, M., CAGLAYAN, H. S., ARSLAN, M., SERRATOSA, J. M., NOTHNAGEL, M., MAY, P., KRAUSE, R., LOFFLER, H., DETERT, K., DORN, T., VOGT, H., KRAMER, G., SCHOLS, L., MULLIS, P. E., LINNANKIVI, T., LEHESJOKI, A. E., STERBOVA, K., CRAIU, D. C., HOFFMAN-ZACHARSKA, D., KORFF, C. M., WEBER, Y. G., STEINLIN, M., GALLATI, S., BERTSCHE, A., BERNHARD, M. K., MERKENSCHLAGER, A., KIESS, W., GONZALEZ, M., ZUCHNER, S., PALOTIE, A., SULS, A., DE JONGHE, P., HELBIG, I., BISKUP, S., WOLFF, M., MALJEVIC, S., SCHULE, R., SISODIYA, S. M., WECKHUYSSEN, S., LERCHE, H. & LEMKE, J. R. 2015. De novo loss- or gain-of-function mutations in KCNA2 cause epileptic encephalopathy. *Nat Genet*, 47, 393-9.

- TAKAHASHI, K. & YAMANAKA, S. 2006. Induction of pluripotent stem cells from mouse embryonic and adult fibroblast cultures by defined factors. *Cell*, 126, 663-76.
- TANG, X., ZHOU, L., WAGNER, A. M., MARCHETTO, M. C., MUOTRI, A. R., GAGE, F. H. & CHEN, G. 2013. Astroglial cells regulate the developmental timeline of human neurons differentiated from induced pluripotent stem cells. *Stem Cell Res*, 11, 743-57.
- TANJI, K., KUNIMATSU, T., VU, T. H. & BONILLA, E. 2001. Neuropathological features of mitochondrial disorders. *Semin Cell Dev Biol*, 12, 429-39.
- TERSAR, K., BOENTERT, M., BERGER, P., BONNEICK, S., WESSIG, C., TOYKA, K. V., YOUNG, P. & SUTER, U. 2007. Mtmr13/Sbf2-deficient mice: an animal model for CMT4B2. *Hum Mol Genet*, 16, 2991-3001.
- THOMSON, J. A., ITSKOVITZ-ELDOR, J., SHAPIRO, S. S., WAKNITZ, M. A., SWIERGIEL, J. J., MARSHALL, V. S. & JONES, J. M. 1998. Embryonic stem cell lines derived from human blastocysts. *Science*, 282, 1145-7.
- TOMLINSON, S. E., RAJAKULENDRAN, S., TAN, S. V., GRAVES, T. D., BAMIOU, D. E., LABRUM, R. W., BURKE, D., SUE, C. M., GIUNTI, P., SCHORGE, S., KULLMANN, D. M. & HANNA, M. G. 2013. Clinical, genetic, neurophysiological and functional study of new mutations in episodic ataxia type 1. *J Neurol Neurosurg Psychiatry*, 84, 1107-12.
- TOOTH, H. 1886. The Peroneal Type of Progressive Muscular Atrophy. *London: H.K. Lewis and Co.*
- TURRENS, J. F. 2003. Mitochondrial formation of reactive oxygen species. *J Physiol*, 552, 335-44.
- UDHAYABANU, T., MANOLE, A., RAJESHWARI, M., VARALAKSHMI, P., HOULDEN, H. & ASHOKKUMAR, B. 2017. Riboflavin Responsive Mitochondrial Dysfunction in Neurodegenerative Diseases. *J Clin Med*, 6.
- VAN LAERE, J. 1966. Paralysie bulbo-pontine chronique progressive familiale avec surdité . Un cas de syndrome de Klippel-Trenaunay dans la me^me fratrie. Proble`mes diagnostiques et ge´ ne´ tiques. *Rev Neurol* 115, 289-95.
- VANDYKE, D. H., GRIGGS, R. C., MURPHY, M. J. & GOLDSTEIN, M. N. 1975. Hereditary myokymia and periodic ataxia. *J Neurol Sci*, 25, 109-18.
- VIALETTO, E. 1936. Contributo alla forma ereditaria della paralisi bulbare progressive. *Riv Sper Freniat*, 40, 1-24.

- VINSANT, S., MANSFIELD, C., JIMENEZ-MORENO, R., DEL GAIZO MOORE, V., YOSHIKAWA, M., HAMPTON, T. G., PREVETTE, D., CARESS, J., OPPENHEIM, R. W. & MILLIGAN, C. 2013. Characterization of early pathogenesis in the SOD1(G93A) mouse model of ALS: part II, results and discussion. *Brain Behav*, 3, 431-57.
- VIVEKANANDA, U., NOVAK, P., BELLO, O. D., KORCHEV, Y. E., KRISHNAKUMAR, S. S., VOLYNSKI, K. E. & KULLMANN, D. M. 2017. Kv1.1 channelopathy abolishes presynaptic spike width modulation by subthreshold somatic depolarization. *Proc Natl Acad Sci U S A*, 114, 2395-2400.
- VOET, D. J., VOET J. G. 2008. Chapter 18, Mitochondrial ATP synthesis. *Wiley*, 3rd Edition, 608.
- WADE, G. R., LAURIER, L. G., PREIKSAITIS, H. G. & SIMS, S. M. 1999. Delayed rectifier and Ca(2+)-dependent K(+) currents in human esophagus: roles in regulating muscle contraction. *Am J Physiol*, 277, G885-95.
- WANG, H., KUNKEL, D. D., MARTIN, T. M., SCHWARTZKROIN, P. A. & TEMPEL, B. L. 1993. Heteromultimeric K⁺ channels in terminal and juxtaparanodal regions of neurons. *Nature*, 365, 75-9.
- WANG, K., LI, M. & HAKONARSON, H. 2010. ANNOVAR: functional annotation of genetic variants from high-throughput sequencing data. *Nucleic Acids Res*, 38, e164.
- WU, H., XU, J., PANG, Z. P., GE, W., KIM, K. J., BLANCHI, B., CHEN, C., SUDHOF, T. C. & SUN, Y. E. 2007. Integrative genomic and functional analyses reveal neuronal subtype differentiation bias in human embryonic stem cell lines. *Proc Natl Acad Sci U S A*, 104, 13821-6.
- XIE, G., HARRISON, J., CLAPCOTE, S. J., HUANG, Y., ZHANG, J. Y., WANG, L. Y. & RODER, J. C. 2010. A new Kv1.2 channelopathy underlying cerebellar ataxia. *J Biol Chem*, 285, 32160-73.
- XUAN, Z., AN, Y., YANG, D., WANG, S., XU, Q. & YUAN, S. 2013. Exploration of the protection of riboflavin laurate on oral mucositis induced by chemotherapy or radiotherapy at the cellular level: what is the leading contributor? *Int J Mol Sci*, 14, 4722-33.
- YAMADA, E. S., RESPONDEK, G., MUSSNER, S., DE ANDRADE, A., HOLLERHAGE, M., DEPIENNE, C., RASTETTER, A., TARZE, A., FRIGUET, B., SALAMA, M., CHAMPY, P., OERTEL, W. H. & HOGLINGER, G. U. 2014. Annonacin, a natural lipophilic mitochondrial complex I inhibitor, increases phosphorylation of tau in the brain of FTDP-17 transgenic mice. *Exp Neurol*, 253, 113-25.

- YAMAMOTO, S., INOUE, K., OHTA, K. Y., FUKATSU, R., MAEDA, J. Y., YOSHIDA, Y. & YUASA, H. 2009. Identification and functional characterization of rat riboflavin transporter 2. *Journal of biochemistry*, 145, 437-43.
- YAO, Y., YONEZAWA, A., YOSHIMATSU, H., MASUDA, S., KATSURA, T. & INUI, K. 2010. Identification and comparative functional characterization of a new human riboflavin transporter hRFT3 expressed in the brain. *The Journal of nutrition*, 140, 1220-6.
- YONEZAWA, A. & INUI, K. 2013. Novel riboflavin transporter family RFVT/SLC52: identification, nomenclature, functional characterization and genetic diseases of RFVT/SLC52. *Molecular aspects of medicine*, 34, 693-701.
- YOSHIMATSU, H., YONEZAWA, A., YAMANISHI, K., YAO, Y., SUGANO, K., NAKAGAWA, S., IMAI, S., OMURA, T., NAKAGAWA, T., YANO, I., MASUDA, S., INUI, K. & MATSUBARA, K. 2016. Disruption of Slc52a3 gene causes neonatal lethality with riboflavin deficiency in mice. *Sci Rep*, 6, 27557.
- ZANETTE, D., MONACO, H. L., ZANOTTI, G. & SPADON, P. 1984. Crystallization of hen eggwhite riboflavin-binding protein. *J Mol Biol*, 180, 1185-7.
- ZEMPLINI, J., GALLOWAY, J. R. & MCCORMICK, D. B. 1996. Pharmacokinetics of orally and intravenously administered riboflavin in healthy humans. *Am J Clin Nutr*, 63, 54-66.
- ZERR, P., ADELMAN, J. P. & MAYLIE, J. 1998. Episodic ataxia mutations in Kv1.1 alter potassium channel function by dominant negative effects or haploinsufficiency. *J Neurosci*, 18, 2842-8.
- ZHANG, P., WANG, J. & SHI, Y. 2010. Structure and mechanism of the S component of a bacterial ECF transporter. *Nature*, 468, 717-20.
- ZHANG, Y., PAK, C., HAN, Y., AHLENIUS, H., ZHANG, Z., CHANDA, S., MARRO, S., PATZKE, C., ACUNA, C., COVY, J., XU, W., YANG, N., DANKO, T., CHEN, L., WERNIG, M. & SUDHOF, T. C. 2013. Rapid single-step induction of functional neurons from human pluripotent stem cells. *Neuron*, 78, 785-98.
- ZHOU, L., ZHANG, C. L., MESSING, A. & CHIU, S. Y. 1998. Temperature-sensitive neuromuscular transmission in Kv1.1 null mice: role of potassium channels under the myelin sheath in young nerves. *J Neurosci*, 18, 7200-15.
- ZUBERI, S. M., EUNSON, L. H., SPAUSCHUS, A., DE SILVA, R., TOLMIE, J., WOOD, N. W., MCWILLIAM, R. C., STEPHENSON, J. B., KULLMANN, D. M. & HANNA, M. G. 1999. A novel mutation in the human voltage-gated potassium channel gene (Kv1.1)

associates with episodic ataxia type 1 and sometimes with partial epilepsy. *Brain*, 122 (Pt 5), 817-25.

Appendix I

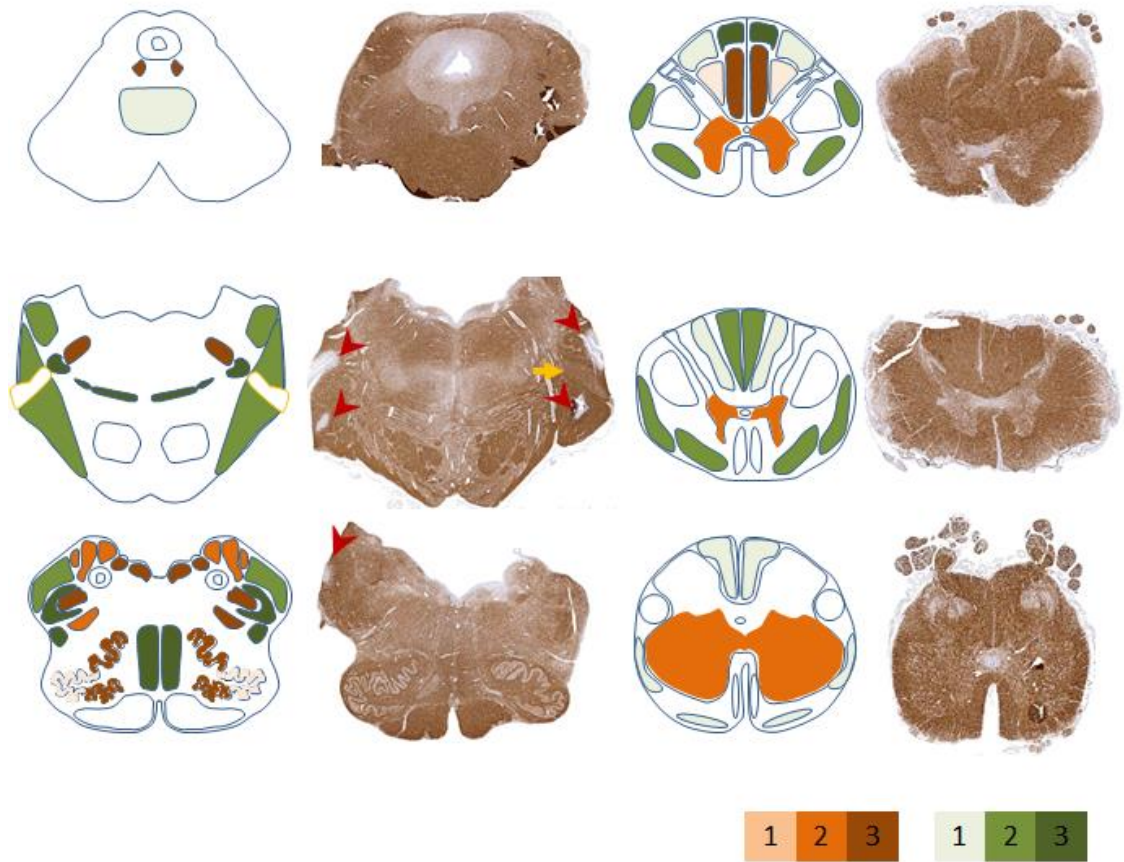


Figure I. Schematic representation of the anatomical distribution and severity of the brain stem and spinal cord pathology in the patient AM2.

In the schematic figures the severity of grey matter pathology is indicated in orange with the lightest shade corresponding to mild neuronal atrophy and mild gliosis and the darkest shade corresponding to severe atrophy and gliosis. The severity of white matter tract pathology is indicated in green with the lightest shade corresponding to mild pathology and the darkest shade corresponding to a severe myelinated fibre loss. The corresponding transverse brain stem and spinal cord sections are immune-stained for myelin with SMI94 antibody. The red arrowheads in the pons indicate the bilateral symmetrical lesions surrounding both 5th cranial nerves, indicated with a yellow arrow on one side. Also the lesion in the medulla is indicated with a red arrowhead.

Appendix II

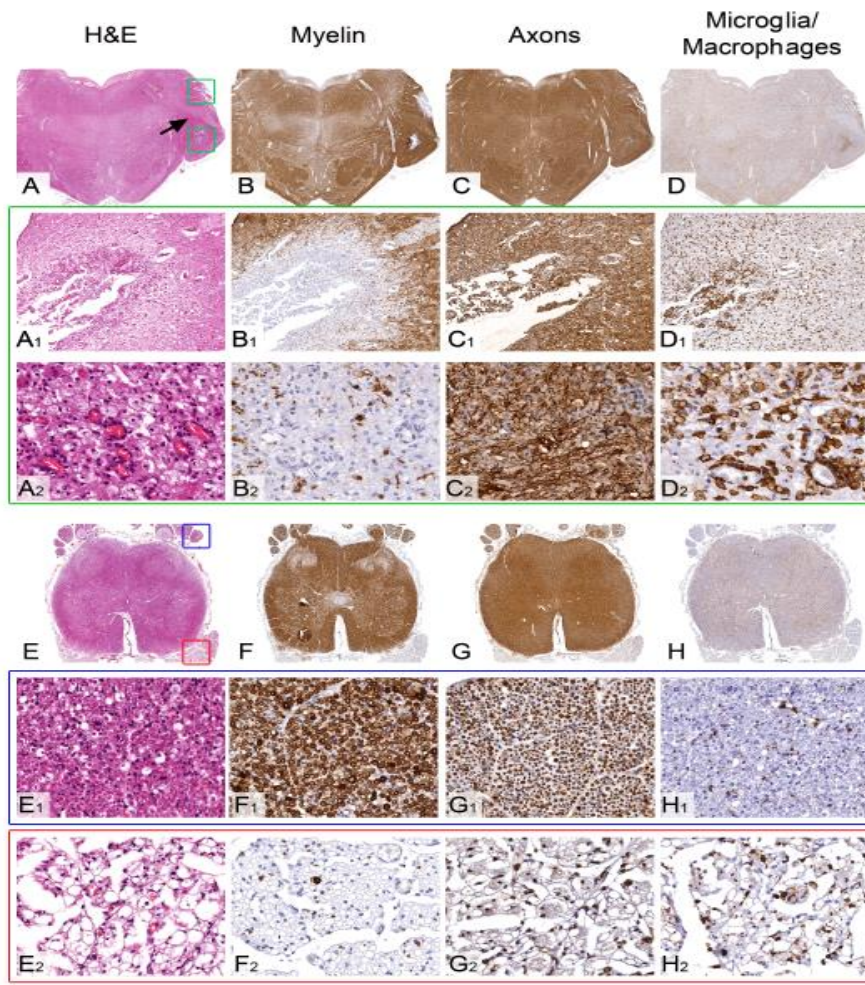


Figure II. Pathological features of the symmetrical brain stem lesions and the comparison of the spinal cord nerve root involvement in the patient AM2.

(A, B, C and D) Low power views of the pons and (A₁, B₁, C₁, D₁, A₂, B₂, C₂ and D₂) high power views of the pontine lesion indicated with green square boxes in A. (A, A₁ and A₂) The Haematoxylin and Eosin (H&E) stained section demonstrates sharply demarcated lesion surrounding the 5th cranial nerve (black arrow). High power view (A₂) reveals frequent small calibre blood vessels and foamy macrophages within the lesion. (B, B₁ and B₂) Immunostaining for myelin with SMI94 antibody shows a near complete absence of myelin, whilst the axons (C, C₁ and C₂), demonstrated with SMI31 antibody, are well preserved within the lesion. (D, D₁ and D₂) Immunostaining for macrophages with CD68 antibody confirm a dense infiltrate of macrophage in the centre of the lesion. (E, F, G and H) Low power views of transverse sections of the sacral spinal cord. The posterior nerve roots are indicated with blue square box in E and on high power views in E₁, F₁, G₁ and H₁. The anterior nerve roots are indicated with red square box in E and on high power views in E₂, F₂, G₂ and H₂. (E₁, F₁, and G₁) The posterior nerve roots are densely populated with myelinated fibres with (H₁) minimal macrophage activity. (E₂, F₂, and G₂) In the anterior nerve roots there is a severe loss of myelinated fibres and (H₂) widespread infiltration of macrophages. Scale bar: 4 mm in A-D; 1.7 mm in E-H; 350 µm in A₁- D₁; 70 µm in A₂- D₂; 140 µm in E₁- H₁ and E₂- H₂.

Appendix III

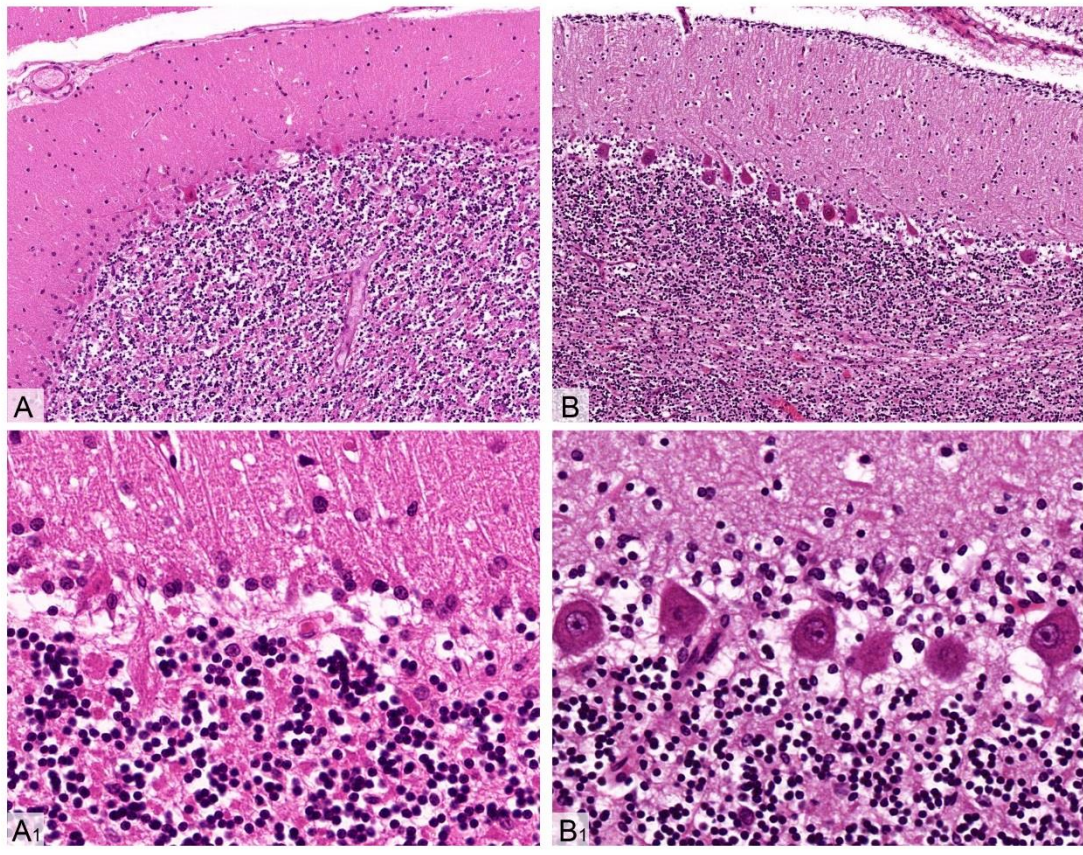


Figure III. Comparison of the cerebellar atrophy between patient AM4 and AM2

(A and A₁) correspond to patient AM4 and (B and B₁) correspond to patient AM2. (A and A₁) In the cerebellar cortex from the patient AM4 there is severe Purkinje cell loss with widespread Bergmann gliosis. (B and B₁) In the patient AM2 the Purkinje cells are well preserved. Note the presence of external granular cell layer (B₁) in patient AM2, a normal finding for the patient's young age. Scale bar: 80 μ m in A-B and 30 μ m in A₁-B₁.

Appendix IV

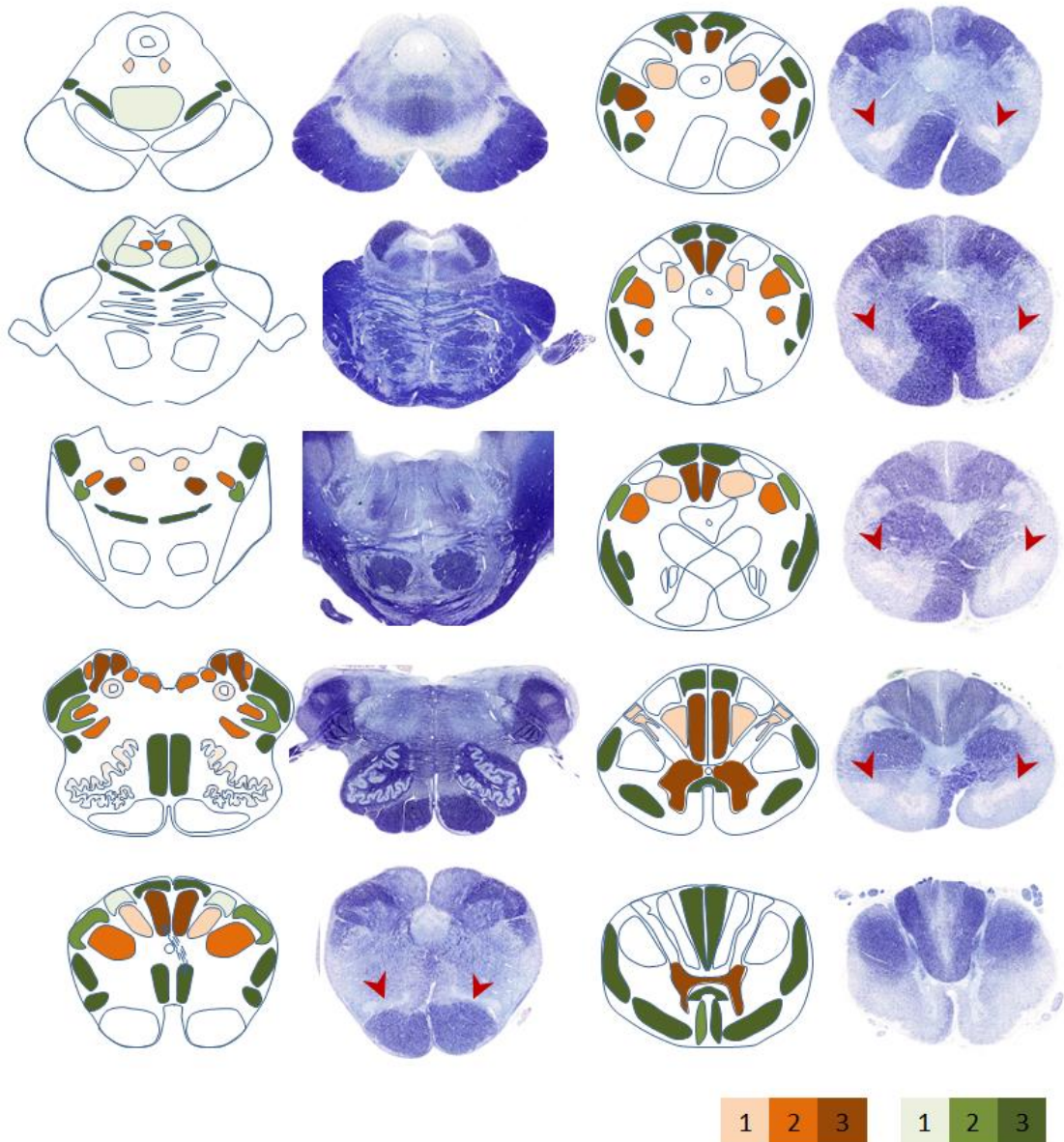


Figure IV. Schematic representation of the anatomical distribution and severity of the brain stem and spinal cord pathology in the patient AM4.

In the schematic figures the severity of grey matter pathology is indicated in orange with the lightest shade corresponding to mild neuronal atrophy and mild gliosis and the darkest shade corresponding to severe atrophy and gliosis. The severity of white matter tract pathology is indicated in green with the lightest shade corresponding to mild and the darkest shade corresponding to a severe fibre loss. The corresponding transverse brain stem and spinal cord sections are stained with luxol fast blue special stain, where normally myelinated tracts are stained dark blue. The red arrowheads in the anterior aspect of the lower medulla and spinal cord indicate the bilateral symmetrical lesions.

Appendix V

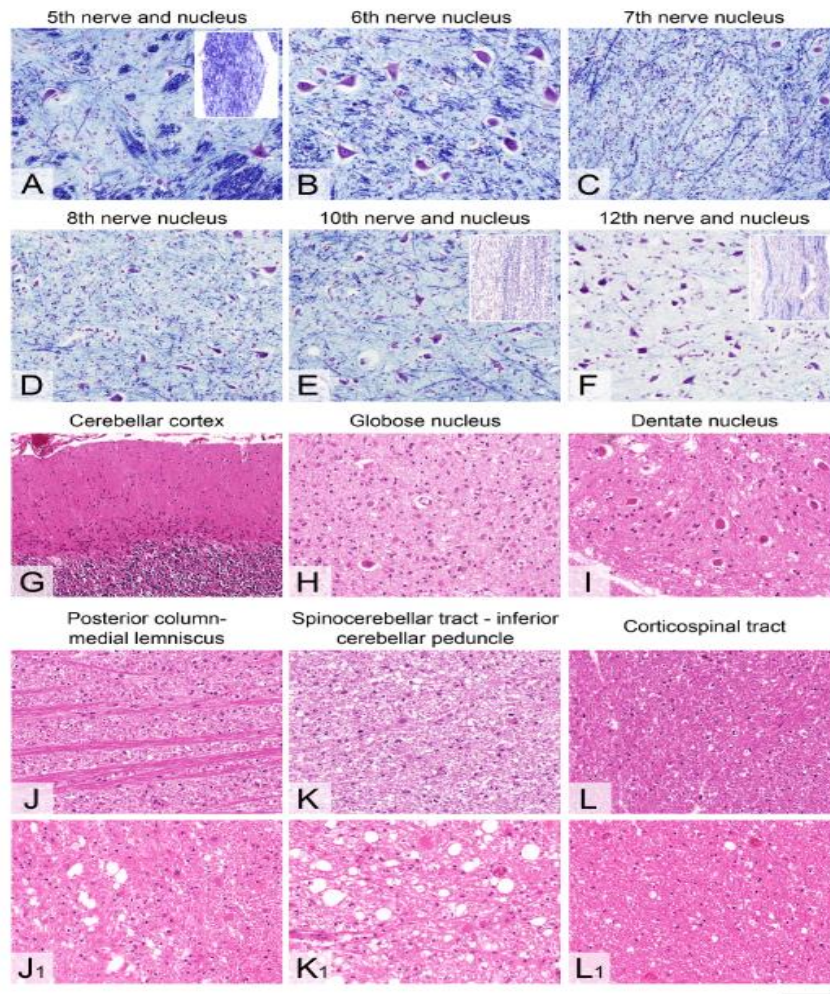


Figure V. The spectrum of the atrophy in the cranial nerve nuclei, deep cerebellar nuclei and white matter tracts in the patient AM4.

(A) In the 5th cranial nerve nucleus there is a moderately severe neuronal loss and gliosis and accompanying myelinated fibre loss in the nerve tract (inset). (B) The 6th cranial nerve nucleus shows only very mild neuronal loss and gliosis. (C) In the 7th and (D) 8th cranial nerve nuclei the neuronal loss and accompanying gliosis is very severe. (E) In the nuclei of the 10th and (F) 12th cranial nerves the neuronal loss and gliosis is moderately severe, but the nerve tracts (inset in E for the 10th nerve and inset in F for the 12th nerve) show marked depletion of myelinated fibres. (G) In the cerebellar cortex there is widespread Purkinje cell loss, Bergmann gliosis and gliosis in the molecular cell layer. (H) The globose nucleus shows a severe neuronal loss and gliosis, whilst (I) the neurons in the dentate nucleus are better preserved and gliosis is mild. (J) The medial lemniscus in the medulla, (J₁) the gracile fasciculus in the posterior column, (K) inferior cerebellar peduncle in hindbrain and spinocerebellar tract in the spinal cord (K₁) show severe gliosis and vacuolation of the neuropil on H&E stained sections, and microglial activation on immunohistochemistry (not shown). (L and L₁) The corticospinal tracts at the level of medulla (L) and spinal cord (L₁) in contrast is well populated by myelinated fibres with no apparent gliosis. Scale bar: 110 µm in A-F and H-L; 220 µm in G. (A-F): stained with luxol fast blue. (G-I and J, J₁-L, L₁): stained with H&E

Appendix VI

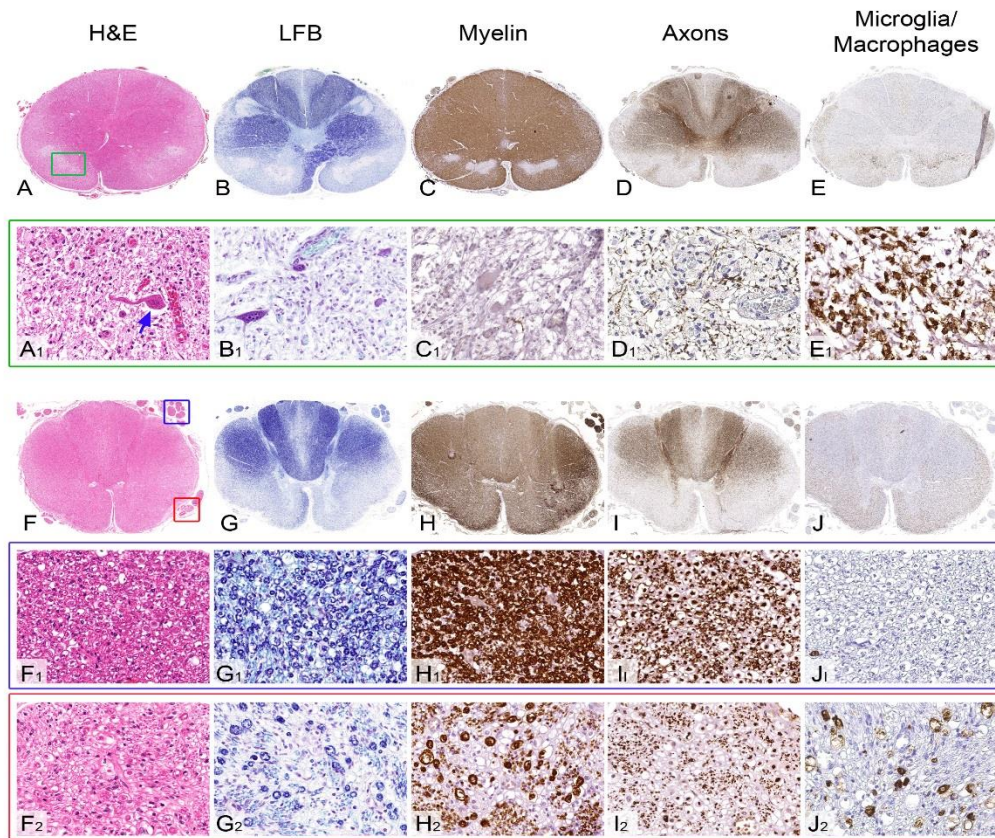


Figure VI. Pathological features of the symmetrical brain stem and spinal cord lesions and the comparison of the spinal cord nerve root involvement in the patient AM4.

(A, B, C, D and E) Low power views of the upper cervical cord and (A₁, B₁, C₁, D₁ and E₁) high power views of the lesion indicated with green square box in A. (A and A₁) The H&E stained section demonstrates bilateral symmetrical sharply demarcated lesions (indicated with a green square box on one side) in the anterior part of the upper cervical cord. High power view of the lesion (A₁) reveals intact neurones (blue arrow) within a dense infiltrate of foamy macrophages and increased numbers of small calibre blood vessels. (B and B₁) Staining for myelin with luxol fast blue (LFB) special stain and (C and C₁) immunostaining with SMI94 antibody highlights the preservation of the neurones and shows complete absence of myelin, whilst the axons (D and D₁), demonstrated with SMI31 antibody, are better preserved within the lesion. (E and E₁) Dense infiltrates of macrophages within the bilateral lesions are confirmed with CD68 immunohistochemistry. (F, G, H, I and J) Low power views of transverse section of the thoracic spinal cord. The posterior nerve roots are indicated with blue square box in F and on high power views in F₁, G₁, H₁, I₁ and J₁. The anterior nerve roots are indicated with red square box in F and on high power views in F₂, G₂, H₂, I₂ and J₂. (F₁, G₁, H₁ and I₁) The posterior nerve roots are densely populated with myelinated fibres with (J₁) minimal macrophage activity. (F₂, G₂, H₂ and I₂) In the anterior nerve roots there is a moderately severe loss of myelinated fibres and (J₂) prominent macrophage activation. Scale bar: 2.5 mm in A-E and F-J; 80 µm in A₁- E₁, F₁- J₁ and F₂- J₂.

